Durability Study of Proton Exchange Membrane Fuel Cells via Experimental Investigations and Mathematical Modeling

Dan Liu

Dissertation submitted to the faculty of the Virginia Polytechnic Institute and State University in partial fulfillment of the requirements for the degree of

Doctor of Philosophy
In
Macromolecular Science & Engineering

Scott W. Case, Chair
Michael W. Ellis
John J. Lesko
James E. McGrath
Garth L. Wilkes

July 11, 2006
Blacksburg, Virginia

Keywords: Durability, Proton Exchange Membrane Fuel Cell, Mechanical Properties, Proton Conductivity, Aging, Cyclic Profile

Durability Study of Proton Exchange Membrane Fuel Cells via Experimental Investigations and Mathematical Modeling

Dan Liu

ABSTRACT

In this dissertation, novel approaches to PEMFC durability research are summarized. These efforts are significantly different from most other studies on durability in that rather than focusing on chemical degradation, more attention is given to the mechanical aspects of the PEMFC system. The tensile stress-strain behavior of Nafion® 117 (N117) and sulfonated poly(arylene ether sulfone) random copolymer (BPSH35) membranes is explored under ambient conditions, with respect to the effects of initial strain rate, counterion type, molecular weight and the presence of inorganic fillers. A three-dimensional "bundle-cluster" model is proposed to interpret the tensile observations, combining the concepts of elongated polymer aggregates, proton conduction channels as well as states of water. The rationale focuses on the polymer bundle rotation/interphase chain readjustment before yielding and polymer aggregates disentanglement/ reorientation after yielding.

In addition, the influence of uniaxial loading on proton conductivity of N117 and BPSH35 membranes is investigated. When the membranes are stretched, their proton conductivities in the straining direction increase compared to the unstretched films, and then relax exponentially with time. The behavior is explained on the basis of the morphological variations of hydrophilic channels, accompanied by the rotation, orientation and disentanglement of the copolymer chains in the hydrophobic domains, as illustrated with the help of our bundle-cluster model.

Finally, the long-term aging of hydrogen-air PEMFCs is examined with a cyclic current profile and under constant current conditions. The end-of-period diagnosis is performed for both MEAs at 100h aging intervals, including a series of cell polarization, impedance and electrochemical experiments. The results demonstrate that hydrogen crossover is the most significant result of degradation for the MEA under cyclic aging mode due to the formation of pinholes at approximately 500-600h, and mass transport limitations are the major degradation sources for constant current mode. A phenomenological mathematical model is set up to describe the PEMFC aging process under both cyclic and constant conditions.

AUTHOR'S ACKNOWLEDGEMENTS

I would like to give my sincere gratitude to Dr. Scott W. Case, for providing me with the opportunity of being his student, which always makes me feel lucky. I wish to express my thanks to my academic committee members, Dr. James McGrath, Dr. Garth Wilkes, Dr. John J. Lesko and Dr. Michael W. Ellis for their guidance and help. In particular, I appreciate the generous help from Dr. Michael W. Ellis for the utilization of fuel cell test stations and potentiostat in his lab. I thank Dr. Garth Wilkes for his valuable suggestions regarding to membrane mechanical and morphological properties. I want to greatly acknowledge Mr. Marshall McCord for his wonderful help in designing the screw-driven fixture and grips utilized in stress relaxation of membranes in water. I also appreciate the assistance in instrumentation provided by Mr. Robert A. Simonds. I am grateful to Ms. Melinda Hill for her supply of BPSH35-R polymers and BPSH35-ZrPP films, and Dr. Mark G. Roelofs and Dr. Dennis E. Curtin at Dupont Fuel Cells for their donation of Nafion 1135 and 1035 extruded films.

I cannot express enough of my appreciation to Dr. Michael A. Hickner for his experimental guidance and Sandia National Laboratories for the use of facilities. That 40-day stay at Sandia Mountains provided me with the unique experience of a lifetime. I also thank Dr. Yeh-Hung Lai at General Motors Fuel Cell Activities for his efforts in providing the cyclic current aging spectrum. Ms. Kim Greenberg and Dr. Michael Budinski of General Motors Fuel Cell Activities are acknowledged here for imaging of the aged MEAs with both optical and scanning electron microscope. I am very grateful to Macromolecules and Interfaces Institute (MII) at Virginia Tech for the graduate frontiers fellowship that supported my Ph.D. study at Blacksburg, Virginia. My special thanks go to Dr. Judy S. Riffle, whose efforts brought me into the interdisciplinary Macromolecular Science & Engineering program. It has broadened my view of science/engineering and will definitely benefit my future career.

I finally thank my husband and my parents in China for their precious love and support through all of the years. Thank you, Dad and Mom, for raising me up and paying the bills for your only child to come to the U.S. and acquire the Doctorate degree in Macromolecular Science & Engineering at Virginia Tech.

TABLE OF CONTENTS

LIST OF FIGURES

LIST OF TABLES

Chapter 1. Introduction and Overview of the Research

1.1 Introduction

Fuel cells are energy devices that convert chemical energy into electrical energy. As a result of the electrochemical reactions occurring on the two electrodes, the fuel at the anode side is oxidized to release electrons, which are then transferred to the cathode side, reducing the oxidant species (usually oxygen). The flow of electrons during these electrochemical processes gives rise to current in the electrical circuit, while potential difference exists over the two electrodes based upon the nature of the redox reactions. The electrical energy obtained by fuel cells can be utilized in residential, stationary, adventure, distant communication and transport applications. The biggest advantage of fuel cell energy compared to traditional energy is its high efficiency. Unlike internal combustion and steam engines, heat exchange and mechanical work are no longer the major energy conversion methods. The electrons from the chemical reactions themselves are collected and conveyed directly to supply power. With the proper selection of fuel such as pure hydrogen, the fuel cell energy is fairly clean, showing great potential of mitigating the environmental pollution problem of modern industrial world.

In spite of the potential, fuel cells have not been commercialized to a large extent after its first invention almost two hundred years ago. The state-of-the-art fuel cells on the market exist in three formats: as network or uninterrupted power supply (UPS) to certain residential and industrial applications, as major power system for adventure and telecommunication at distant locations, and as demonstration units in universities and automobile companies. In the 1990's, megawatt (MW) phosphoric acid fuel cell (PAFC) power plants were established and began to supply power. A number of 250 kilowatt (KW) molten carbonate fuel cell (MCFC) power plants have been under operation since the early 2000's. Another type of high temperature fuel cells, solid oxide fuel cells (SOFCs) are forecast to reach $335 million in sales by the anticipated year of commercialization (2008) with an average annual growth rate (AAGR) of 22.2% through the forecast period.[1] Proton exchange membrane fuel cells (PEMFCs) are being seriously considered by the automotive industry as vehicle primary or secondary engine for their high efficiency, clean side product (H_2O) and employment of solid state electrolyte. Quite a few prototypes have been established to demonstrate the capability

of PEMFCs to power not only vehicles but residential areas. Nevertheless, the source of pure hydrogen remains an unresolved issue for PEMFC application. Although hydrogen can be obtained by water electrolysis, methanol/natural gas/gasoline reformation and bacterial production, the cost of hydrogen generation, storage and building hydrogen fueling infrastructure is high. In particular, reformation of hydrocarbon compounds cannot eliminate the dependence of power generation on naturally conserved fossil resources and has carbon dioxide (CO_2) as one of the end products, causing environmental issues by itself.

While the cost problem of fuel cells can be reduced by mass sale/production or mitigated due to certain circumstances such as remote locations, durability and reliability of fuel cells are essential for the goal of fuel cell commercialization. Fuel cells must last long enough in order to serve their duties and compete with the conventional energy devices. Fuel cells are subject to high temperature, high humidity, flow of fuel and oxidant and strong acid or alkaline environment. There are a number of components in the system, including the electrolytes, catalyst layers, gas diffusion layers (which comprise the membrane-electrode-assemblies, MEAs), bipolar plates and current collector plates. In order to achieve good long-term performance, it is necessary for all of these components to maintain their integrity. Therefore the materials selection and system configuration are critical when designing the fuel cells. The electrical, chemical, physical and mechanical properties of the components need to be tailored to reach the optimum state in terms of performance, cost and durability. The MEA fabrication method should also be improved to reduce the damage to the membranes, such as residue stress concentrations induced by hot pressing.

Although the study of fuel cell durability has attracted more and more attention in recent years, the fundamental aspects of component properties and degradation along with operation have not been fully characterized. However, the information obtained via detailed investigations of component durability is necessary for microscopic mathematical modeling. To achieve maximum accuracy of the durability model and to provide useful guidance for manufacturing, both steady-state and transient values of property parameters are to be substituted into the fuel cell model, incorporating the aging phenomena and effects. Eventually, the lifetime of the fuel cells can be predicted based upon different materials, structure and operation conditions, which enables a closer approach to fuel cell commercialization.

1.2 Overview of the Research

As described in the previous section, fuel cell durability is a complex topic that demands a great deal of work. In this dissertation, we focus on the characterization of proton exchange membrane (PEM) mechanical and transport properties as well as proton exchange membrane fuel cell (PEMFC) long-term aging study. The tensile behavior of two types of membranes, Nafion and sulfonated poly(arylene ether sulfone) random copolymer is explored under ambient conditions, with respect to different strain rates, counterions, inorganic additives and molecular weights. Stress relaxation of the membranes is also measured under ambient conditions at different initial strain levels and strain rates, with master curves of stress relaxation modulus versus time constructed. To interpret the data, a new morphological "Bundle-Cluster" model is proposed combining the concepts of elongated polymer aggregates, proton conduction channels as well as states of water. The interpretation is mainly involved with the chain motion in the hydrophobic phase, corresponding to the mechanical behavior of membrane with low water contents. The investigation of membrane tensile properties and proposal of "Bundle-Cluster" model provide a basis for modeling the reaction of membrane to fuel cell hydrothermal environment, especially the pinhole formation. It necessitates the assessment of membrane mechanical response at elevated temperature and high humidity, which will be continued in the future research.

In addition to mechanical characterizations, the proton conductivity of the membranes is evaluated in water at various temperatures with applied strain. The series of the proton conductivity experiments address the influence of strain-induced changes in the hydrophilic channel structure on proton conduction. The stress relaxation of submerged membranes is quantified under the same conditions with proton conductivity measurements. Three-term Prony series are employed to fit the results of proton conductivity and stress relaxation and the relaxation times are estimated. The activation energy for proton conduction is computed and associated with the morphological explanations for the experimental observations. The change of proton conductivity under strain is important to the long-term performance of PEMFCs because this value determines the resistance to protons transfer from anode to cathode, which is directly related to the distribution of oxygen reduction reaction (ORR) and the corresponding heating, along with the overall efficiency of power generation.

The last part of this dissertation concentrates on the results of two long-term aging experiments for PEMFCs. Commercial MEAs are purchased to conduct aging in 10 aging periods, with 100h of continuous operation per aging period. End-of-period diagnosis is carried out after each aging period, including polarization curve, impedance, Tafel plot, hydrogen crossover current and cyclic voltammetry. Samples of cathode outlet water are collected to determine the fluoride ion concentration and pH value. Two aging modes are tested, specifically cyclic current aging and constant current aging mode. The cyclic current aging profile is provided as a potential Department of Energy (DOE) durability test protocol. The data analysis demonstrates the consequences of fuel cell operation conditions on its durability. Large amount of hydrogen crossover is identified as the major degradation source for PEMFC under cyclic current aging mode, whereas mass transport limitations are the biggest causes of cell degradation under constant current mode. A phenomenological durability model is set up to incorporate the aging effects into the fuel cell semi-empirical equation and capable of describing the evolutions of fuel cell performance as a function of time.

The research presented in this dissertation lays a foundation for more detailed fuel cell system/components durability study. The evolution laws of materials utilized in PEMFCs have to be discovered under all kinds of circumstances before a robust microscopic durability model can be established. Careful design of aging experiments and characterization of material properties are preferable to provide solutions to the durability question. It is reasonable to anticipate that the goal of durability prediction and manipulation will be achieved eventually, as long as the systematic degradation analysis and incorporation of the analysis into the durability model are performed properly.

Chapter 2. Literature Review

2.1 Introduction

Fuel cells have received a great deal of interest in recent years for their potential to solve several major challenges facing America today: dependence on petroleum imports, poor air quality, and greenhouse gas emissions. R&D efforts including mathematical modeling and equipment developing has been put down to this "next generation technology." A fuel cell is defined as an electrochemical "device" that continuously converts chemical energy into electric energy (and some heat) for as along as fuel and oxidant are supplied.[2] But since people have relatively cheaper batteries to supply small-scale power and engines to output work, why are we still bothering to develop fuel cells? Let us compare the similarities and differences among these three to see.[2] The similarities are: (1) Fuel cells and batteries share the electrochemical nature of power generation processes; (2) Fuel cells and engines work continuously consuming a fuel. The differences are: (1) Fuel cells do not need recharging; (2) Fuel cells can operate quietly and efficiently; (3) Some types of fuel cells generate only power, water and heat (so called "zero-emission engine") (4) The usage of fuel cells can reduce the consumption of primary fossil fuels. (5) The ratio of manufacturing cost to output power density of fuel cells is currently much higher than that of batteries and engines.

Now we have realized that the environmental considerations and high efficiency bring about the big advantage of fuel cells over the traditional power suppliers. Before reviewing the proton exchange membrane fuel cell (PEMFC) modeling, a general introduction of fuel cells is given in the following sections.

2.1.1 Classifications of Fuel Cells

All of the fuel cells function in the same basic way, i.e., a fuel is oxidized into electrons and protons; oxygen is reduced to oxide species; proton or oxide ions are transported through the ion-conducting but electronically insulating electrolyte.

Fuel cells can be classified based on the type of electrolyte used in a fuel cell (exception: DMFC, in which methanol is the fuel): alkaline fuel cell (AFC), proton exchange membrane fuel cell (PEMFC), direct methanol fuel cell (DMFC), phosphoric acid fuel cell (PAFC), molten carbonate fuel cell (MCFC) and solid oxide fuel cell (SOFC). Among these types of fuel cells, the first four belong to low temperature fuel cells, which operate at a temperature lower than 220°C. The high temperature fuel cells including MCFC and SOFC operate at 600 to 1000°C. Table 2-1 summarizes the features of different types of fuel cells.

Table 2-1. Features of different types of fuel cells.[3]

	AFC	PEMFC	DMFC	PAFC	MCFC	SOFC
Electrolyte	Alkaline	Polymer Membrane	Direct Methanol	Phosphoric Acid	Molten Carbonate	Solid Oxide
Operating temp. (oC)	<100	60-120	60-120	160-220	600-800	800-1000 or 500-600
Anode reaction	$H_2+2OH^- \rightarrow 2H_2O+2e^-$	$H_2 \rightarrow 2H^++2e^-$	$CH_3OH+H_2O \rightarrow CO_2+6H^++6e^-$	$H_2 \rightarrow 2H^++2e^-$	$H_2+CO_3^{2-} \rightarrow H_2O+CO_2+2e^-$	$H_2+O^{2-} \rightarrow H_2O+2e^-$
Cathode reaction	$1/2O_2+H_2O+2e^- \rightarrow 2OH-$	$1/2O_2+2H^++2e^- \rightarrow 2H_2O$	$3/2O_2+6H^++6e^- \rightarrow 6H_2O$	$1/2O_2+2H^++2e^- \rightarrow 2H_2O$	$1/2O_2+CO_2+2e^- \rightarrow CO_3^{2-}$	$1/2O_2+2e \rightarrow O^{2-}$
Realized power	5-150KW	5-250KW	5KW	50KW-11MW	100KW-2MW	100-250KW
Charge carrier in electrolyte	OH^-	H^+	H^+	H^+	CO_3^{2-}	O^{2-}
Applications	Transportation, space, military, energy storage systems			Combined heat and stationary power	Combined heat and stationary power and transportation	

2.1.2 Applications of Fuel Cells

Based on each fuel cell type's characteristics, fuel cells may have specific applications in three main categories: transportation, stationary, and portable application. For example, AFCs and PEMFCs have been employed as the auxiliary power supply in the Apollo and Germini space

program respectively. PEMFCs may become the future replacement of current internal combustion engines in the automobiles. High temperature fuel cells such as MCFCs and SOFCs have been applied in the stationary power stations to generate electricity and heat for the community. Also researchers are investigating the possibility of DMFCs as the power supplier for portable electronic apparatus including cell phones and laptops. In addition, fuel cells have been used in transit utility vehicles, breath alcohol testers and outdoor activity power sources.

2.2 Fuel Cell History

As early as 1839, Sir William Grove discovered the operating principle of fuel cells by reversing water electrolysis to generate electricity with hydrogen and oxygen. However, the so-called "Gaseous Voltaic Battery" set up by Grove was a fragile apparatus filled with diluted sulfuric acid into which a platinum electrode was dipped, as shown in Figure 2-1.

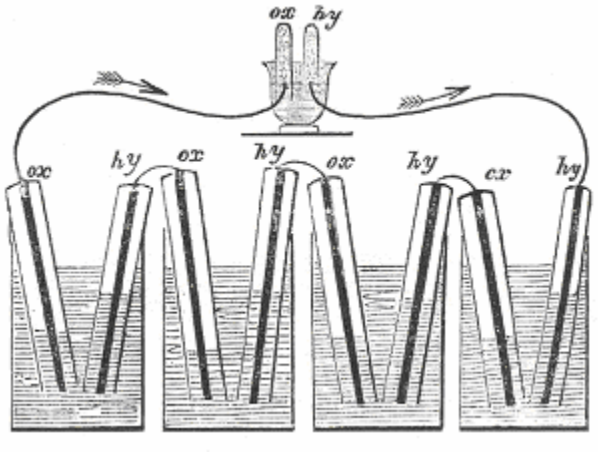

Figure 2-1. The schematic of "Gaseous Voltaic Battery" invented by Sir William Grove.[4]

One also must mention Francis T. "Tom" Bacon, who constructed a fuel cell to repeat the experiment of Grove in 1939.[2] Bacon developed the "double-layer" electrode and solved the liquid flooding and gas bubbling problem between 1946 and 1955. In addition, he worked out the cathode oxidation (corrosion) problem by forming an oxide coating on the nickel electrode.

Bacon built a 6-KW fuel cell stack in 1959. One of his patents was used in the AFC's fabricated for the Apollo space program, as seen in Figure 2-2.

Figure 2-2. The AFCs fabricated for APOLLO space program (courtesy of UTC Fuel Cells).[2]

As for the most popular proton exchange membrane, "Nafion", it was Grot at Du Pont who first introduced a polymer named as "XR" in 1972, which could withstand the chemical degradation mechanism with hydrogen peroxide (H_2O_2). "XR" was improved and registered as "Nafion" in 1975.

Today, most of the major automobile manufacturers have become involved in the development of fuel cells (especially PEMFCs), after they realized the great potential of PEMFCs in applications on future road vehicles. We have seen the exhibition of fuel cell van by General Motors (1967),[2] fuel cell car by DaimlerChrysler (2005), fuel cell bus by Los Alamos National Laboratory (1986)[2] and fuel cell SUV by UTC Fuel Cells (2005) (see Figure 2-3 below).

(a)

(b)

Figure 2-3. (a) Fuel cell car by DaimlerChrysler (2005), (courtesy of DaimlerChrysler); (b) Fuel cell SUV by UTC Fuel Cells (2005) (courtesy of UTC Fuel Cells).

2.3 Challenges Facing the Fuel Cell Technology

Thus far, only the PAFCs and MCFCs have been utilized commercially. There are still some challenges facing the fuel cell technology. In spite that the working principle and equipment design for each type of the fuel cells have been relatively mature, their commercialization remains an unresolved issue, though improvements have been achieved in recent years.

Take PEMFCs as an example, the barriers to commercialization include the cost of stack and durability. First, the high cost of PEMFCs is due to the use of platinum particles as the catalysts of the hydrogen oxidation and oxygen reduction reaction, the "Nafion" membranes whose chemical ingredients include fluorine (an expensive element) and the bipolar plates which are often made of graphite or its composites. Consequently, to lower the cost of a PEMFC, one should start with decreasing the catalyst loading by developing new alloy catalysts, synthesizing new types of suitable membranes (which have to be chemically, physically, and mechanically stable), and tailoring the material properties of bipolar plate such as electrical conductivity and the graphite content by using composite materials. Secondly, for the durability of PEMFCs, approximately 5000 hours operation time has been reported for PEMFC stacks in the literature. So far, the causes of fuel cell degradation and their characteristics have not been modeled well, though a few papers proposed the loss of catalyst activity by platinum sintering and loss of proton conductivity by membrane degradations as the primary degradation mechanisms. In

addition, in order to make PEMFCs durable, good thermal and water management has to be ensured during the operation. The details of PEMFC durability issues will be discussed in Section 2.8.

2.4 Fuel Cell Thermodynamics

Since fuel cells work on the conversion of chemical energy to electrical energy via the catalyzed heterogeneous electrochemical reactions, the rules of thermodynamics will come to play. Before the fuel cell thermodynamics are discussed, let us first make clear the definitions of potentials, overpotentials and efficiencies in a fuel cell.

2.4.1 Definitions of Potentials and Overpotentials

The reversible (Nernst) potential, E_{rev}, is defined as the cell potential at the equilibrium or reversible state, where no irreversibilities exist in the system. The reversible potential of the anode in a PEMFC, where hydrogen oxidation occurs, is 0 V. For the PEMFC cathode, where the oxygen reduction occurs on Pt catalysts, the reversible potential is 1.23 V at 25 ^{o}C and 1 atm with liquid water as the product.[2]

The terminal cell potential, E, is the voltage drop measured at the external electrical load. The open circuit voltage, E_{ocv}, is the potential obtained when the external circuit is open, as shown by its name. In general, we find that $E < E_{ocv} < E_{rev}$.

Adopting the nomenclature of electrochemistry, the potential losses used to run the cell itself are called overpotentials. The anode overpotential is positive, which means the anode potential is higher than 0 V. The cathode overpotential is negative, which means the cathode potential is lower than 1.23 V.[2]

Corresponding to the nature of voltage drops inside the cell, we have the activation overpotential η_{act} , ohmic overpotential η_{ohm} , mass transport overpotential η_{mass} and fuel crossover overpotential η_{cross}.

The overpotentials can be expressed by the following equations:[5]

- Activation overpotential: $\eta_{act} = b \ln \frac{i}{i_0}$ - (1)
- Ohmic overpotential: $\eta_{ohm} = ir_i$ - (2)
- Mass transport overpotential: $\eta_{conc} = \frac{RT}{n\alpha F} \ln(1 - \frac{i}{i_l})$ - (3)
- Fuel crossover overpotential: $\eta_{crossover} = i_n r_n + b \ln \frac{(1 + i_n / i)}{i_0}$ - (4)

where i is the current density, which is equal to current per unit area, i_0 is the exchange current density, b is the Tafel slope, i_l is the limiting current density, R is the gas constant, F is Faraday's constant and i_n is the cell internal current caused by fuel crossover.

Each of the above overpotentials dominates at different current density regions. As shown in Figure 2-4, when the current density is low, the activation overpotential is the main loss mechanism. The ohmic losses dominate at the middle current density region. As the current density continues increasing, the mass transport limitation - induced overpotentials become important.

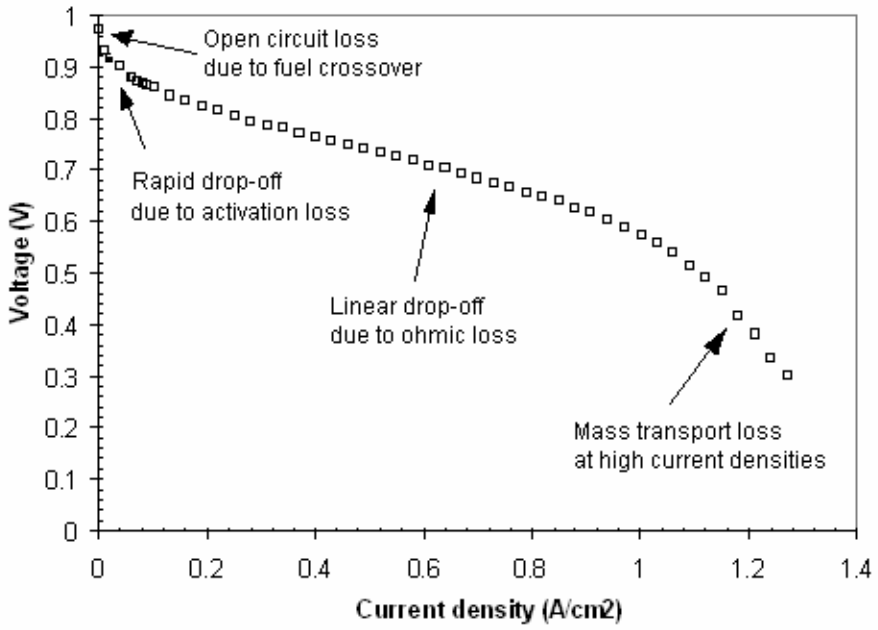

Figure 2-4. Overpotentials in a fuel cell at different current density regions.[6]

2.4.2 Definitions of Efficiencies

With the definitions of fuel cell potential and overpotentials in mind, we can now define the cell efficiencies, which provide a good measure for the cell working conditions.[3]

- Overall (total) efficiency: $\varepsilon_{fc} = -\frac{nFE}{\Delta\bar{h}}$ - (5)
- Thermodynamic efficiency: $\varepsilon_r = -\frac{E_{rev}}{\Delta\bar{h}}$ - (6)
- Electrochemical (voltage) efficiency: $\varepsilon_V = \frac{E}{E_{rev}}$ - (7)
- Faradaic efficiency: $\varepsilon_F = \frac{i}{i_{theo}}$ - (8)
- Fuel utilization: $U = \frac{m_{reacted}}{m_{input}}$ - (9)

- Heating value efficiency: $\varepsilon_H = \dfrac{\Delta H_r}{\Delta H_c}$ - (10)

where $\Delta\bar{h}$ is the enthalpy of reaction of the fuel, i_{theo} is the theoretical current density, $m_{reacted}$ and m_{input} are mole numbers of the reacted and input fuel respectively.

The overall efficiency can be calculated as: $\varepsilon_{fc} = \varepsilon_r \cdot \varepsilon_V \cdot \varepsilon_F \cdot U \cdot \varepsilon_H$ - (11)

2.4.3 Engineering Thermodynamics:

Thermodynamics is the study of the conversion of energy from one form to another. Goals are to produce heat or work, either electrical or mechanical in form. In fuel, the energy is bound in chemical form. Devices such as fuel cells and heat engines release energy by chemical reactions, converting it into electricity or heat. The first and second laws of thermodynamics introduced briefly below constitute the fundamental theoretical basis of fuel cell efficiency calculation and the Nernst equation.

The First Law of Thermodynamics:[2] energy is conserved in a thermodynamic system. In other words, the change in total energy of a system is equal to the heat added to the system minus the work done by the system as: $E = Q - W$. For a closed system or a control mass e.g. piston-cylinder system, the first law of thermodynamics can be written as $\Delta E = \Delta U + \Delta KE + \Delta PE$, where U is the internal energy, KE is the kinetic energy and PE is the potential energy. For an open system or a control volume, an additional flow energy (product of pressure and volume) PV is added to the total energy.

Define the property enthalpy by $H = U + PV$, for a stationary control volume under steady-flow conditions, the first law of thermodynamics becomes $Q - W = \Delta H$. A fuel cell can be regarded as a control volume, in which the work is done in the form of electron transfer across a potential difference.

The Second Law of Thermodynamics:[2] the second law defines the property *entropy*, a measure of the disorder in a system, which is expressed by $dS = (\frac{\delta Q}{T})_{rev}$. A process that does not generate entropy is called a reversible process if it can be performed and then returned to its initial state without leaving any traces on the surroundings. The Clausius inequality $\oint \frac{\delta Q}{T} \leq 0$ implies that for an isolated process, the entropy always tends to increase.

Heat Engines and Carnot Cycle:[5] the second law of thermodynamics deduced the so-called Carnot Limit for heat engines like steam and gas turbines. The Carnot Limit can be calculated via equation: $\text{maximum efficiency} = (T_1 - T_2)/T_1$, where T_1 is the temperature the heat engine is working at, and T_2 is the temperature of the cooling water in the system. Fortunately fuel cells are not subjected to the Carnot limit, for the energy is converted electrochemically without combustion or heat exchange.

2.4.4 Chemical Thermodynamics[2]

As is known, the Gibbs free energy is defined as the difference between the enthalpy of a chemical reaction and the product of absolute temperature with entropy, i.e. $G = H - TS$. Chemical reactions proceed in the direction that minimizes the Gibbs energy, so the change in Gibbs energy is negative as the reaction approaches equilibrium. At chemical equilibrium, the change in Gibbs energy is zero.

Substituting the first law of thermodynamics into the differential form of Gibbs energy, we obtain $dG = \delta Q - \delta W + PdV + VdP - TdS - SdT$. Applying the second law for a reversible process ($\delta Q = TdS$) and applying to a process at constant temperature and pressure yields $dG = -(\delta W - PdV)$.

Suppose that we examine a chemical reaction $\alpha A + \beta B \rightarrow \gamma C + \delta D$. By definition, the change of the Gibbs free energy is $\Delta G = \gamma \bar{g}_C + \delta \bar{g}_D - \alpha \bar{g}_A - \beta \bar{g}_B$. It also equals to

$$\Delta G = \Delta G^0 + RT \ln \frac{\alpha_C^{\gamma} \alpha_D^{\delta}}{\alpha_A^{\alpha} \alpha_B^{\beta}} \qquad \text{- (12)}$$

where ΔG^0 is the change of Gibbs free energy at the standard state, and the α 's are the chemical activities of reactants and products.

The electrochemical work done by fuel cells is a type of non-expansion work $(dV = 0)$, therefore the maximum work attainable is: $\delta W_e = -\Delta G = n_e FE$. - (13)

Combining equation (12) and (13), we arrive at the Nernst equation, $E = E^0 - RT \ln \frac{\alpha_C^{\gamma} \alpha_D^{\delta}}{\alpha_A^{\alpha} \alpha_B^{\beta}}$, which describes the relation among the cell terminal potential, the cell reversible potential and the chemical activities of reactant species.

2.5 Fuel Cell Electrode Kinetics

It is necessary to review some of the fundamental electrochemistry here due to the operation principle of fuel cells. In particular, the electrode kinetics is the controlling mechanism that incorporates the ion conduction and mass transport together in a fuel cell, the basics of which are given in the following sections.

2.5.1 General Electrode Kinetics

2.5.1.1 Rate-Determining Step

2.5.1.1.1 Rate-Determining Step for Consecutive and Parallel Reactions

The efficiency of an electrochemical device depend on the values of rate constant, (i.e. the velocity of the rate-determining step), although other factors such as adsorptive properties of

reactants and intermolecular forces among the species adsorbed on the electrode also play an important role.

Eyring et al. showed that the rate-determining step is the step that has the highest standard free energy of the activated state with respect to the initial state.[7] For a consecutive reaction, the velocity of the reaction is approximately the same as the rate-determining step, i.e. $\frac{1}{v} \approx \frac{1}{v_g}$ while all other steps before and after the rate-determining step are virtually in equilibrium. For a parallel reaction, the most rapid step of the parallel paths determines the rate of the overall reaction. These can be easily seen in the roadblock analog shown in Figure 2-5.

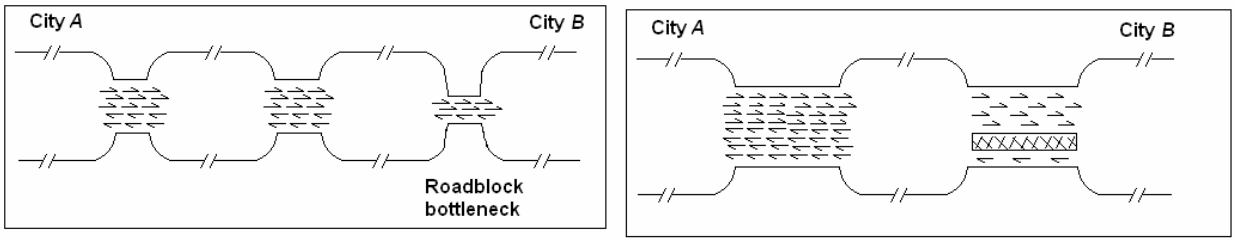

(a) (b)

Figure 2-5. The electric circuit analog for consecutive (a) and parallel (b) reactions.[7]

2.5.1.1.2 Classifications of Electrode Processes

The classifications of electrode processes are in compliance with the types of rate-determining steps that are listed in Table 2-2.

Table 2-2. Types of rate-determining steps.[7]

	Types of rate-determining step				
Mass-transport control	Diffusion	Diffusion-convection	Ohmic		
Heterogeneous-step control	Charge transfer	Adsorption & desorption	Nucleation	Crystal growth	Surface diffusion
Homogeneous-step control	Chemical reactions in solution				

2.5.1.1.3 The overall rate-determining step for a PEMFC

Figure 2-6 compares the relative magnitudes of the overpotentials in a PEMFC. It shows that the cathode activation loss is the largest overpotential over the entire current density region and membrane loss is the second largest one next to activation overpotential. Hence the cathode activation is the rate-determining step of the whole PEMFC electrochemical process when the current density is low. As the current density increases, the process can be regarded as two rate-determining steps connected in series, which implies that two main irreversible losses – cathode activation overpotential and membrane loss – have to be taken into consideration carefully at the same time during the modeling work. When the current density is high enough, the cathode electrochemical reactions will be controlled by the mass transport limitations; therefore mass transport is the only rate-determining step in this case.

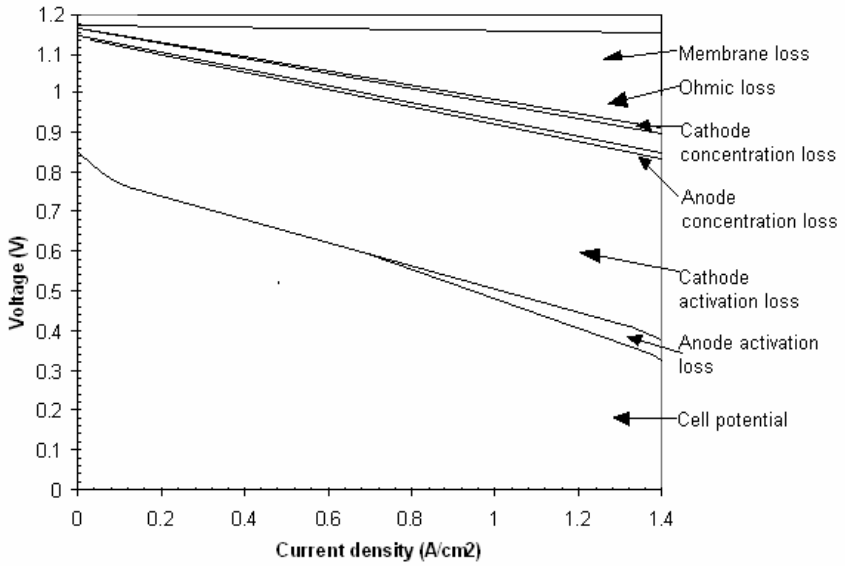

Figure 2-6. Comparison of the relative magnitudes of overpotentials in a PEMFC.[6]

2.5.1.2 Tafel Relation

As a result of experiments, Tafel reported in 1905 that the activation overpotential at the surface of an electrode follows a similar pattern in a large variety of electrochemical reactions.[5] If a graph is plotted of activation overpotential against logarithm of current density, the graph approximates a straight line, as shown in Figure 2-7. For most of the overpotential, its value can be calculated via the equation:[5]

$$\eta = a\log\frac{i}{i_0} = A\ln\frac{i}{i_0} \qquad \text{- (14)}$$

where i_0 is the exchange current density at which the reaction is taken as a reversible process, small a and large A express the slopes of the straight line in the case of log and natural log operation respectively, both named as "Tafel slope". It can be seen that a smaller Tafel slope corresponds to a faster electrochemical reaction as well as a larger exchange current density i_0. The relation between the Tafel slope a and symmetry factor β is $a = \frac{2.303RT}{n\beta F}$.[5]

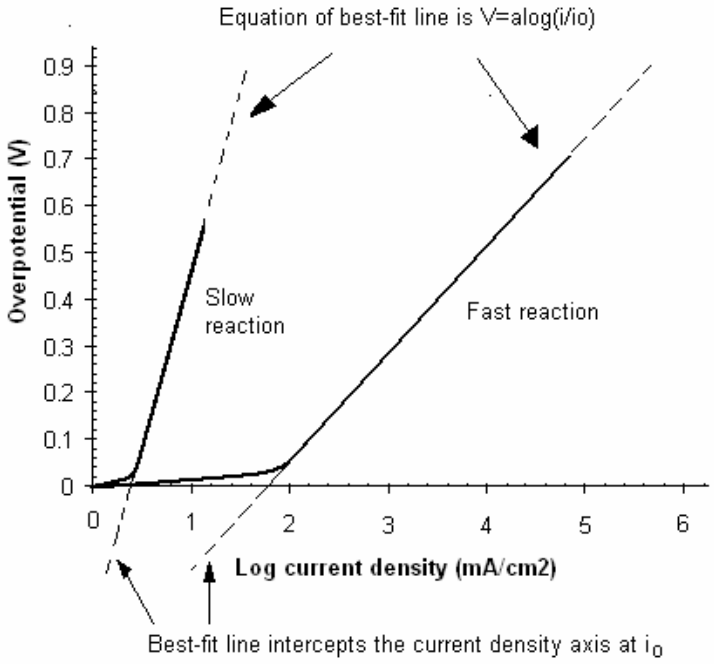

Figure 2-7. A typical Tafel plot.[5]

2.5.1.3 Symmetry Factor β and (Charge) Transfer Coefficient α

2.5.1.3.1 Clarification of β and α

There has been some confusion regarding to the terms of "symmetry factor" and "(charge) transfer coefficient" in electrochemistry books and papers. One may encounter nomenclature such as "symmetry factor", β;[7] "charge transfer coefficient", α;[8] and "transfer coefficient" that is also denoted as α.[9] These three terms had been used by some researchers to express the same mechanistic significance (if any), but the other researches distinguished them in their work clearly.[10-13]

For example, "charge transfer coefficient" α, "symmetry factor" β and "transfer coefficient" α were adopted to represent the slope of the energy profile in the transition state zone in a single-electron transfer step (see Figure 2-8), or in other words, to represent the proportion of the electrical energy applied that is harnessed in changing the rate of an electrochemical reaction.[8]

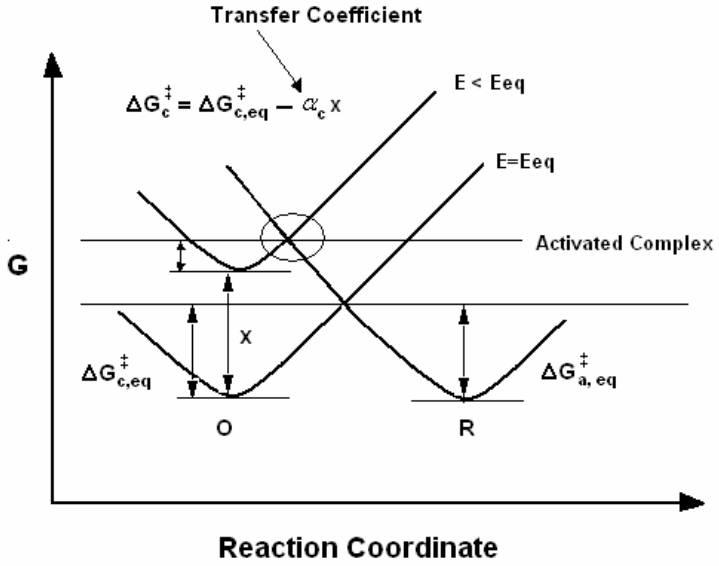

Figure 2-8. Significance of charge transfer coefficient α or symmetry factor β.[8]

The values of β or α for a single-electron transfer are usually taken to vary between 0 and 1, depending on the symmetry of the transition state. Experimentally, both β and α has been determined to be approximately 0.5 for metal electrodes and no coupling between electrode and reactant species. For other electrodes and strongly interacting systems, α and β can be smaller or larger than 1/2, as shown in Figure 2-9.

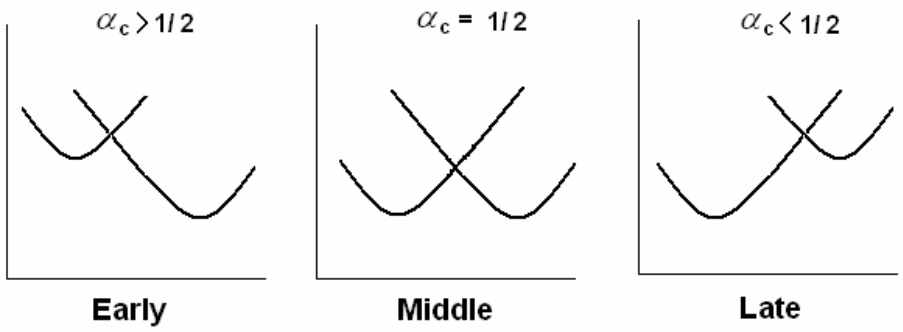

Figure 2-9. Values of charge transfer coefficient.[8]

However, according to A. Damjanovic et al.[13] in 1986, symmetry factor β is for the first electron transfer step as the rate-determining and the transfer coefficient α is for the slow electrochemical step following that first electron step as rate-determining, the details of which will be given at a later time. But in several electrochemistry books, the symmetry factor β was more likely to be used for single-electron transfer and the transfer coefficient α was used as the composite exponential terms in the rate constant equation for multiple-step electron transfers. If multiple electron transfers are involved in an electrode reaction, it is unlikely that they occur in one single step, which essentially means that multiple electron transfers correspond to multi-step electron reaction. It is worth mentioning that it is difficult to draw any physical meaning from α and β for multi-step reactions, if the rate-limiting step does not involve charge transfer and one cannot measure the value of the parameters by electrochemical means.[9]

2.5.1.3.2 Dependences of Symmetry Factor β

It has been suggested that the symmetry factor β for the first electron transfer step as the rate-determining is not always a constant.[13] In fact, it may vary with the absolute temperature T and has two components:

$$\beta = \beta_H + \beta_S T \qquad \text{- (15)}$$

where the enthalpic component β_H is defined by the equation: $\beta_H = [\frac{d\Delta\overline{H}^{\neq}(E)}{EdE}]$ and the entropic compound β_S is defined by the equation $\beta_S = -[\frac{d\Delta\overline{S}^{\neq}}{dE}]$.

The Conway plot, which is represented by the relation: $\frac{d\ln i}{dE} = -\frac{(\beta_H + \beta_S T)F}{RT}$, can be utilized to obtain the value of the symmetry factor for a specific electrochemical reaction. This plot is composed of the data of the reciprocal Tafel slope versus reciprocal absolute temperature. For the oxygen reduction reaction (ORR) at platinum (Pt) electrodes, it was found that the symmetry factor β was nearly independent of temperature with $\beta = \beta_H + \beta_S T = 0.44 + 2.3\times10^{-4}T$ in $HClO_4$ and H_2SO_4 solutions,[14] as seen in Figure 2-10. However, β was reported proportional to the absolute temperature as $\beta = \beta_0 T$ for ORR at Pt electrode in concentrated H_3PO_4 solutions.[14]

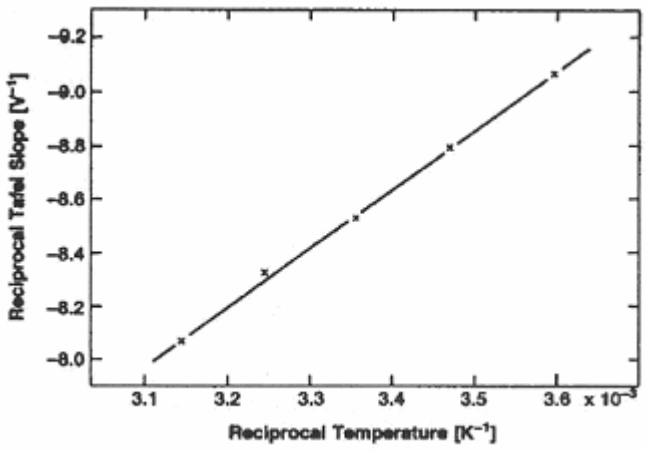

Figure 2-10. The Conway plot for ORR at Pt electrodes.[14]

A detailed theoretical treatment of the electron-transfer process, the Marcus theory, has shown that the cathodic and anodic symmetry factors are linear functions of potential as:[15]

$$\beta_c = \beta = \frac{\partial(\Delta G_c^{\neq})}{\partial(FE)} = \frac{1}{2} + \frac{FE - (w_0 - w_r)}{2\lambda} \qquad \text{- (16)}$$

$$\beta_a = 1 - \beta = \frac{\partial(\Delta G_a^{\neq})}{\partial(FE)} = \frac{1}{2} - \frac{FE - (w_0 - w_r)}{2\lambda} \qquad \text{- (17)}$$

where w_0 and w_r are the work required to bring the oxidized species O and reduced species R from bulk solution to the electrode, and λ is the energy required to reorganize O to the conformation of R, all of which are constants for a specific electrochemical system.

2.5.1.4 Butler-Volmer Equation[2]

2.5.1.4.1 Single-Electron Transfer

Consider a single-electron transfer reaction: $O + e^- \Leftrightarrow R$, the current generated from this redox reaction, I (Ampere), or current density, i (A/cm^2), can be calculated by equation (18) :

$$I = nA \cdot F \cdot j \text{ or } i = nF \cdot j \qquad \text{- (18)}$$

where n is the number of electrons transferred per electrochemical act and equals to one for single-electron transfer, A is the effective electrode area, F is Faraday's constant, and j is the net velocity (or reaction rate) of the single-electron transfer reaction, which equals to the difference between the forward and back reaction velocities, i.e. $j = j_f - j_b$.

If we suppose that the backward and forward reaction velocity is proportional to the concentration of its reactant, we have:

$$i = F(k_f c_{ox} - k_b c_{rd}) \qquad \text{- (19)}$$

Here, c_{ox} and c_{rd} denote the concentrations of the oxidized and reduced reactant species, the heterogeneous rate coefficient k is a function of the Gibbs energy of activation, which can be calculated from the Arrhenius equation with k_B and h being the Boltzman's and Planck's constant respectively:

$$k = \frac{k_B T}{h} \exp(\frac{-\Delta \overline{G}^{\neq}}{RT}) \qquad \text{- (20)}$$

Because an electrochemical reaction occurs in the presence of an electric potential E, the Gibbs energy of activation includes both chemical and electrical terms:

$$\Delta \overline{G}^{\neq} = \Delta \overline{G}^{\neq}_{c,f} + \beta FE \qquad \textit{Cathode reduction} \qquad \text{- (21)}$$

$$\Delta \overline{G}^{\neq} = \Delta \overline{G}^{\neq}_{c,b} - (1-\beta)FE \qquad \textit{Anode oxidation} \qquad \text{- (22)}$$

Substituting equation (21) into equation (20), the forward rate coefficient k_f can be described by:

$$k_f = \frac{k_B T}{h} \exp(\frac{-\Delta \overline{G}^{\neq}_{c,f}}{RT}) \exp(\frac{-\beta FE}{RT}) \qquad \text{- (23)}$$

If we define the overpotential η as the actual potential E minus the reversible potential E_{rev}, define $k_{o,f} = \frac{k_B T}{h} \exp(\frac{-\Delta \overline{G}^{\neq}_{c,f}}{RT}) \exp(\frac{-\beta FE_{rev}}{RT})$ and $k_{o,b} = \frac{k_B T}{h} \exp(\frac{-\Delta \overline{G}^{\neq}_{c,b}}{RT}) \exp\frac{(1-\beta)FE_{rev}}{RT}$, and rearrange above equations, the current density i is given by:

$$i = Fc_{ox} k_{o,f} \exp(\frac{-\beta F\eta}{RT}) - Fc_{rd} k_{o,b} \exp(\frac{(1-\beta)F\eta}{RT}) \qquad \text{- (24)}$$

When the electrode is in equilibrium and at its reversible potential, the overpotential and the external current are both zero. Hence the exchange current density i_0 is equal to:

$$i_0 = Fc_{ox}k_{o,f} = Fc_{rd}k_{o,b} \quad \text{- (25)}$$

By replacing the terms in equation (24) with i_0, we obtain the famous Butler-Volmer equation for single-electron transfer as:

$$i = i_0[\exp(\frac{-\beta F\eta}{RT}) - \exp(\frac{(1-\beta)F\eta}{RT})] \quad \text{- (26)}$$

2.5.1.4.2 Multi-Step Electrode Reaction

The Butler-Volmer equation above applies only to the electrode reaction taking place in one single-electron transfer step. One needs to construct a generalized Butler-Volmer equation or sometimes known as the kinetic law for the multi-step electrode reaction usually written as a sequence of bi-directional reactions, one of which is rate determining.

Again consider a single-electron transfer reaction $O + e^- \Leftrightarrow R$.[16] It has been shown that the electrochemical activity of an electron with potential E is proportional to $\exp(-FE/RT)$. But from thermodynamic viewpoints, the rate of the reductive process $O + e^- \rightarrow R$ is actually proportional to $\exp(-\beta FE/RT)$. Accordingly, the corrective activity dependence should be given as: $R_{rd} \propto a_O a_e^{\ \beta}$, where R_{rd} is the reductive reaction rate, a_O and $a_e^{\ \beta}$ are the chemical activities of oxidized species O and electrons respectively. Hence the equation $O + \beta e^- \Leftrightarrow R - (1-\beta)e^-$ describes the process better, with β and $(1-\beta)$ taken as the virtual stoichiometric coefficients that represent the reaction orders of the single-electron transfer.

Now we can proceed to study the kinetics of multi-step electrode reactions. With the aid of a seven-step implementation which involves the rearrangements of the reaction equations before and after the single-electron transfer rate-determining step, a stoichiokinetic equation accounting

for the total complex electrode reaction can be established. Consequently, the generalized Butler-Volmer equation is formulated as below:[16]

$$i = vFk[c_{rd} \exp\frac{-\alpha_{rd} FE}{RT} - c_{ox} \exp\frac{\alpha_{ox} FE}{RT}] \qquad \text{- (27)}$$

where c_{ox} and c_{rd} are concentrations or groups of concentration terms and k is the composite heterogeneous rate constant. The α_{ox} and α_{rd} terms are the oxidative and reductive transfer coefficients which sum to the integer v that is not necessarily equal to n, the net number of electrons transferred in the complex electrode reaction.

Correspondingly, the exchange current density of the multi-step electrode reaction can be written as:[16]

$$i_0 = i_{c,rev} = vFkc_{rd} \exp\frac{-\alpha_{rd} FE_{rev}}{RT} = -i_{a,rev} = vFkc_{ox} \exp\frac{\alpha_{ox} FE_{rev}}{RT} \qquad \text{- (28)}$$

2.5.2 Review of the Electrode Kinetics of Oxygen Reduction Reaction (ORR) on Pt Electrode in Acid Solutions

Although the electrolyte is the solid ionomer in a PEMFC, there are some similarities that exist between the ORR at Pt/ionomer interface and ORR at Pt/acid solution interface, the latter of which has been intensively investigated and could provide us some useful background for the electrode kinetics of PEMFCs.

The study of ORR on platinum (Pt), palladium (Pd) and iridium (Ir) electrodes in acid and alkaline solutions had been in the focus between the 1960's and 1980's. A. Damjanovic, D. Sepa, M. A. Genshaw, J. Bockris et al. are the electrochemists who made major contributions in this area.[12-14,17-26] Among the three electrodes, the Pd electrode is supposed to behave the same as the Pt electrode, but Ir electrode has been reported to behave differently from the other two.

For the kinetics of ORR on Pt electrode in acid and alkaline solutions, four points seem to be agreed upon by most workers.[17] First, the kinetics at pre-reduced, oxide free electrodes is qualitatively different from those at electrodes covered by thin oxide films formed anodically at higher potentials. Second, in both acid and alkaline solutions, steady state kinetics is characterized by two nearly linear Tafel regions. Third, in the low current density region with the Tafel slope of -60mV/decade (equal to $-2.3RT/F$), there is intermediate coverage with oxygen species, which increases linearly with electrode potential. Fourth, in both current density regions, the reaction order with respect to molecular oxygen is one.

2.5.2.1 Reaction Plots and Parameters

In electrochemistry, the electrode kinetics for an electrochemical reaction is partially characterized by plots such as Tafel plot, Conway plot, and Arrhenius plot and their corresponding parameters. The dependences of specified potential or current density on pH, reactants concentration and temperature could help restricting the possible reaction pathways.

The important reaction parameters for ORR on oxide-free Pt electrode in acid and alkaline solutions are summarized in Table 2-3. The reaction mechanisms can be analyzed on the basis of the values of these parameters.

Table 2-3. Kinetic data for ORR on pre-reduced Pt electrodes, data were not corrected for the roughness of the electrode surface.[17]

Parameters	Acid		Alkaline	
	Low current density region	High current density region	Low current density region	High current density region
$dE/d\log i$ (mV/decade)	-60	-120	-60	-120
dE/dpH (mV/unit)	-90	-120	-30	0
$dE/d\log p_{O_2}$ (mV/decade)	60	120	60	120

The transition potential at which the Tafel slope changes, E_T, is also a valuable parameter for reaction pathway analysis. It physically reflects the potential when the coverage with reaction intermediate θ falls to a very low value (0.05). As the current density is decreased, a rest

potential, E_R, is reached beyond which any further decrease of current does not affect the potential.

It is generally believed that the rest potentials are mixed electrode potentials involving the O_2 reduction as one component and an anodic process as the other component. It was suggested this anodic process is platinum dissolution, particularly in the pH range of 0 to 3 and 11 to 14. In the intermediate pH region, residual impurities in the acid or alkaline solutions may be sufficient to provide an alternative anodic component of the mixed potentials.

The positions of E_T and E_R in a Tafel plot are shown in Figure 2-11.

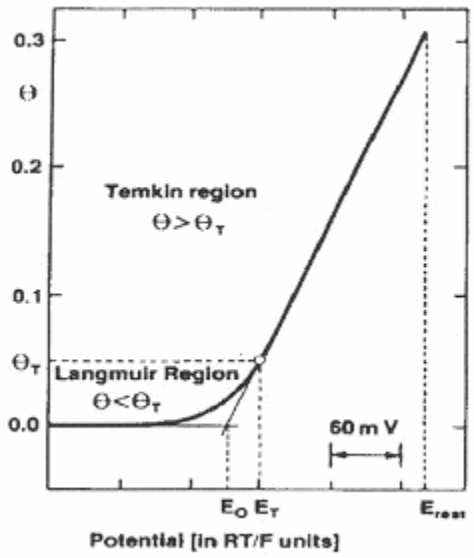

Figure 2-11. The relative positions of E_T and E_R in a Tafel plot.[18]

The trends of change of E_T and E_R with pH of the electrolyte for ORR on Pt electrode in acid and alkaline solutions are shown in Table 2-4.

Table 2-4. Change of E_T and E_R for ORR on pre-reduced Pt electrodes.[24,26]

Parameters	Acid	Alkaline
dE_T / dpH (mV/unit)	-60	60
di_T / dpH (mV/unit)	-1/2	1/2
dE_R / dpH (mV/unit)	-60	-60

Combing above data with reaction order analysis, the generally accepted kinetics equations for ORR on Pt electrode in acid and alkaline solutions at high and low current densities are: [24, 25]

Acid:

$$i = k_1 nFp_{O_2}[H^+]^{3/2} \exp[-FE/(RT)] \quad \text{- (29)}$$

$$i = k_2 nFp_{O_2}[H^+] \exp[-\beta FE/(RT)], \text{ where } \beta = 1/2 \quad \text{- (30)}$$

Alkaline:

$$i = k_3 nFp_{O_2}[OH^-]^{-1/2} \exp[-FE/(RT)] \quad \text{- (31)}$$

$$i = k_4 nFp_{O_2} \exp[-FE/(2RT)] \quad \text{- (32)}$$

2.5.2.2 Reaction Pathways

The method of the rotating-disk electrode with a concentric ring was used by A. Damjanovic, M. Genshaw and J. Bockris to examine the reaction pathways of ORR on Pt electrode.[23] A plot of I_d / I_r versus $\varpi^{-1/2}$ was made based on equation 33:

$$\frac{I_d}{I_r} = \frac{x+1}{N} + \frac{K(x+2)}{\varpi^{1/2}} \quad \text{- (33)}$$

where I_d and I_r are the measured currents at the disk and the ring electrode, ϖ is the rate of disk rotation, N is a geometric constant (~0.35), x is the ratio of the current at the disk for the reaction path which does not involve the formation of H_2O_2 to the current at the disk due only to the reduction of O_2 to H_2O_2, and K is proportional to the rate of further reduction of H_2O_2 at the

disk electrode. If the straight line has an intercept with the I_d / I_r axis greater than $1/N$, two parallel paths for oxygen reduction are present.

For oxygen reduction at oxide-free platinum electrodes in sulfuric acid solution, it turns out that hydrogen peroxide is produced in a path parallel to the main path of oxygen reduction which does not involve H_2O_2 as an intermediate. The O_2 to H_2O_2 reduction arises due to the adsorption of residual impurities of the solution at the Pt surface. Since the slope of the lines is zero, hydrogen peroxide is not further reduced to water.

In alkaline solution, the I_d / I_r plot reveals that two paths of oxygen reduction occur simultaneously at comparable rates (see Figure 2-12). One of these paths has hydrogen peroxide formed as an intermediate, which partially reduces further at the disk electrode.[23]

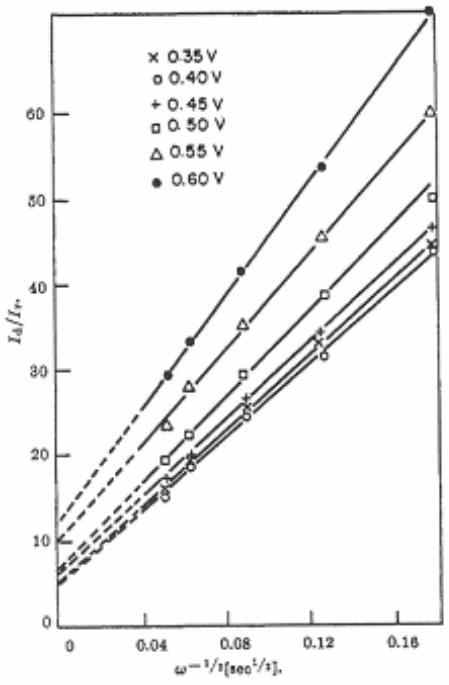

Figure 2-12. The plot of ratio of the current at disk to the current at the ring electrode vs. the rate of disk rotation, solution was 1N KOH.[23]

2.5.2.3 Rate-Determining Step

As shown in Figure 2-13, there are two linear regions in the Tafel plot of ORR on oxide-free Pt electrode in acid solutions. The slopes of -60 mV/decade and -120 mV/decade correspond to the low and high current density region respectively. Generally speaking, a change in Tafel slope for an electrochemical reaction implies the variation of the rate-determining step. In spite that the slope of -60 mV/decade is usually associated with a chemical step following first electron transfer step (ETS) as the rate determining, it was concluded by A. Damjanovic et al. that for ORR on Pt electrode in both acid and alkaline solutions, the first ETS was rate-controlling under Temkin conditions of adsorption with respect to reaction intermediates in the low current density region and Langmuir conditions in the high current density region.[20]

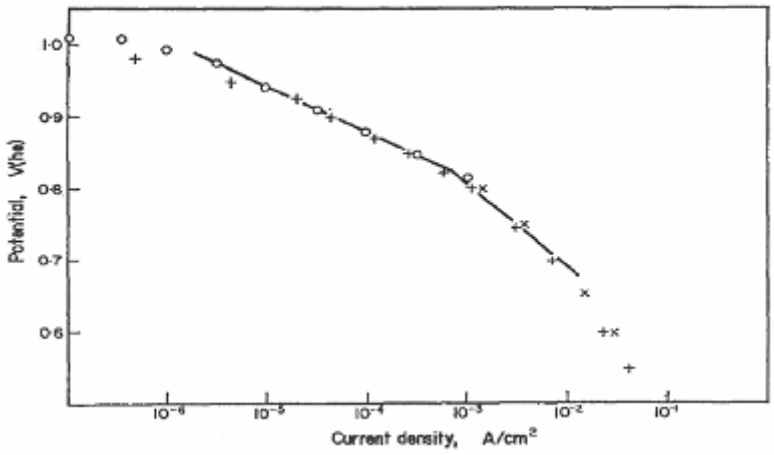

Figure 2-13. Current-Potential relation in acid solutions, o, stationary Pt wire electrode in $HClO_4$ solution (pH=1); + and ×, rotating Pt disk electrode in H_2SO_4 solution (pH=1).[20]

The difference of the Temkin and Langmuir condition depends on the homogeneity of the surface. Correspondingly, the Temkin and the Langmuir isotherm were derived based on different assumptions regarding the adsorbing surface, both of which describe the relations between the surface coverage with the temperature and adsorbent pressure, or in other words, the dependence of surface coverage on the enthalpy of adsorption. In general, the distribution of binding energies in the Temkin condition corresponds to a model of a heterogeneous surface and the Langmuir condition corresponds to a homogeneous surface with the same binding energy at

each adsorbing site. The equation of the Temkin isotherm is $\theta = -\alpha \ln(A\frac{p}{p_0})$,[27] while that of the Langmuir isotherm is $\theta = \frac{bp}{1+bp}$,[28] here $\alpha, b,$ and A are constants under the specific temperature and pressure conditions.

For ORR on Pt electrodes in acid solutions, the Temkin condition can hold only when the electrode potential is high or the overpotential is low. As the rate of the reaction increases, coverage by reaction intermediates decreases, and eventually reaches the level at which Langmuir conditions become dominant.[29,30]

2.5.2.4 The Effect of Coverage by Reaction Intermediates: ORR Thermodynamics

To explain the observed relations of the electrode potential with pH and oxygen partial pressure p_{O_2} as well as the proposed reaction pathways, A. Damjanovic, D. Sepa, and J. Brockis et al. studied extensively the ORR thermodynamics and the effect of surface coverage on the electrode surface by reaction intermediates.[19,29]

Focusing on the ORR at pre-reduced Pt electrode in acid solutions, it was determined that the surface coverage in the low current density region satisfies the following relationship:[29]

$$\theta(E, pH) = KE + K\frac{2.3RT}{F}pH + \theta_0 \qquad \text{- (34)}$$

where $K = 0.85V^{-1}$ is a constant, θ_0 is also a constant whose value depends on the choices of the reference potential, $\theta_0 = KE_0 = 0.85 \times 0.77 = 0.65$ when the potential refers to *s.h.e.* (standard hydrogen electrode), and E_0 is the potential to which θ extrapolates to zero in a solution of pH=0. The dependence of θ on potential E can be explained in terms of the induced heterogeneity model based on the effects of surface dipoles on work function and potential. The dependence of θ on pH is most likely related to the dependence of the onset of adsorption with oxygen species on pH.

At high current densities, the coverage with reaction intermediates is low and the electrode is under the Langmuir adsorption condition, when the change of activation energy contributed by chemical means, $\Delta G_c^{\neq}$, is independent of either θ or ΔE. At low current densities, θ is appreciable and the electrode is under the Temkin adsorption condition, when $\Delta G_c^{\neq}$ increases linearly with θ according to:[29]

$$\Delta G_c^{\neq} = \Delta G_o^{\neq} + \alpha r(\theta - \theta_T) \qquad \text{- (35)}$$

Here θ_T is the critical coverage (=0.05) at which the adsorption condition changes. It occurs at the critical potential E_T that is approximately 0.86V *h.e.*. A measure of the change of energy of adsorption of the adsorbed species with the total coverage $(\theta - \theta_T)$ is given by r and $r = \frac{F}{K}$. The symmetry factor for adsorption, α (this "α" is different from the normal charge transfer coefficient term or the one used as the composite transfer coefficient in a multi-step electrode reaction), is usually taken as 0.5. At $\theta > \theta_T$, θ increases linearly with the electrode potential E, hence $\Delta G_c^{\neq}$ becomes potential dependent as:[29]

$$\Delta G_c^{\neq} = \Delta G_o^{\neq} + \alpha F(E - E_T) \qquad \text{- (36)}$$

Only at potentials higher than E_T does $\Delta G_c^{\neq}$ increase with E at high current densities, when $\theta < \theta_T$, the above equation does not hold any longer and $\Delta G_c^{\neq} = \Delta G_o^{\neq} \neq f(E)$.

After combining the above analysis and applying the Arrhenius equation, the current density at low current densities can be expressed as:

$$i = k_1 nFp_{O_2}[H^+]^{3/2} \exp[-(\alpha+\beta)FE/(RT)], \text{ where } \alpha = 1/2, \beta = 1/2 \quad -(37)$$

The current density at high current densities is:

$$i = k_2 nFp_{O_2}[H^+] \exp[-\beta FE/(RT)], \text{ where } \beta = 1/2 \quad -(38)$$

2.6 Proton Exchange Membrane Fuel Cell (PEMFC)

2.6.1 Advantages of PEMFCs in Automobile Applications

The candidate power sources for the hybrid electric vehicles (HEVs), PEMFCs are considered to be the most promising type in comparison with rechargeable batteries and other hybrid sources. PEMFCs can provide a driving range and refuel time comparable to the conventional automobiles in contrast with the relatively short-range operation and long recharging time of battery-powered automobiles. What's more, PEMFCs run on air in the terrestrial transportation systems with ambient or slightly higher pressure and use sulfonated solid polymer as the electrolyte, which makes them very suitable for transportation applications in terms of room temperature start-up, low temperature operation, easy construction and elimination of corrosion and electrolyte leakage problems.

2.6.2 Components of a PEMFC

Generally speaking, a PEMFC is composed of current collector, gas distributor and membrane electrode assembly (MEA). Among these components, the current collector is usually made of common metals with low electrical resistance such as copper or aluminum. The gas distributor, in the form of monopolar plate in a single cell and a bipolar plate in a PEMFC stack, is injection-molded from a graphite plate with grooved gas channels to transport the reactant gases to the reaction sites. The membrane electrode assembly is an assembly where the electrochemical reactions occur. The components of a MEA and their corresponding functions are listed below and see the SEM image of the MEA cross-section by Siegel et al. in Figure 2-14 for reference.[31]

A. Gas diffusion layer which is currently made from carbon fiber or carbon cloth and functions to wick away liquid water, transport reactants of H_2 and O_2 and conduct electrons. Its thickness is normally between 200 and 300μm.

B. Catalyst layer which is the region where the membrane and the electrodes overlap and the H_2 oxidation or O_2 reduction reaction occurs. It allows electron and ion conduction at the same time. Catalyst layer and gas diffusion layer together compose the electrode. The typical thickness of the catalyst layer in a PEMFC is about 10μm.

C. Membrane which can transport the hydrogen ions with the presence of water but is impermeable to gas and electrons. The membranes should possess good chemical, mechanical and thermal properties in order to withstand the fuel cell reaction environment. The thickness of membrane for hydrogen-air fuel cells is around 50μm.

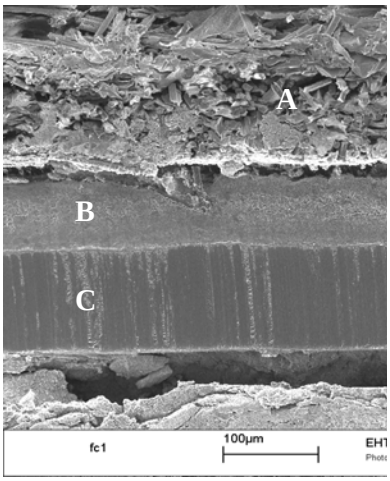

Figure 2-14. The SEM image of the MEA cross-section.[31]

2.6.3 Oxygen Reduction Reaction Mechanisms at the Pt/ionomer Interface

As mentioned in the previous section, the ORR kinetics on the Pt/ionomer interface has not been thoroughly studied. Nevertheless, similar to the ORR on Pt in acid solutions such as $HClO_4$ and

H_2SO_4 solutions, the Tafel plot of ORR on Pt with the polymer electrolyte shows two distinct slopes for the low and high current density region respectively, as seen in Figure 2-15 below.[32]

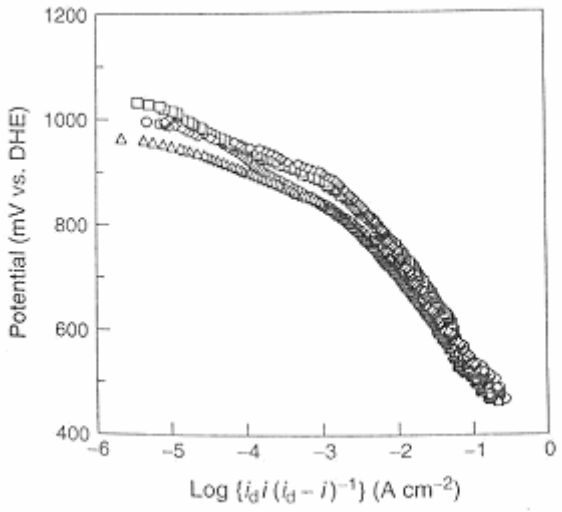

Figure 2-15. The Tafel plot of ORR at the Pt/ionomer interface.[32]

A. Parthasarathy, B. Dave, S. Srinivasan et al. stated that ORR on Pt/ionomer interface is overall a 4-electron reduction reaction for both regions with steps including oxygen gas adsorption, charge transfer, breaking of the O-O bond and desorption based on the analysis by slow scan voltammetry.[32] However, Mitsushima et al. suggested that the difference of Tafel slopes at the low and high current density region should be interpreted by the number of electrons transferred in the oxygen reduction reaction, with a 2-electron reduction corresponding to the low current density region and 4-electron reduction to the high current density region.[32] In spite of the discrepancies, the most accepted hydrogen oxidation and 4-electron oxygen reduction reaction mechanisms in a PEMFC are:[6]

The anode side:

$$2Pt(s) + H_2 \rightarrow Pt\text{-}H_{ads} + Pt\text{-}H_{ads} \qquad \textit{slow adsorption}$$

$$Pt\text{-}H_{ads} \rightarrow H^+ + e^- + Pt(s) \qquad \textit{fast reaction}$$

The cathode side (proposed mechanisms):

$Pt(s) + O_2 \rightarrow Pt\cdot\cdot O_2$ *fast adsorption*

$Pt\cdot\cdot O_2 + H^+ + e^- \rightarrow Pt\cdot\cdot O_2H$ *rate determining step*

$Pt\cdot\cdot O_2H + 3H^+ + 3e^- \rightarrow Pt(s) + 2H_2O$ *via unknown fast steps*

The **overall reaction** is: $2H_2 + O_2 \rightarrow 2H_2O$

The unique features of ORR at the Pt/ionomer interface should be kept in mind when its kinetics is being studied. First, utilizing Pt or Pt alloy nanoparticles impregnated on the carbon cloth or carbon paper diffuser brings up the issue of Pt catalyst structure and morphology that play an important role on catalyst activity. Second, oxygen permeability and proton concentration in the membrane affect the kinetics of the oxygen reduction reaction.[32] The product of solubility and diffusivity of O_2 expresses the permeability of O_2 in a polymer membrane, which increases when the temperature and ion exchange capacity (IEC) of the membrane are increased. Third, the above two aspects can be reflected in an important electrokinetic variable, i.e. exchange current density i_0, which can be expressed by equation $i_0 = nFk[P_{O2}]^n[H+]^m$,[32] and experimentally determined by extrapolating the linear region of the Tafel plot to the axis of current density (see Figure 2-16).[9]

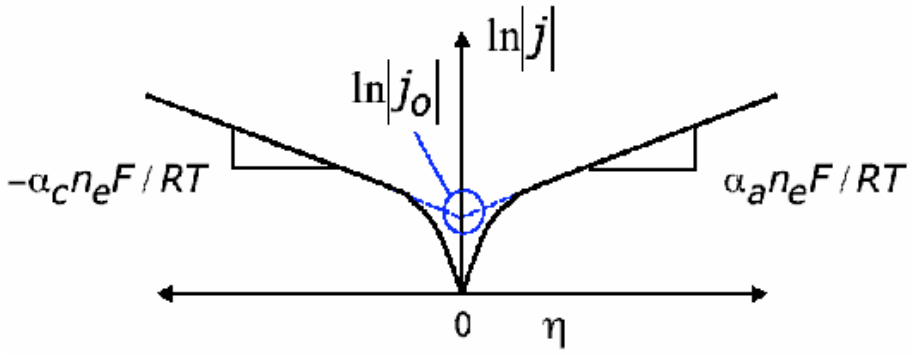

Figure 2-16. The determination of the exchange current density in a Tafel plot.[9]

2.6.4 Primary Characteristics to Describe a PEMFC

The primary characteristics to describe the performance of a PEMFC are polarization curve and power curve (shown in Figure 2-17), limiting current density i_l and local current density distribution. As for the transient state, the voltage-time behavior, start-stop performance and the performance under mechanical stress or cyclic operating conditions are usually concerned.

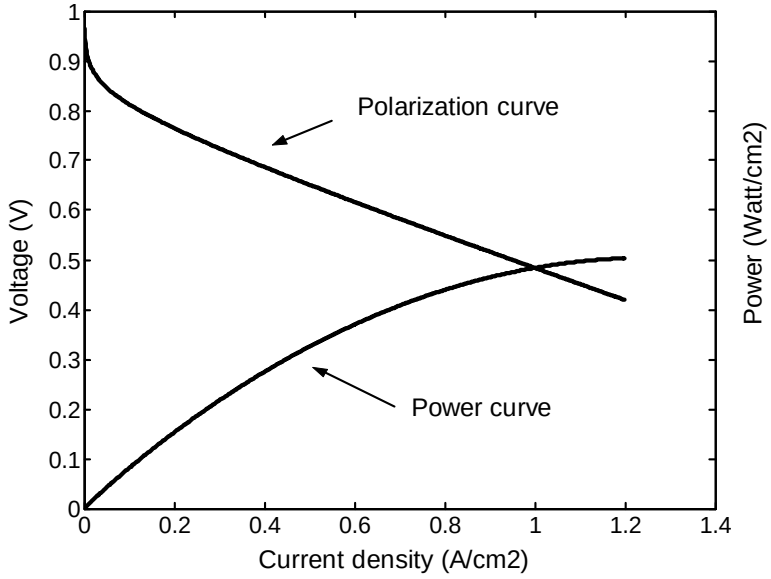

Figure 2-17. The polarization curve and power curve of a PEMFC.

2.7 PEMFC Mathematical Modeling – Performance Models

2.7.1 The Significance of Mathematical Modeling

As is known, many phenomena occur in a PEMFC during the generation of power, including electrochemical reactions, gas and liquid transport, phase change, mechanical stress and deformations, etc. Hence the study of PEMFCs has an interdisciplinary nature, involving the knowledge of electrochemistry, thermodynamics, fluid mechanics, transport phenomena, polymer science and so on.

The proton exchange membrane fuel cell requires a tailored design of the MEA for optimal catalyst localization, water and heat management and gas-transport characteristics, and the membrane conductivity. Good manipulation of the operating conditions for cell temperature, pressure, reactant stoichiometry and gas compositions are desired in order to achieve satisfactory performance from the cell. One method of optimizing performance is by analyzing the experiment results. However, the interplay of the various phenomena and the large quantity of variables make the effects of the individual parameters hard to isolate experimentally. To make thing worse, in-situ measurements in a PEMFC are extremely difficult due to the compactness of its components and the ease of disturbing the original distributions by artificial or instrumental factors. Consequently the mathematical modeling is believed to be a more appropriate way to optimize performance. Mapping of the cell variables and fluxes can be obtained by simulating the real PEMFCs under operating conditions with the aid of computer, which provides a good guidance for further operation and optimization design.

2.7.2 General Modeling Assumptions

The basic conservation laws of mass, momentum, species and energy constitute the basis for PEMFC modeling. There have been more than one hundred sets of models proposed in the literature thus far, with differences in the specifications of the model domains, parameters (the constitutive equations), assumptions, and solution techniques.[35- 68]

To avoid the redundancy in the next review section, if not mentioned, the models imposed the same general assumptions including: 1. The gas mixture in the gas channel is taken as ideal and compressible, 2. The electrode (gas diffusers), membrane and catalyst layers are assumed to be isotropic materials, 3. The gaseous O_2 has to be dissolved in the polymer phase first to be reduced at the cathode catalyst/membrane interface, 4. The water product of the oxygen reduction reaction is assumed to be in the form of liquid, 5. The local liquid water and water vapor is in transient equilibrium, 6. The local heat conductivities of the solid phase, gaseous phase and liquid phase are assumed infinite which means the solid/gaseous/liquid interface always reaches the same degree of temperature.

2.7.3 Summarized Model Governing Equations in the Vector Notation

The general model governing equations for material balance and transport phenomena in a PEMFC are summarized in Table 2-5.

Table 2-5. The general equations used in a PEMFC modeling

Balance of	Equation name	Equation in vector form
Mass	Continuity equation	$\frac{\partial \rho}{\partial t} + \nabla \cdot (\rho \vec{V}) = S_m$
Momentum	Navier-stokes equation	$\rho[\frac{\partial \vec{V}}{\partial t} + (\vec{V} \cdot \nabla)\vec{V}] = -\nabla p + \nabla[(\lambda + 2\mu)\nabla \cdot \vec{V}]$, [33] $-\nabla \times [\mu(\nabla \times \vec{V})] + \vec{F} + S_{me}$
Species	Stefan-Maxwell equation	$\nabla \cdot x_i = -\sum_{j=1}^{n-1} \frac{x_i x_j}{D_{ij}} (\vec{V}_i - \vec{V}_j)$, [6]
Energy		$\rho C_p \frac{dT}{dt} = \frac{dp}{dt} + \nabla \cdot \nabla (kT) + \mu\phi$, [34]

Transport of	Equation name	Equation in vector form
Proton in membrane	Nernst-Planck equation	$\vec{N}_i = -z_i \frac{F}{RT} D_i c_i \nabla \Phi - D_i \nabla c_i + c_i \vec{v}$, [5]
Liquid water in membrane	Schogel equation	$\vec{N}_{w,n} = -c_w \frac{k_\Phi}{\mu_l} c_H + F \nabla \Phi - c_w \frac{k_p}{\mu_l} \nabla p$, [6]
Electrochemistry	Bulter-Volmer equation	$i = i_0[\exp(\frac{\alpha_a F}{RT} \eta_{act}) - \exp(-\frac{\alpha_c F}{RT} \eta_{act})]$, [6]

2.7.4 Development of Performance Models

Like other types of simulation work, the development of PEMFC performance model has undergone the processes of one-dimensional to multi-dimensional, many assumptions to fewer assumptions, single (gaseous) phase to two phase (gas and liquid), and describing phenomena

from macro-homogenous to microscopic-inhomogeneous points of view. It should be mentioned that although nearly all of the presented models exhibited good agreement between the model predictions and the experimental data, many of them implemented the artificial adjustment of model parameters.

The one-dimensional models were mainly proposed in the early 1990's, often just focusing on the gas diffusion layer (GDL) and catalyst layer. Most of the one-dimensional models were isothermal, steady-state models of the MEA, cathode or complete cell (very few such models) with assumptions of fully humidified membrane and no interactions existent between gas and liquid phase.[35- 47]

The two-dimensional models began to emerge after 1998. Some developments such as application of multiphase mixture model (e.g. "Dusty-gas" model), modeling of newly introduced "interdigitated" gas distributors[49- 53] and consideration of temperature as one of the primary variables (nonisothermal model) were brought into stage. Computational fluid dynamics codes were utilized by researchers to solve the two-dimensional models.

The first three-dimensional model was presented by Dutta et al. in 2000.[57] Berning, Djilali and Li et al. have also developed steady-state, three-dimensional, nonisothermal models for PEMFCs recently.[54] In their models, two-phase flow in the gas channel was addressed as well as the impact of the temperature profiles within the cell. The nature of three-dimensional simulation allows the models to account for the variations of parameters in plane and along the gas channel, which could give a more accurate description of the phenomena occurring in a PEMFC. Unfortunately these advantages were obtained with the cost of model complexity, though commercial computational software such as "Fluent" and "CFX 5.0" was utilized to help solve the models.

2.7.5 Review of Steady-State Models

For the sake of brevity, only the models published after 1990's are reviewed in this dissertation. Primarily the models are sorted in chronological order, but the order is sometimes adjusted according to the connections between the models (such as papers from the same authors).

2.7.5.1 One-Dimensional Models

Before the 1990's, most of the models focused only on the gas-diffusion electrode or ion conducting membrane. In 1990, Bernardi proposed a simple one-dimensional, steady-state, isothermal model of water balance for solid polymer electrolyte fuel cells.[35] This model assumed that there was no free liquid water in the pores of the electrode. Therefore it only consisted of the mass balance equations for water vapor transport in the electrode. The membrane was assumed very thin with uniform liquid distribution. Finally the calculated results of the current density as a function of temperature, gas stream pressure, stoichiometric ratio and humidification were presented.

Following that model, Bernardi and Verbrugge published a one-dimensional isothermal model of MEA in 1991.[36] In their model, a PEMFC cathode bonded to the membrane was simulated with detailed mathematical descriptions of the electrochemical reactions and the transport phenomena. They modified the traditional porous-electrode theory and addressed the "active catalyst layer" where the membrane phase and electrode overlap. Three sets of model equations for proton exchange membrane, active catalyst layer and gas-diffuser respectively were presented. Though their model was the first membrane-electrode model to include electro-osmotic convection, a few assumptions were still employed to simplify the modeling process. First, it was assumed that the membrane was always fully humidified. Second, the total gas pressure within the gas diffuser was taken to be constant. Third, only the wetted liquid pores were considered in the gas diffuser and throughout the diffuser, the gas phase was taken to be in equilibrium with the liquid-water phase. Fourth, the gas in the chamber was treated as well mixed and in equilibrium with liquid water present in the gas channel. Hence the gas composition was not affected by the humidification level of reactant gases entering the gas chamber and the depletion of the reactant, which lead to a conclusion that for a given stoichiometric ratio, the gas composition is independent of current density. Fifth, the volume fraction of gas pores in the active catalyst layer

was assumed to be uniform. The calculated results of the model suggested that at high current densities, only a very small portion of the active catalyst layer near the catalyst/gas diffuser interface could be utilized due to the dissolved-oxygen transport limitations. The liquid water velocity profiles in the membrane showed that liquid water transport could proceed in different directions under different current density regimes. There were no advantages to operate the PEMFC with a pressure differential at low current densities for the sake of possible cathode dehydration.

With the 1991 model as a stepping stone, Bernardi and Verbrugge developed a complete steady-state, one-dimensional, isothermal fuel cell model in 1992, which is one of the classical works on PEMFC modeling.[37] In this approach, the limiting factors of the cell performance (including ohmic and activation polarization losses, transport limitations and membrane dehydration) were investigated. The gaseous phase was not included in the model of the active catalyst layers since the PTFE solution was considered as wetting (or coating) carbon surfaces thoroughly during the electrode fabrication. Hence the oxygen, which was mixed with nitrogen and water vapor, entered the cathode gas chamber, transported through the porous gas diffuser, could only dissolve into the membrane phase of the active catalyst layer. The total gas pressure within the gas diffuser portion of the electrodes was assumed to be constant and equal to that the adjacent gas chamber. The gas pores of the diffuser were taken to be separate from the water pores and the gas phase pressure was allowed to be different from that of the aqueous phase. Again a fully hydrated membrane was considered. For the anode, the gas stream was assumed only consisting of the binary H_2-H_2O mixture, which indicated the liquid water velocity is constant and the hydraulic pressure profile is linear in the anode gas channel.

It is worth mentioning that in this work most of the model parameters and properties were obtained from independent experiments except the cathode kinetic parameters: the product of effective electrode area a with the reference exchange current density i_0^{ref} and the membrane hydraulic permeability k_p. The analysis indicated that the volume fraction of the cathode for gas transport must exceed 20% in order to avoid unacceptably low limiting current densities. Low hydraulic and electrokinetic permeability of the membrane were desired but the hydraulic permeability must be high enough so that the gas diffusion electrode can serve to retain water at

the anode side. Inefficiencies due to fuel crossover were shown to be insignificant at practical operating conditions. The Dow membrane showed higher performance due to its higher proton concentration and smaller, more abundant pores compared to Nafion membrane. The model also elucidated that the transport of dissolved gases in the membrane phase limited the utilization of the catalyst at both electrodes. For example, at high current densities like 880mA/cm^2, the dissolved oxygen only penetrated less than 0.04μm, which meant only 2% utilization of the cathode catalyst layer. Finally it was concluded that there are no external humidification requirements since the water produced at the cathode can satisfy the water requirement of the membrane.

Almost at the same time when Bernardi and Verbrugge presented their models, Springer et al. proposed a steady-state, one-dimensional, isothermal model for a complete PEMFC in 1991, which was the first model to account for dehumidified Nafion 117 membranes.[38] An experimentally determined isotherm by Springer et al. for water sorption into the membrane was used to convert water vapor activity to water content in the membrane at the anode interface. The gas composition in the anode and cathode flow channels was assumed to be uniform and saturated with water vapor at the humidifier temperatures. There were only concentration gradients and no total pressure gradients across the electrode. A weakness of this model was that the possibility of large excess of liquid water in the flow channels or within the electrode was not considered during modeling. The presence of liquid water was assumed as in the form of finely dispersed droplets with zero volume, having transport properties identical to those of water vapor. Hence only the cathodic overpotential loss and the ohmic loss of the membrane were calculated without considering the mass transport limitation. The phenomenon of membrane swelling was accounted for by applying the equivalent water concentration normalized to the thickness of a dry membrane. In addition to the theoretical modeling work, Springer et al. performed several experiments to determine the values of the model parameters using equipment such as 1H-pulsed gradient spin-echo NMR (PGSE-NMR). These parameters included water content as a function of water activity, proton inter- and intra-diffusion coefficient, proton conductivity and electro-osmotic drag as a function of water content. In spite of the good features of Springer et al.'s model, they ignored the pressure driven flow in the membrane. This might

have lead to the conclusion that there was no need to humidify the cathode feed stream, which deviated from the experimental observations.

In succession to above model, Springer et al. developed a steady-state, one-dimensional, isothermal model in 1993 for well-humidified PEMFCs operated to maximum current density with a range of cathode gas compositions.[39] This model took the gas transport limitations in the cathode diffuser into consideration, which was not discussed in their previous model. Experimental data were collected for a homemade thin-film Pt/C based catalyst layer bonded directly to the membrane and a separate catalyst-free hydrophobic backing layer. The electrode fabricated this way was different with the ionomer impregnated catalyzed gas diffusion electrode, in which the resolution of the catalyst and backing domains is not clear. The effect of gradual depletion of oxygen along the flow channel was accounted for by using a uniform effective oxygen concentration in the flow channel, equal to the average of inlet and exit concentrations. They argued that for air cathode, cathode activation loss was the most important source. But for pure O_2 cathode, the ohmic loss in the membrane constituted a major fraction of the loss. The model predictions were fitted to the measured polarization curves after ohmic iR correction (including the membrane and contact ohmic loss) indirectly determined via high-frequency voltage loss experiments, as shown in Figure 2-18.

In their model, the anode overpotential and the electronic loss within the catalyst layer and the gas diffuser was not considered. In the results and discussion section, the effect of cathode kinetic parameter, $a \cdot i_0^{ref}$, was investigated, which showed higher intrinsic activity of the catalysts shifted up the polarization curves. At a given constant loading, catalyst layers with more widely distributed thickness across the surface of the membrane were shown to yield higher currents at high polarization, whereas the overall Pt loading determined the performance at low polarization. Their model also demonstrated that the oxygen transport at high current densities was more determined by the mole fraction of oxygen in the gas mixture, instead of its partial pressure. This dependence arises from the opposite effects of pressurization of a gas mixture on the concentration and effective diffusion coefficient of a gas component. A Nitrogen blanket was shown to slow the oxygen mobility through the backing layer, based on an analysis using the Stefan-Maxwell equation. It should be noted that the liquid flow field through the

electrode was not investigated in this model, though the liquid water in the cathode was allowed to decrease the porosity at a steady-state. However, the possibility of dependence of oxygen reduction reaction rate on liquid water content at the cathode/membrane interface was discussed by the authors, which implied that the Tafel slope for ORR might need to be adjusted along with the change of the current density.

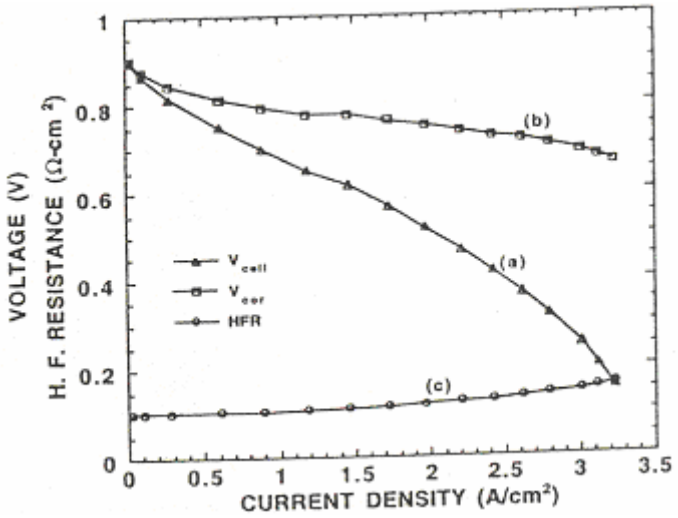

Figure 2-18. (a) Original polarization curve, (b) polarization curve after IR correction, (c) measured high-frequency resistance.[39]

In 1996, Nguyen proposed a gas distributor design for the PEMFCs, which was claimed to be able to improve the mass transport rates of the reactants from the flow channel to the inner catalyst layer, and also reduce the electrode flooding.[40] Along the gas channel, as the exiting reactant is fully humidified by the water vapor transported out from the cathode interface, there will be no driving force for the remove of excess water in the form of water vapor. The new design made the inlet and outlet flow channels dead-ended so that the reactant gases were forced to flow into the porous electrode, which converted the transport of the reactant/product gases to/from the catalyst layer from a diffusion mechanism to a convection mechanism (Figure 2-19). Also the shear forces helped remove most of the liquid water that was initially entrapped in the inner layer of the electrode. After comparing with the conventional flow channel design, the new pattern showed great improvement of cell performance and extended mass transport limited region, as well as higher power density peak. What's more, the new gas distributor design

allowed the use of liquid water injection system for anode humidification and simultaneous heat removal. The above improvement was found to be pronounced for both high and low current density with an air cathode, but only apparent at high current density for pure O_2 as the reactant.

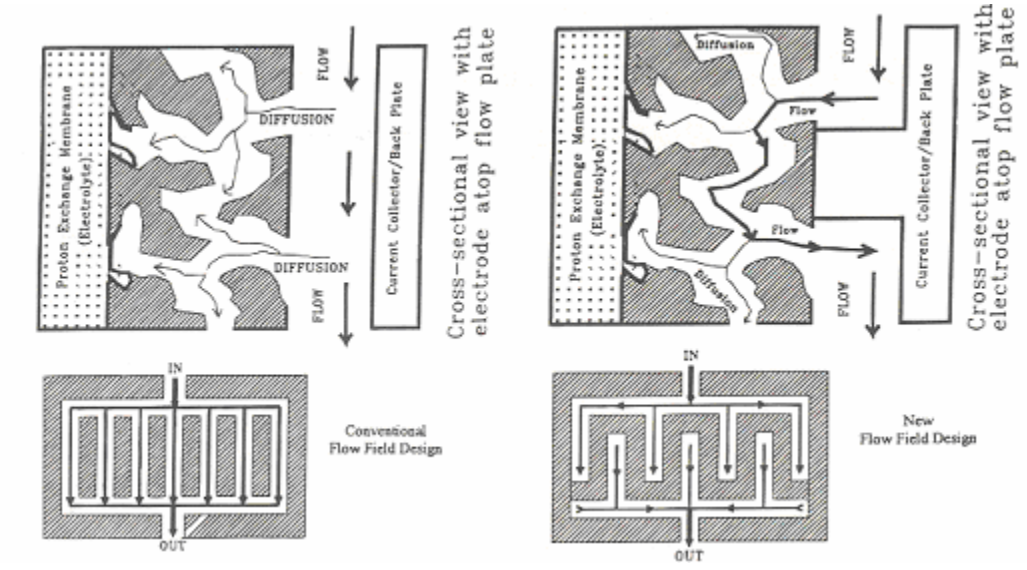

Figure 2-19. The gas distributor design proposed by Nguyen for the PEMFCs.[40]

Bevers et al. conducted a steady-state, one-dimensional, nonisothermal model of the cathode side only in 1997.[41] The descriptions of the material and energy balance as well as the transport of gases, water vapor and liquid water in the gas diffusion layer and the catalyst layer constituted the governing equations. One specific feature of this model was that the phase change of water in the cathode was included. Rapid water transport was assumed which implied that no liquid water flooding occurred at any time. The flow field of the bipolar plates was neglected in order to isolate the processes that were influenced by the cathode properties only. The temperature of the gas phase was considered equal to that of the solid phase at every point and no heat storage occurred in the gas species. The distributions of pore radii and tortuosity of the cathode were approximated by effective mean values while the thermal conductivity and heat capacity of the solid phase were assumed independent of the porosity. The model analysis showed that the usually assumed Tafel slope of -60 mV/decade could not be used to simulate a real system; hence the open circuit potential was employed as a fitting parameter to account for the unpredictable impurities in the catalyst, side reactions, differences in the effective active surface

and crossover of hydrogen and oxygen. If a different potential other than the measured OCV was used, it was necessary to use the term of apparent exchange current density to fit the model. It turned out that a satisfactory agreement between model predictions and experimental data could be achieved only by taking the Tafel slope as 800 mV/decade, which is much higher than the electrochemically determined value. These discrepancies indicated the inaccuracy of the model system or values of model parameters.

In 1997, K. Broka and P. Ekdunge modeled the PEM fuel cell cathode one-dimensionally and isothermally.[42] Their paper presented the comparison between the pseudo-homogenous film model and the agglomerate model for active catalyst layer. Two assumptions employed for both models were that the transport of H_2 and O_2 reactants to active sites occurred by diffusion through the gas pores and/or through the ionomer in dissolved form and any excess water in the cathode existed in liquid form. In pseudo-homogenous film model, the catalytic layer can be described as a macro-pseudo-homogenous film, consisting of four superimposed media, a diffusion, ionic, electrical conduction and catalytic medium. The kinetics expression for the oxygen reduction rate per unit volume was described by the simplified Bulter-Volmer equation. In the agglomerate model, the concentration gradient for oxygen was perpendicular to the potential gradient in the agglomerate, since the oxygen was diffusing from the gas pores into the agglomerate. The effect of the material transport limitation due to the oxygen diffusion in the agglomerates was simply characterized by an effectiveness factor $E = \tanh(mL)/mL$, where mL is Thiele's modulus, $mL = L \cdot (k/(c_{o_{O_2}} \cdot D_{eff}))^{0.5}$ and the rate constant k is calculated from the equation: $\frac{\partial i}{\partial x} = nF[\frac{1}{\delta/(aC^*_{O_2} D_{eff} + 1/kE}]$.

The SEM image in Figure 2-20 indicated that the agglomerate model gave a better representation of the reaction zone than the pseudo-homogenous model. The thickness of the active layer and the size of the agglomerate were estimated from the SEM micrograph to be several micrometers. For the same effective permeability and thickness, the agglomerate model resulted in lower overvoltage, a more even distribution of variables such as O_2 concentration, current density and potential, and a higher limiting current density because the reactants could penetrate into the catalyst layers.

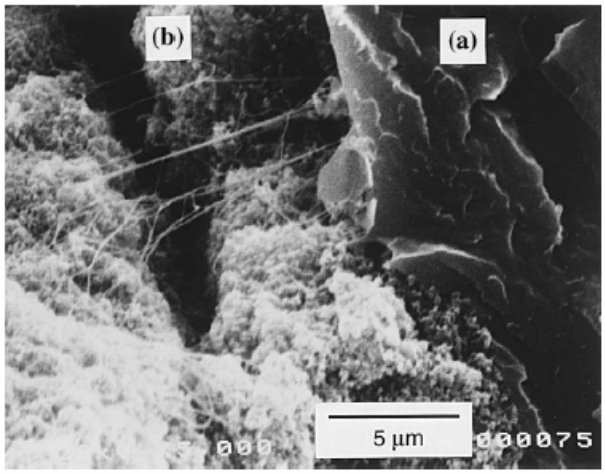

Figure 2-20. The SEM image of the reaction zone by Broka and Ekdung, (a) Nafion 117 membrane, (b) impregnated catalyst layer.[42]

Most of the models so far concerned the membrane according to its global conductivity and permeability as a function of water content. In 1998, Eikerling et al. published a paper that described the water and ionic conducting phenomena occurring within the membrane in great detail, including the capillary action and electro-osmotic drag.[43] A discussion of the membrane properties such as the pore-size distribution function and the electro-osmotic drag coefficient was also given. This model was used to predict the water content profiles and the voltage-current plot for medium current densities, on the basis of which the existence of a critical current was proposed. The critical current or oxygen depletion could lead to a dramatic drop in the water content at the membrane close to the anode side. It was concluded that increasing the proportion of microscopic pores in the membrane could induce an increase of the membrane conductivity, but a decrease of the effective Darcy's coefficient. The optimization of the porous structure was considered very important to achieve good performance by the membrane.

In 1999, Marr and Li developed a steady-state, one-dimensional, isothermal model focusing on the electrochemical reaction and mass transport of the catalyst layer.[44] This model aimed at the catalyst layer performance and its composition optimization under various conditions. The distributions of current density, oxygen concentration and the location of the zero oxygen

concentration fronts, as well as the change of cell performance at different catalyst loading and void fraction were given in the result section. It was found that the electrochemical reactions occur in a thin layer within a few micrometers thick, indicating ineffective catalyst utilization for the present catalyst design, especially at high current densities. The authors also reported the optimal void fraction for the catalyst layer might be around 60%.

Baschuk and Li presented a steady-state one-dimensional isothermal model in 2000, with the components of MEA modeled as equivalent electrical resistors.[45] The degree of water flooding in the gas diffusion electrodes was included as a modeling parameter, which was adjusted to match the experimental polarization curves, i.e. the degree of flooding was determined by a trial and error method or used as a fitting parameter. In their model, the catalyst layer was assumed to be uniformly distributed and the Knudsen effect was neglected. The membrane was taken as fully hydrated. The oxygen in the gas channel was assumed to diffuse to the surface of the electrode first, and then continue diffusing through the electrode to the catalyst reactive surface. The experimental data measured by Kim et al. and Voss et al. were chosen to fit the model predictions at different cell temperature and pressure using air or pure oxygen as the reactant. It was shown that the resultant flooding schedules using air or oxygen were dissimilar with each other. Increasing the cell pressure could increase significantly the extent of water flooding in the electrode. Increasing the cell temperature made the initiation of the electrode flooding occur at a higher current density.

Shortly after that model, Rowe and Li developed a one-dimensional, nonisothermal model in 2000 involving variable membrane hydration and phase change of water with unsaturated reactant gas streams.[46] The influence of cell temperature, gas steam humidity, pressure and composition on cell performance was investigated using this model. The viscous, Soret, Dufour, gravity and radiation effects as well as pressure change in the electrode were ignored. Small temperature variations of the cell were assumed so the material properties were evaluated at the average cell temperatures. The cathode catalyst was assumed to be full humidified but anode catalyst humidification depended on the water vapor activity through the adsorption isotherm of the Nafion membrane. The water activity was expressed with the product of water vapor mole fraction with the ratio of water vapor partial pressure to saturation pressure. The catalysts at both

sides were taken as uniformly distributed. The membrane pressure differential between the anode and cathode was assumed to vary linearly with the thickness. No adjustment of $a \cdot i_0^{ref}$ was executed during model solving process. The plots in the results showed that larger temperature peak occurred within the cell operated at lower temperatures. Operating on reforming fuels resulted in a decrease in cell performance because CO_2 decreased H_2 mole fraction and limited the diffusion coefficient of water vapor at the anode, and thus reduced the membrane hydration. High gas permeability of the electrode could have a large positive impact on the cell performance at high current densities. It turned out the anode and cathode temperature was almost linear but the membrane temperature was highly nonlinear which meant the predominant heat source was joule heating, neither heat conduction nor phase change (see Figure 2-21). Nevertheless, at low current densities, the effect of water condensation in the cell may become the most important factor for temperature distribution.

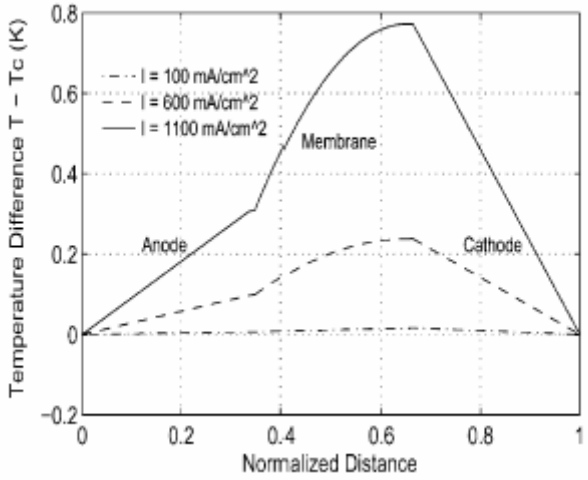

Figure 2-21. Temperature profile in a PEMFC predicted by the model of Rowe and Li.[46]

In 2002, Djilali and Lu proposed a steady-state, one-dimensional, nonisothermal and nonisobaric model, which was formulated for a complete fuel cell with ternary fuel and oxidant gases.[47] The assumptions for this model were: 1. The fluid and solid phase shared a homogenous local temperature, 2. The diffusion of dissolved gases in the membrane and the effect of dissolved gases on water balance are neglected, 3. The concentration of the hydrogen protons can be

assumed constant throughout the reaction active catalyst layer, 4. The catalyst layer was taken as an ultrathin interface with only the source and sink terms associated with it, 5. Water and gas transport were considered to take place in separate pores with no interaction, which is the weakest assumption used in the model. However, for the multi-component gas through the electrode, the effect of gas pressure and Soret effect was considered, hence a more complex Stefan-Maxwell equation was employed. The convection of the liquid water in the electrode was accounted for along with the heat generation and transfer in the PEMFC. Non-uniform distribution of gas pressure in the porous electrode and micro-hydrodynamics in very small pores (Knudsen diffusion) were taken into account due to the range of the electrode permeability. The model equation system was solved by use of a staggered-grid finite volume method. To exhibit the effect of isobaric and isothermal conditions, Djilali and Lu compared their results with that of Bernardi and Verburgge. Their model results exhibited a big temperature gradient in the fuel cell: the higher the current density, the greater the temperature gradient. The highest temperature of the fuel cell occurred at the membrane/cathode interface, and the temperature profile in each component was shown to be linear (Figure 2-22).

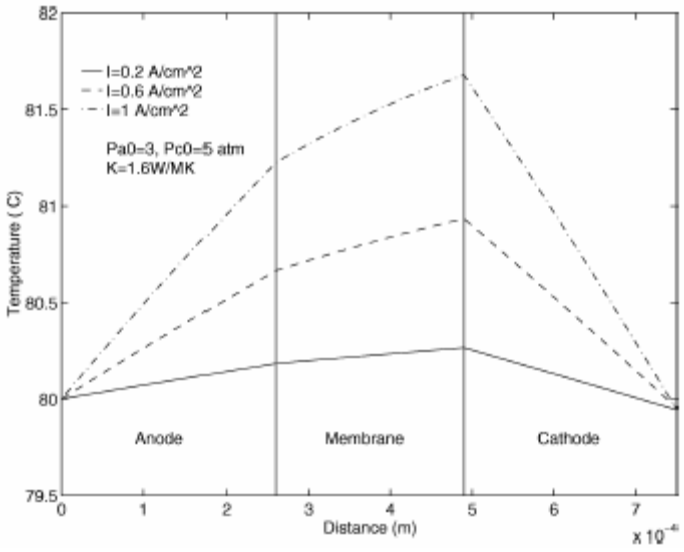

Figure 2-22. Temperature profile in a PEMFC predicted by the model of Djilali and Lu.[47]

It was found by Djilali and Lu that non-uniform distribution of pressure and temperature had a large impact on the model predictions of the liquid and water fluxes which indicated that the

water management requirements preventing membrane dehydration and cathode flooding should be much more conservative than models assuming isothermal conditions. Three regimes of current density i.e. $i < 0.23\ \mathrm{A/cm^2}$, $0.23 < i < 0.38\ \mathrm{A/cm^2}$, $i > 0.38\ \mathrm{A/cm^2}$ were defined, corresponding to the variations of water flux at the anode-channel and cathode-channel boundaries, as shown in Figure 2-23. It should be mentioned that the membrane dehydration has not been accounted for in this model, which will be done in the future work.

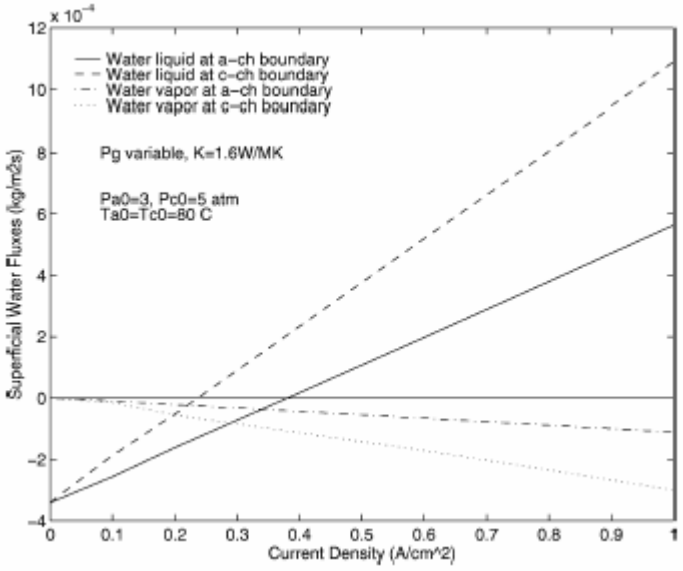

Figure 2-23. Variations of water flux at the anode-channel and cathode-channel boundaries that correspond to three regimes of current density.[47]

2.7.5.2 Two-Dimensional Models

Fuller and Newman proposed the first steady-state, quasi two-dimensional, nonisothermal model of MEA in 1993. The model was actually solved one-dimensionally, but the solutions were integrated along the channel length.[48] The MEA was set to operate on air and ternary H_2 mixture reformed from methanol. In this model, a macroscopic approach was applied with the reaction zone treated as the superimposed continua consisting of solid, gas and membrane. The analysis was taken in three areas, the first of which was constant temperature study of a unit cross section of the fuel cell; the second of which was the water management at constant temperature with cocurrent flow of air and fuel; the third of which was the combined material and energy balance.

Transport in the polymer electrolyte was described with concentrated solution theory, with a fundamental equation $\vec{d}_i = \sum_{j \neq i}^{n} K_{ij}(\vec{v}_j - \vec{v}_i)$, where $\vec{d}_i$ is the driving force for transport, K_{ij}'s are the frictional coefficients. In the results section, the water concentration, net water flux in the membrane and mole fraction of gas species in the channel as well as the local current density distribution under isothermal conditions were presented. The water concentration and current density as a function of hydrogen utilization were also given in a nonisothermal case. The importance of water and thermal management for PEMFCs to achieve high efficiency was emphasized. The rate of heat removal was shown to be a critical parameter in the operation of the PEMFCs.

In the same year, Nguyen and White developed a steady-state, two-dimensional, nonisothermal model by extending their one-dimensional model to include the convective water transport across the membrane by a pressure gradient and the heat removal by natural convection and coflow and counterflow heat exchangers.[49] The phase change of water was accounted for, though an ultrathin gas diffusion layer was assumed and the volume of liquid phase was neglected. The other assumptions used in this model included: 1. The temperature of the solid phase in bipolar plates, electrodes and membranes was uniform and constant. 2. In the gas channels, plug flow prevailed and no pressure drop occurred along the gas channel. 3. Water entering and leaving the gas channel, electrode and membrane was in the form of vapor only. 4. Heat conduction in the gas phase was neglected. 5. No voltage drop occurred along the gas channels. In the end the model was used to justify the different humidification designs for PEMFCs after distributions of water, temperature, oxygen partial pressure and current density along the gas channel were presented. It was concluded when using air in the cathode, the cathode gas stream must be humidified to prevent membrane dehydration.

In a typical fuel cell stack, the individual cells are connected in series and the reactant gases are supplied in parallel through a manifold (Figure 2-24). Thus, the operation of a fuel cell stack depends on the electrochemical performance of the MEA, gas flow across the flow field of a single cell, gas manifolding and stack design. In 1997, Thirumalai & White integrated above single-cell model with the model of flow field in the gas manifold to predict the operational

characteristics of a PEMFC stack.[50] The general momentum, mechanical energy and mass balance equations of the stack were given, though solving the Navier-Stokes equation throughout 50 cells numerically was considered impractical. Instead, a sensitivity analysis of the cell potential was performed for pure O_2 and air while keeping the current density drawn from the stack constant. The analysis showed that nonuniformity in single-cell reactant gas flow would result in a decrease in the efficiency of the stack. To eliminate this effect, the authors proposed the idea of trading off between the flow resistance of the single cell and that of the gas manifold through specified manifold dimensions. The effect of the nonuniform temperature distribution across the cells on stack performance was not considered in their model.

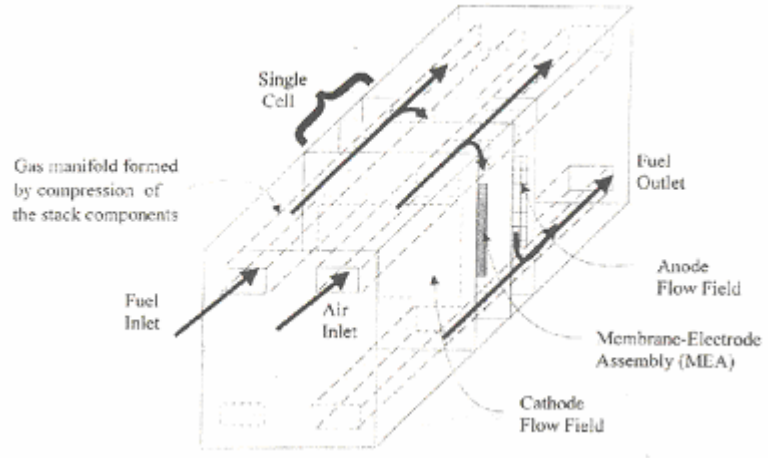

Figure 2-24. Schematic of a PEMFC stack with Z-manifold design.[50]

Yi and Nguyen then conducted a steady-state, two-dimensional, along-the-channel nonisothermal model in 1998.[51] Again, similar to their 1993 two-dimensional model, the convective water transport across the membrane and heat removal by natural convection and heat exchangers were not involved. Most of the old assumptions were still adopted in their new model. The main improvements were that the temperature gradient along the gas channel in the solid phase and the effect of reaction gas dilution by water vapor were taken into consideration. However, no temperature drop was assumed across the cell. In the result section, the net water transport by diffusion and by eletro-osmotic effect was separated and plotted. The water, temperature, and current profiles along the flow channels were explored with comparisons to

their previous model in which the temperature in the solid phase was taken as a constant. Different heat removal and humidification strategies for PEMFCs were examined for different cell bulk temperature, liquid injection, and convective flow caused by pressure differential in the membrane and heat exchangers.

One year later, Yi and Nguyen presented a steady-state, two-dimensional, isothermal model for multicomponent transport in gas diffusion layer with an interdigitated gas distributor.[52] The model described a two-dimensional flow pattern and predicted the values of current density as a function of operating conditions and design parameters. The porous electrode layer was treated as a homogenous phase with uniform morphological properties such that the effective diffusion coefficient was invariant of position. It was assumed that water in the electrode existed as vapor only. The permeabilities and viscosities were assumed constant in the model without any pressure dependence because the pressure change was negligible in the range studied and most of pressure drop was located along the gas channels. The continuity equation and Darcy's law along with specified boundary conditions for the case of interdigitated gas distributor were employed. Once the partial pressures of oxygen along the reaction interface were known, a finite difference algorithm was used to solve the model. Only current densities where the water vapor pressure was lower than the saturated vapor pressure were studied in order not to violate the assumptions. Results showed that with the forced flow-through condition created by the interdigitated gas distributor, the electrode could be reduced to a much thinner combined catalyst and boundary layer, which is highly porous to keep the pressure drop low. The results also showed the average current density generated at the cathode increased with higher gas flow-through rates, thinner electrode (the gas shortcut and bypassing effect was less severe) and narrower shoulder width. Experimentally, PEMFCs with interdigitated gas distributor exhibited very stable performance at very low stoichiometric flow rates and no performance hysteresis at a given current density or potential was observed. It was concluded that the diffusion was still very important for reactant gas transport to the cathode/membrane interface even with the interdigitated gas distributor and the higher gas flow rate could improve the performance only when this diffusion layer become thinner.

He, Yi and Nguyen again developed a detailed steady-state, two-dimensional, two phase isothermal model for interdigitated flow field design in 2000.[53] Their previous models were extended to include the two phases in the electrode and the effect of liquid water transport. The aim was to investigate the effect of various electrode and flow field design parameters on the performance of PEMFCs with interdigitated flow pattern. It was assumed that water was generated as liquid because the PEMFCs are running at a temperature lower than 100^{o}C. In this study, the electrode was treated as a homogenous porous media with uniform porosity, tortuosity, and permeability. The catalyst layer was treated an ultrathin interface within which the transport of species was neglected. It was shown that high differential pressure between inlet and outlet channels could yield higher electrode performance due to the higher rate of oxygen transport and liquid water removal. The electrode thickness needed to be optimized between the thin electrode with reduced gas-flow rate and thick electrode with thicker diffusion layers. The distributions of water vapor, oxygen mole fraction, liquid water and current density in both of the electrode width and height directions were analyzed and plotted. The effects of differential pressure between the inlet and outlet, electrode thickness and shoulder/channel width ratio were investigated based on the model predictions.

Gurau, Liu and Kakac presented the first steady-state, two-dimensional, nonisothermal model of a complete fuel cell, employing the computational fluid dynamics (CFD) techniques in 1998.[54] The authors applied the concept of coupled gas channel/gas diffuser/catalyst layer domain, which enabled them to use the same numerical method throughout. Thus the need to prescribe or approximate boundary conditions at the interfaces was eliminated. Although objects of analysis were different along each element, three coupled domains, which were gas channel-gas diffuser coupled domain for gas mixture, PEM-gas diffuser-catalyst layer for liquid water and catalyst layer-PEM domain for protons were utilized to formulate the continuity, momentum and species conservation equations. This model assumed no interactions between liquid water and water vapor even though the values of the general diffusion coefficients did account for this effect. The materials in gas diffusers, membrane and catalyst layers were taken as homogenous. In spite that the authors realized the reactants dissolve into water before they are subjected to the electrochemical reactions, this phenomenon was ignored in their model. The heat by viscous dissipation and the dispersion in porous media were also disregarded. In the results section, a

parametric study was performed for variables that could be controlled in real fuel cell applications such as O_2 and H_2 mole fraction. The influence of gas diffuser porosity, the inlet air velocity and temperature on cell performance was investigated. Like many other models, the direction of net water flux in the membrane was switched as a function of current densities. An important conclusion of this model was that the computed oxygen mole fraction along the gas channel-gas diffuser interface and the current density along the membrane-catalyst layer interface did not have linear distributions, as usually assumed in other work.

In 2001, Wang, Wang and Chen published a steady-state, two-dimensional, two-phase isothermal model for the cathode side of a PEMFC where the catalyst layer was treated as ultrathin interface.[55] The single and two-phase transport regimes were first defined based on the multiphase mixture model in porous media, which was also proposed by Wang and Chen to account for liquid phase transport by capillary action, phase change and multicomponent gas transport. Three diffusion mechanisms were considered in this model: mass diffusion through liquid and gas phase, and capillary diffusion within the two-phase zone. The unique feature of multiphase mixture model is that it does not need to track phase interfaces separating single from two-phase regions. It was assumed that when current density was low, the water in the cathode was first present as vapor. As the current density increased, the water vapor reached saturation and gradually condensed into liquid water (see Figure 2-25). This marked the end of single-phase regime; consequently the current density was the threshold current density. The situation where a single-phase region and two-phase region coexist in the cathode was also modeled. The capillary force was found to be the predominant mechanism for water transport inside the two-phase zone. The dimensionless mass Sherwood number was employed to estimate the mass transfer coefficient at the cathode/channel interface. In the results section, the water vapor, liquid water, oxygen concentration contours and the current density distribution were provided along with the two-phase mixture velocity field. The advantage of this model was that it not only provided a unified formulation for both single-phase and two-phase calculation at low and high current densities, but ensured the smooth transition from the single to two-phase region automatically. It has been shown that the threshold current density for liquid water to appear in gas channel was about 1.47 A/cm^2.

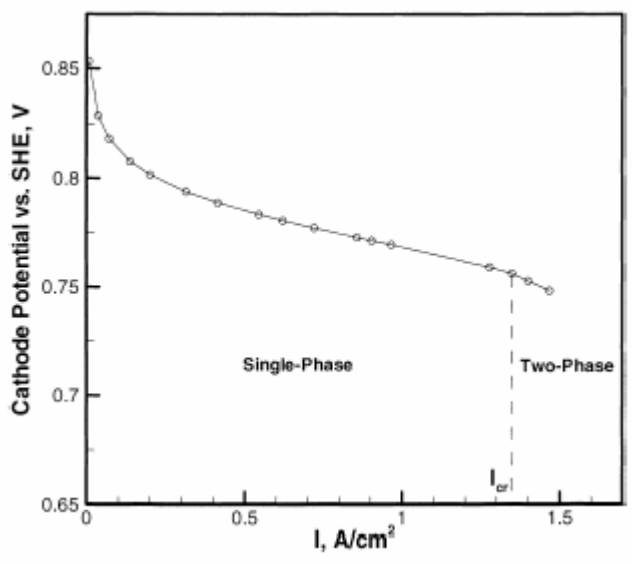

Figure 2-25. The transition from single-phase to two-phase in the cathode assuming dry inlet gases.[55]

Ge and Yi proposed a steady-state, two-dimensional, isothermal mathematical model for a PEMFC in different flow modes in 2002.[56] In their paper, basic material balance equations were employed with the assumption of plug flow and no pressure drop along the channel. The effect of liquid water on the gas transport in the cathode was considered simply by changing the values of effective porosity. No interactions between the liquid and vapor phase were assumed. The contact resistance was taken into account by assigning a constant value to it and the cathode liquid water saturation was included to calculate the cathode overpotential via modified Tafel equation. The mole flow rates for reactant gases were calculated and integrated along the electrode length. The fractions of liquid product water leaving the anode side were measured. The authors also carried out the parametric study for the relative humidity of reactant gases, imposed pressure differential, cell temperature and membrane thickness. It was concluded that only the counterflow mode could help the entering dry reactant gases get hydrated by the exiting gas to minimize the need of humidification. However, there are two places in the paper need to be discussed. First, the authors attributed the decrease of local current density along the flow channel to the existence of liquid water in the coflow mode, which might not be the case since reactant gas could be diluted along the channel by consumption as well as addition of water vapor. Secondly, the enhancement of cell performance at a higher temperature was explained as

the evaporation of liquid water from the electrode, which might actually be related to the effect of temperature on the (electrochemical) reaction rate.

In 2003, another single domain steady-state two-dimensional nonisothermal model was presented by Siegel et al.[31] In comparison to the macro-homogenous catalyst layer approach, an agglomerate geometry was employed to describe the transport phenomena occurring in the catalyst layer. The authors assumed that the reactant gases flow through the macro-pores of the catalyst layer, then dissolve and diffuse into the agglomerate to the reaction site, which implied water existed in both dissolved form and gaseous form. The mass and momentum conservation equations were given in vector form, especially the mass transfer of water and reactants between the gas phase and the dissolved phase was accounted for by source terms. The catalyst layer structure had been examined by the SEM and TEM micrograph to verify the agglomerate model and estimate the agglomerate size, the thickness of catalyst layer and the void fraction. One of the TEM images was shown in Figure 2-26. In this model, the convective term in the membrane was neglected due to the small pressure differential of the anode and cathode gas channel. The oxygen reduction reaction was assumed to produce water in the form of liquid and the liquid water could vaporize instantly. A constitutive relation that connected the membrane water content with the dissolved water concentration and accounted for the membrane swelling was applied. In accordance with the hypothesis, the results showed that the fuel cell performance was highly dependent on the catalyst structure, specifically the relative gas pore volume fraction and the membrane content within the active layer as well as the geometry of the individual agglomerate. The optimal catalyst layer void fraction, catalyst layer thickness, and the size of the catalyst agglomerate were then given. The oxygen concentration across the catalyst layer and the current density versus the agglomerate characteristic length was also examined. The authors are currently working to extend this model to three-dimensional and include liquid water transport in the cathode.

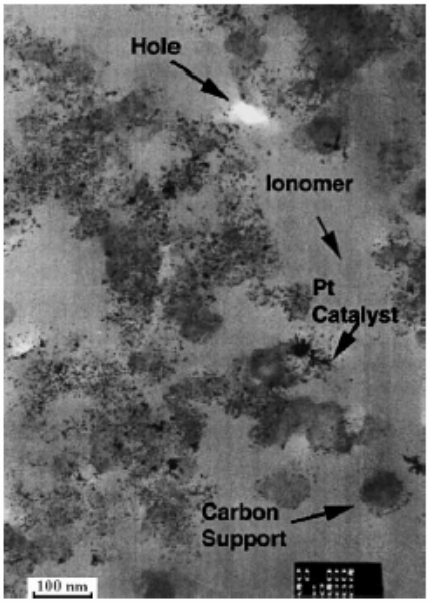

Figure 2-26. TEM image of the agglomerate by Siegel, Ellis and Nelson et al.[31]

2.7.5.3 Three-Dimensional Models

The first steady-state three-dimensional isothermal model for PEMFCs was proposed by Dutta et al. in 2000.[57] A control volume method was used to model the cell in two dimensions on the membrane and one dimension along the gas channel. The computational domain shown in Figure 2-27 included the anode and cathode gas channel, diffusion layer and MEA. Though this model accounted for a partially dehydrated membrane, the volume of liquid water was neglected and only vapor phase of water was assumed in the gas channels. The pressure driven flow in the membrane was not considered. Commercial software (Fluent 4.48) was modified to solve the coupled equations by incorporating the electrochemical reactions via addition of the source terms. In the results, the effect of membrane thickness and cell voltage on local width-averaged current density profiles and velocity as well as mixture density contours were provided for several cases in comparison with the predictions of Nguyen and Yi and Fuller and Newman's model. It was illustrated that the presence of diffusion layers adjacent to both sides of MEA could help create a larger reaction area and hence result in higher current densities. However, the diffusion layer behaved as the resistance to convection flow at the same time. In the diffusion

layer, the reactants were transported by convective and diffusion mechanisms, neither of which should be ignored even for low porosity of the layer.

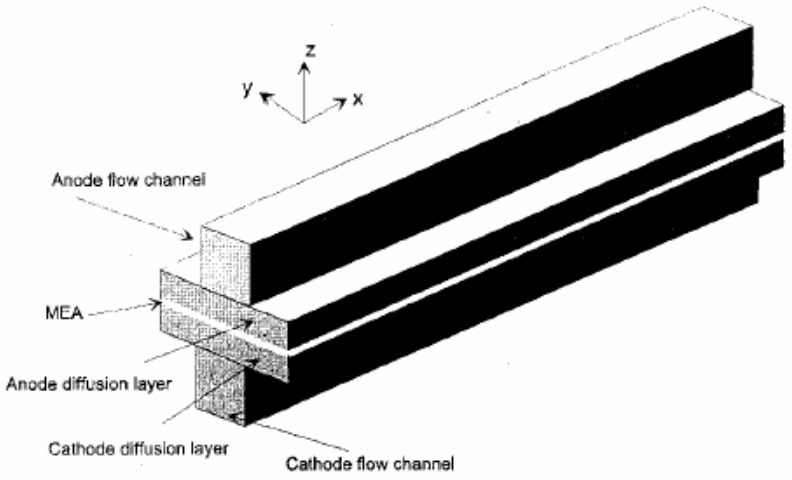

Figure 2-27. The computational domain used in Dutta et al.'s model.[57]

In 2002, Berning and Djilali presented a steady-state, three-dimensional, nonisothermal model. The model claimed to account for all of the major transport phenomena except phase change, including the multiphase, multicomponent and multidimensional flow, heat and mass transfer with electrochemical reactions that occur in porous media or gas channel.[58] Hence the governing equations were based on the full mass and momentum, species and energy conservation equations in a vector form. However, the membrane was assumed fully humidified so that the ion conductivity was constant and no back diffusion term was applicable. Only one phase, (i.e. the gaseous phase) was considered in the gas channel. In addition, the assumption that the water in the pores of the diffusion layer was separated from the gas in the layers was a weak statement. The heat transfer inside the membrane was accomplished by conduction only. The model domains comprised a main domain and three subdomains used for solving heat flux, liquid water through the MEA, and electrical potential in the membrane respectively. Three-dimensional reactant gas and temperature distribution as well as the net flux of water through the membrane were given as the model results. The effect of land area was shown to be pronounced when the current density is high. Since uniform current density is desirable in a PEMFC, the authors

proposed to solve this predicted nonuniformity of current density by design of a non-homogenous catalyst layer or GDL.

Hertwig, Martens and Karwoth also addressed a steady-state, pseudo-three-dimensional, isothermal model in 2002.[59] One-dimensional calculations were conducted for the MEA but a two-dimensional model was utilized for the gas channel, which altogether resulted in a pseudo-three-dimensional modeling. In their paper, a representative single cell element (SCE) was adopted. The different channel structures were compared in terms of the flow field. The modeling equations included the external balances with the single cell that described the reactant gas feeding, two-phase species transport in the anode and cathode channels and the material flows between the anode and cathode based on the water vapor flow across the membrane region. The simulation of the distributions of the current densities and concentrations were waived in the SCE. Only the superior distributions along the length of the channel were considered. Empirical approaches were utilized to calculate the effective electrode kinetics so the diffusion inhibitions in the gas diffusion layer were neglected. The pressure loss in the main distribution channels was neglected while the whole pressure loss was based on the Bernoulli equation for channel flow. A three-fold staggered iterative solution technique was developed to solve this single cell model. The results provided the distributions of current density, water vapor in the gas channel and membrane water concentration as a function of the cell width and height for Nafion1 and Gore1 membranes at different cell potentials. It was shown that Gore1 membranes have better performances than Nafion 1 membranes.

Recently, Natarajan and Nguyen (2003) developed a steady-state, pseudo-three-dimensional, isothermal model.[60] Their previous two-dimensional models were expanded to account for the dimension along the gas channels, which was proven to be critical to obtain an accurate prediction of the cathode performance. The length of channel was divided into a series of control volume that has a gas diffuser and a channel volume associated with it. All of the gradients at the boundaries of the control volume were forced to be zero. The model took the gas composition change along the channel into consideration. Convection was only considered along the gas channel and diffusion was the only mechanism in the diffusion layer. This model did not account for the momentum effects in the channel and hence did not explicitly solve for the gas phase

species concentration and liquid water amount. Once the gas stream in the gas channel was saturated, the water vapor boundary condition was forced to be at the saturation pressure and the liquid water saturation was forced to be 0.1. Hence the model could not capture the severity of the flooding beyond the boundary and the model predictions were qualitative once liquid water was present in the channel. The authors admitted adjusting the exchange current density and the rate of liquid water removal to fit the experimental data. The variation of the current density along the channel length was found to be largely dependent on the oxygen concentration changes due to the dilution effect. Operating conditions like higher temperature, higher stoichiometric rate and lower cathode inlet humidity were shown to result in better water removal rate and higher current density. Three-dimensional effect of liquid water was seen more severe over the shoulder, which led to a more nonuniform distribution of the current density.

2.7.5.4 Others

2.7.5.4.1 Gas Distributor Models

In 2000, Hontanon et al. gave a steady-state, three-dimensional, isothermal model of gas flow in the bipolar plate and anode in order to optimize the flow field.[61] The balance equations from fluid mechanics in the vector form were adopted for the compressible flow in the fuel side. Two types of gas distributors were compared using the model, one of which was the grooved plate, the other of which was a porous material. The results showed that H_2 consumption in the anode increased with the decrease of the channel width and the H_2 depletion in the anode increased with the increase of the rib width. Therefore decreasing the size of both ribs and channels was advantageous for the performance. When comparing the grooved plate with the porous media, a concept of equivalent permeability was introduced by the authors and the simulation showed that porous medial are more advantageous than grooved plate with respect to the reactant gas utilization.

Kumar and Reddy provided a steady-state three-dimensional isothermal model of gas channel in 2003.[62] The flow in gas channel was assumed as laminar based on the Reynolds number calculation. The permeability of the electrode was assumed isotropic and the volume of the by-

product liquid water was neglected. The continuity equation and Navier-Stokes equation in rectangular coordinate system were used. The model equations were solved using CFD software (Fluent 6.0). The aim of this study was to provide a tool to optimize the channel dimensions and shape by looking at the hydrogen consumption condition at the anode. A single-path, serpentine flow field was studied. The results revealed that the triangular and hemispherical shaped cross-section of the channel resulted in a higher hydrogen consumption and then a higher fuel utilization. For the base case, high hydrogen consumption (~80%) was achieved when the channel width, land width and channel width was close to 1.5, 0.5 and 1.5 mm respectively.

2.7.5.4.2 Semi-Empirical Models

In 1994, a steady-state electrochemical model (SSEM) was developed by Amphlett et al. to model the performance of a Ballard Mark V 35-cell 5-KW PEMFC stack.[63] In general, there is no need for assumptions for the empirical modeling, though the applied parameters may have ambiguous meanings. On the other side, the mechanistic models are usually very intricate, coupled complex models, which are very difficult to solve, and hence need quite a few simplifications. In spite that the empirical models are only accurate over a narrow operating range, they can be helpful in doing some simple trend analysis. A semi-empirical approach seems more appealing in some cases. In this model, the anode and cathode gases were assumed saturated with water vapor in a humidifier. The dissolved oxygen was assumed diffusing to the reaction sites through a water film that covered the catalyst layer. This assumption may not be very appropriate, since it is commonly accepted that the dissolved oxygen diffuses through the polymer phase to react with hydrogen ions and electrons. But this assumption will not affect the form of the semi-empirical equations to a large extent. After analyzing the experimental data of a Ballard V PEMFC stack by linear regression, the values of the semi-empirical model parameters were obtained as: $\zeta_1 = -0.694$, $\zeta_2 = 4.34\times10^{-3}$, $\zeta_3 = -1.96\times10^{-4}$, $\zeta_4 = 1.80\times10^{-5}$, $\zeta_5 = 3.30$, $\zeta_6 = -7.55\times10^{-3}$, $\zeta_7 = 1.10\times10^{-3}$.

Kim, Lee and Srinivasan also presented a semi-empirical model of PEMFCs in 1998.[64] A semi-empirical equation $E = E_0 - b\log i - Ri - m\exp(ni)$ was shown to fit the experimental data of

cell potential versus current density reasonably well, where E is the cell potential, i is the current density, b is the Tafel slope and R represent the resistance, predominantly ohmic and to a small extent, the charge transfer resistance of the anode side. Nonlinear parameter estimation software was utilized to determine the values of the parameters with correlation coefficients in excess of 0.99. The effects of different values of m and n were investigated in order to interpret their physiochemical meanings. It was proposed that m was responsible for the increase in slope of the linear region of E versus i plot whereas n had a dominant contribution to the rapid fall of E with i at high current density region.

In 2000, a generalized steady-state electrochemical (GSSEM) model with only operating variables as input was established by Mann et al. based on the previously proposed steady-state electrochemical model (SSEM) developed for Ballard Mark IV and Mark V system.[65] Only isothermal conditions and no excess liquid water in the electrode were considered in this model. The proton and water concentration were taken as constants. The current densities were set low and hence no mass transport limitations were evaluated. However, this model possessed both mechanistic and empirical features by generalizing the terms in SSEM and introducing cell dimensions and characteristics along with the extension of current densities. Most of the coefficients in the model had a theoretical meaning except for the ohmic overpotential that was experimentally determined. During the modeling, the anode and cathode activation overpotentials were combined as the total activation overpotential which was expressed by a semi-empirical equation with four coefficients related to the free energy of activation and the reactant concentrations. The equation was $\eta_{act} = \xi_1 + \xi_2 T + \xi_3 T \ln c^*_{O_2} + \xi_4 T \ln i$. The ohmic overpotential was regarded to be composed of electrical resistance by current collector and electrode as well as the proton conductivity. It was worth mentioning that a term to account for the membrane aging was added to the equation. The model predictions were shown to reach a good agreement with the experimental data. The values for coefficients in the GSSEM model were proposed as: $\xi_1 = -0.948(\pm 0.004)$, $\xi_2 = 0.00286 + 0.0002 \ln A + (4.3 \times 10^{-5}) \ln c^*_{H_2}$, $\xi_3 = (7.6 \pm 0.2) \times 10^{-5}$ and $\xi_4 = -(1.93 \pm 0.05) \times 10^{-4}$.

2.7.6 Review of Transient Models

There are several papers that have modeled the performance of PEMFCs in a transient state, as reviewed below.

In 1998 the dynamic modeling and simulation of a PEMFC was proposed by Wohr, Bolwin and Schnurnberger et al. with separate modules for each component.[66] The modules were coupled together to give a complete model which took the exothermic heat released by the cathodic reaction into account and considered temperature as one of the primary variables. The "Dusty-gas model", combining the Stefan-Maxwell equation and Knudsen diffusion with convective transport driven by a pressure gradient described the gas transport within the pores. Transport of the liquid water was characterized by surface diffusion and capillary action. The temperature profile in a PEMFC stack with 2, 3, and 4 cells were compared (see Figure 2-28 for temperature profile of a 4-cell stack) by assuming that the heat flow was only in the direction perpendicular to the membrane. The influence of model parameters such as thickness and porosity of the diffusion layer and the structure of the catalytic layer were illustrated. It was shown that the current and humidity distributions in the membranes of the cells within the stack had different shapes corresponding to the imposed flow field. Finally, the model results suggested the use of cooling plate as well as increase of the humidifier temperature and the fundamental diffusion coefficients. It seemed like this model was not solved and analyzed dynamically though the differential terms with respect to time was included in the governing equations.

Um, Wang and Chen published a transient, two-dimensional, isothermal model accounting for the electrochemical kinetics, current and concentration distribution, hydrodynamics and multicomponent transport in 2000.[67] This model was solved using a finite-volume based CFD technique. The hydrogen dilution effect was explored, which predicted little effect when current density was low but pronounced hydrogen depletion effect when current density was high. The transient behavior of PEMFCs was investigated by changing the cell potential, while the reacting time of current density was shown to be in the order of several seconds. The weakness of this model was that only the situation of one-phase transport in the electrode and cell current density smaller than 0.6 was examined. The cell was assumed to generate water vapor initially and then the vapor is condensed into liquid water. Average current density was calculated by integration

along the *y* direction. This paper also employed the single domain approach which assumed large source terms over specific subdomains and treated the jump condition at boundaries by standard interfacial resistance technique.

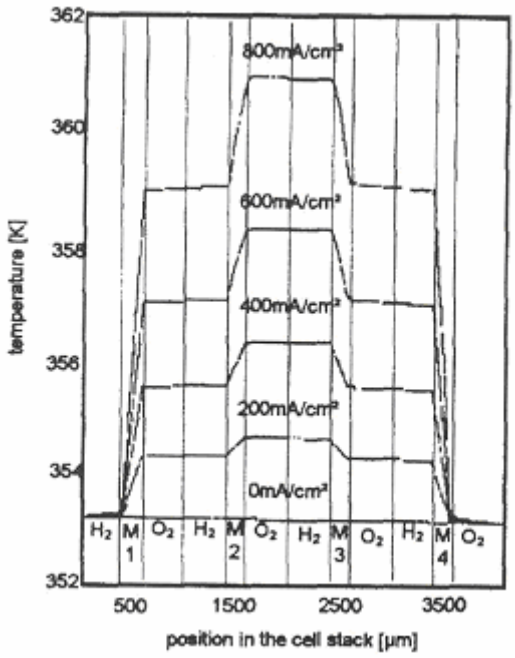

Figure 2-28. The predicted temperature profiles for a 4-cell PEMFC stack.[66]

S. Yerramalla et al. addressed the dynamic performance of a PEMFC in 2003.[68] Almost all of the modeling work in the literature have neglected the effects of inverter load in order to achieve simplicity. This research employed the electrical engineering approach, which applied the simulation block diagram to analyze the fuel cell system. In their view, "one-dimensional" model is that the fuel input is the only variable through the fuel cell and the inverter load is neglected. A "three-dimensional" approach was defined as three variables being the input: fuel supply, air supply and inverter load current. The stack voltage was shown to follow the inverter load in the form of a ripple, as shown in Figure 2-29. In addition, the step response of the stack and the cell utilization (polarization) were predicted using the linear and nonlinear model developed in this paper. The objective of this research was to design the damping controller for the PEMFC system operating as a distributed resource in a power system. The results indicated that the linear model stabilized its voltage faster than nonlinear model. The rapid response of the voltage to the

step change in the fuel cell load was due to the nature of the PEMFC, i.e. the electrochemical reactions are involved to generate electricity. It was also found that the output voltage was not smooth, which was attributed to the internal leakage currents between the individual cells.

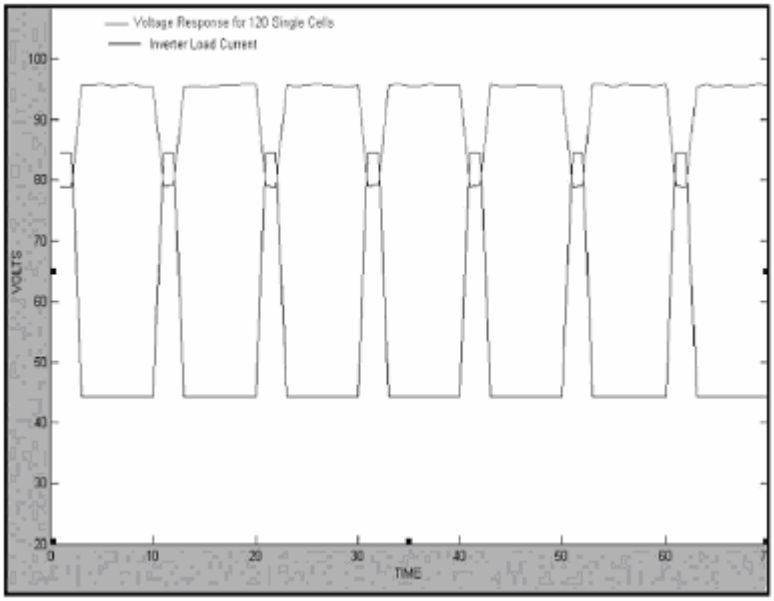

Figure 2-29. Voltage output of a PEMFC stack system containing 120 cells.[68]

2.7.7 Performance Model Summary

Mathematical modeling can function as a tool to optimize the design and performance of PEMFCs, by means of model-suggested heat and water management as well as mass transport control. There have been many heat and water management strategies proposed so far, for example, the cathode is coated by polytetrafluoroethylene (PTFE) to help evacuate the liquid water to the electrode/gas channel interface where the liquid water can evaporate and be removed by convection via air stream; the anode-cathode pressure differential is increased to minimize the anode dehydration; high stoichiometry and isothermal conditions are maintained to provide uniform reacting conditions over the active area for fuel cells; manipulation of in-plane gradients is employed to reduce the performance loss involving kinetic, ohmic and mass transport overpotentials, by tailoring the material properties and structure of the MEA.

Although good agreement between experimental results and model predictions has been achieved, the performance models reviewed here demonstrated different merits. The PEMFC semi-empirical equations show that model-predicted polarization curves will exhibit the correct shape, as long as the logarithmic drop-off in the low current density region, the linear ohmic losses in the middle current density region and the power law relation between mass transport overpotential and current density in the high current density region were captured.

It should be noted that different models may reach different conclusions in terms of distribution of variables as well as heat/water management strategies. For instance, some models predicted that there was no need for outer humidification of reactant gases to prevent membrane dehydration at the anode side, but others have illustrated at high current densities the back diffusion of water from the cathode to anode was not sufficient to keep the membrane hydrated. The model assumptions and boundary equations directly determine the focuses of the modeling results and the conclusions drawn from them.

After comparing the models, one can say that the trend of developing PEMFC performance models is from assuming ideal working conditions of the cell with proper water and heat management such as fully humidified membrane to realizing the unfavorable operating situations such as membrane dehydration at the anode side, from neglect of part of the real phenomena occurring in the MEA components to considering all of them for analysis.

2.8 PEMFC Mathematically Modeling – Durability

2.8.1 Reliability and Durability

Reliability and lifetime analysis play significant roles for PEMFCs in the application of automobiles as well as stationary power sources. How to achieve desired beginning-of-life (BOL) and end-of-life (EOL) performance with minimum cost is the main objective of these types of analyses. In general, reliability is defined as the probability that the components of a system or the system can successfully meet the operational demand within a given period of

time.[68] On the other hand, lifetime prediction is based on the study of durability, whose meaning is similar to that of "wearability", defined as the ability of the system components to resist permanent changes in performance over time.[69]

Although reliability and durability are two terms intertwining each other, there are still some differences between them. It is usually considered that durability along with safety factor and maximum stress assessments comprise reliability, a definition possessing more statistical meanings.[70] Durability is mainly employed to describe the property of components or simple systems consisting of only a few components such as shoes and toys; whereas reliability focuses on the assembly conditions of more complicated systems like cars and electric appliances, and the probability of successful performance by the systems.

Like any other applications, reliability modeling and evaluation of PEMFCs involves common methodologies applied in the field of reliability engineering, including the failure mode and effects analysis (FMEA), fault tree analysis (FTA), reliability block diagram (RBD), accelerated reliability engineering testing and cut set and tie set methods, etc. The goal is to predict the values of reliability parameters such as mean time between forced outrages that can be used for setting up maintenance schedules.[70]

By far the systematic reliability modeling for PEMFCs have not been carried out intensively, since the development of PEMFCs itself is still in a revolutionary stage. Nevertheless, a few papers regarding the durability study of PEMFC components have been published in the literature, the review of which is given in the next section.

2.8.2 Durability Study for PEMFCs

It is generally accepted that the durability requirement for a PEMFC stack in automobile applications is 3000 (4.2 months) to 5000h (7 months); in bus application is 20,000h (5.8 years) and in stationary application is 40,000h (11.6 years).[71] The need to satisfy above requirements with optimum system design and material selection necessitates the PEMFC durability study.

There are two ways to investigate the durability of PEMFCs, one of which is by theoretical analysis, the other of which is by experimental observations. Mathematical modeling can be employed to predict the degradations in a PEMFC with low cost, which would need detailed descriptions of the possible aging phenomena occurring in the cell components, along with proper incorporations of the aging effects to the performance model. Durability test stand can be utilized to examine the structural and property changes of components under realistic working environments, but the testing cost is very high. For example, a bus operation test with PEMFC stack for 20,000h consumed about 2,000,000 Canadian dollars. The running cost includes supplying the fuel and air, building the test station, and the associated expenses such as electricity, maintenance and operator.[70] The normal test stands can measure the durability of cells up to 15,000h, hence is applicable only for automotive and compact type applications. For bus and stationary applications, accelerated aging tests (AAT) are more suitable.

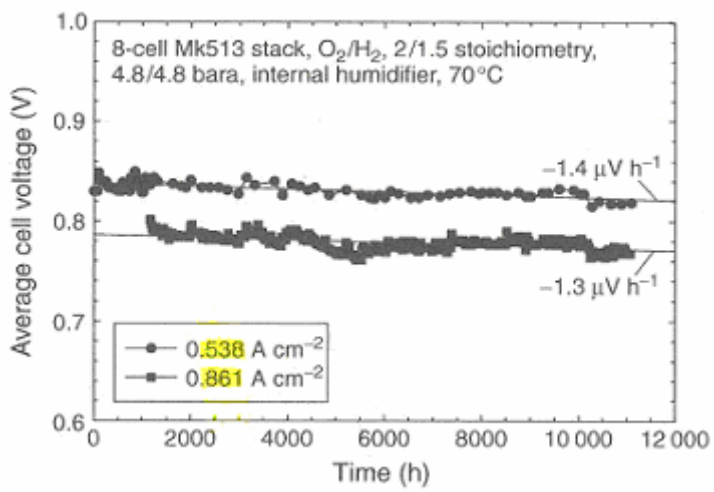

Figure 2-30. Typical voltage-time behavior of a PEMFC stack.[70]

The degradation rate of PEMFCs that has been reported in the literature ranges between -27 and -121 uV/cycle under the urban transit authority (UMTA) driving cycles, though much lower rate was also seen (Figure 2-30).[70] It is necessary to keep in mind that for practical use, PEMFCs may be subjected to the following situations that affect durability to a large extent.

PEMFC stacks are actually used instead of single cells; therefore the issue of uniformity would come to play. High stoichiometric ratio and high operating pressure are not desirable in daily use. Reactant gases may be the reformate and air, and thus not very pure. Low catalyst loading, inexpensive gas diffusion layers and low cost composite bipolar plates are preferred when manufacturing the real-life MEA. All should be considered when studying the PEMFC durability.[70]

2.8.3 Sources of Degradations and Their Effects

The PEMFCs are involved with the strong acidic environment (pH~2), oxygen in gaseous phase and dissolved phase, water in vapor and liquid phase, mechanical compression, contamination, high temperature (90^{o}C for automobiles and higher for stationary applications) and dynamic load cycles. Correspondingly the aging processes may occur in the polymer membrane, catalyst layers, electrodes, membrane-catalyst interface, monopolar/ bipolar plates, and sealing materials. Therefore the aging effects could cause the following variables to change: catalyst activity, reactive catalyst surface area, exchange current density, membrane proton conductivity, interfacial resistance, contact between the cell components, fuel utility, bipolar plate conductivity, thickness of the MEA component, and so on.

In the following section, the sources of degradations in a PEMFC stack and their characterizations as well as effects on performance are browsed through in an order of component position, from outer part to inner part.

2.8.3.1 Current Collectors

The current collectors are usually made of common metals with high electrical conductivity such as copper and aluminum. The presence of reactant gases that includes water vapor at both sides and oxygen at the cathode side may lead to the formation and growth of oxide film, which affects adversely the through-thickness conductivity of the current collector

plates as well as the interfacial resistance between current collector plates and bipolar plates.[69]

In addition, the exposure of copper and aluminum to acid may result in the oxidation of metal into metal ions that are carried away by liquid water and recycled back into the stack. In this way the current collectors may become a contaminant source for the MEA.

2.8.3.2 Bipolar Plates

It is highly possible that the bipolar plates used in the PEMFC stack also age with time. According to Fowler et al., bipolar plates can corrode, foul, crack, permeate hydrogen, deform and leach contaminants.[71] The transport of reactant gases and water vapor, the electron conduction, thermal and hydration cycling as well as the acidic environment and mechanical compression may cause the degradations of the polymeric bindings in the graphite bipolar plate. Once degradations occur, there would be less adhesion forces between the polymer bindings and the graphite flake sheets, which may lead to the "creeping" of materials, loss of integrity, mechanical strength and electrical conductivity, and changes in the dimensions and shape of grooves.[71] Hence aging may increase the ohmic and contact resistance of the bipolar plates, and also disturb the designed flow field.

2.8.3.3 Sealing Materials

By now the selection of the sealing materials remains an unanswered question, though silicon-contained elastic materials are often employed to seal the MEA with the bipolar plates in the lab scale. There is little information from the literature regarding the degradations of sealing materials in a PEM fuel cell. But the possible chemical instability of the sealant to acid and reactant gases may cause the breakdown of the polymer network and release of silicon atoms to the MEA. Swelling experiment and tensile testing can be performed to determine the network crosslink density. Scanning electron microscope - energy dispersive

atomic X-ray (SEM-EDAX) machine can be utilized to examine the components of MEA to detect leached contaminants. This is definitely an issue deserving more investigation.

One consequence of sealant degradation to the operating stack is fuel leakage due to loss of elasticity. It can decrease the stoichiometric ratio of fuel and oxidant (mainly fuel) supplied to the cells, lowering the stack power efficiency by reactant starvation. When reactant starvation becomes really severe, it may turn into cell reversal that is very harmful. The reaction occurring at the cathode during oxygen starvation is $2H^+ + 2e^- \leftrightarrow 2H_2$; during fuel starvation are $2H_2O \leftrightarrow O_2 + 4H^+ + 4e^-$ and $C + 2H_2O \leftrightarrow CO_2 + 4H^+ + 4e^-$.[70] The resultant carbon corrosion by cell reversal may dysfunction the carbon support under the catalyst particles as well as the gas diffusion media, leading to large irreversible degradation in performance. Therefore the oxidative stability of MEA components is important.

2.8.3.4 Electrodes

Since the electrode consists of the gas diffusion layer and catalyst layer which are made from different materials and have different structures and functions, the degradation mechanisms of gas diffusion layer and catalyst layer are reviewed separately below.

2.8.3.4.1 Gas Diffusion Layers (GDL)

The changes of gas diffusion layer (GDL) along with time can be reflected in property parameters including porosity, tuotoristy, hydrophilicity and electrical conductivity. The degradations result from the weakness of carbon material subjected to water and oxygen under high temperature and ion contaminations along with the conduction of electrons. Fowler et al. presented that prolonged exposure of the MEA to water could result in a permanent loss of performance due to GDL degradation, involving changes in carbon surface functional groups and GDL porosity, accumulation of hydrophilic impurities and PTFE loss.

This may in turn affect the gas and liquid water transport through GDL.[70] However, the detailed mechanisms were not provided.

In addition, the GDL/catalyst layer interfacial delamination was reported occurring in a 5-KW PEMFC stack after an operation of 8000h, which propelled the interfacial resistance to infinity and lead to cell failure (Figure 2-31).[72] Fowler et al. explained this phenomenon on the basis of localized tensile stresses that were caused by MEA hydration/dehydration. The decomposition of electrode carbon materials as well as its polytetrafluoroethylene (PTFE) coating under electrochemical stress and attack of chemical species such as HOO· radicals may have accelerated the delamination process.[71]

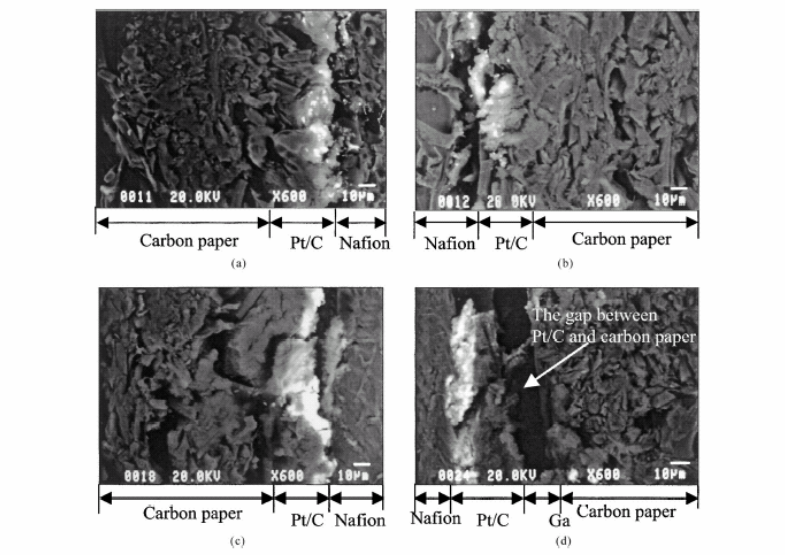

Fig. 10. BS images of the EPMA for MEA before and after 1800 h operation. (a) Anode, before; (b) cathode, before; (c) anode, after; (d) cathode, after.

Figure 2-31. The delamination occurring between Pt/C and carbon paper.[72]

2.8.3.4.2 Catalyst Layers

The degradation of catalyst layer in PEMFCs has been considered a significant factor in PEMFC durability study by many researchers, though the relation between platinum catalyst evolution and change of reaction kinetics has not been resolved. It should be noticed that the catalyst layer structure and morphology and hence the performance of the cell greatly depend

on the catalyst and electrode fabrication methods. The fabrication methods include spread, spray, catalyst powder deposition, ion exchange, electro-deposition, impregnation reduction, evaporative deposition, dry spraying, precipitation, colloidal method catalyst decaling and painting, and so on.[73] In order to improve the carbon monoxide (CO) poisoning resistance, the platinum is usually alloyed with other noble metals. The content of oxide in the catalysts can influence the H_2 and O_2 adsorption characteristics and also the effective platinum surface area (EPSA) that is defined by EPSA = ECA · Pt utilization · catalyst loading, where ECA is the intrinsic catalyst area.[70]

In order to characterize the catalysts under degradation, electrochemical experiments can be performed such as the in-situ X-ray absorption spectroscopy (XAS) for structural parameters, the X-ray absorption near edge structure spectroscopy (XANES) for electronic perturbations, the steady-state galvanostatic polarization (GP) and electrochemical impedance spectroscopy (EIS) for polarization resistance, and cyclic voltammetry (CV) for the active area.[74] Morphological observations can be made by TEM and SEM-EDAX. X-ray diffraction (XRD) can help determine the particle size and indicate the sintering resistance of each catalyst. Dissolution of the catalysts can be analyzed with a spectrophotometer to evaluate the corrosion resistance.[74]

Catalyst sintering is the one of the main causes for the reduction of effective surface area. It has been shown that the catalyst particle sintering occurs at the cathode side more readily, the mechanism of which was proposed as the dissolution-redeposition of small platinum crystallites.[75] In spite that the effective surface area was reduced, the degradation in cell performance was not observed, which was interpreted by the higher intrinsic activity possessed by larger catalyst particles.[75] In fact, an increase of cell performance is usually discerned right after the assembly of test fixture. The reason for it was attributed to the enlargement of the three-phase zone at the catalyst-membrane interface by uptake of the ionomer to the surface of catalysts (Figure 2-32).[75] For the anode side, the lost of catalyst surface area could be due to the formation of Pt-hydrogen complexes and subsequent moving away from the catalyst/membrane interface.[70]

The reduction of the catalyst effective surface area may also result from the degradation of the membrane phase (ionomer) in the catalyst layer. Once degradation occurs, it may not only affect the transport of hydrogen ion, but also the dissolution and diffusion of H_2 and O_2 gases to the reaction sites. In this case the exchange current density of the electrochemical reactions will be decreased.

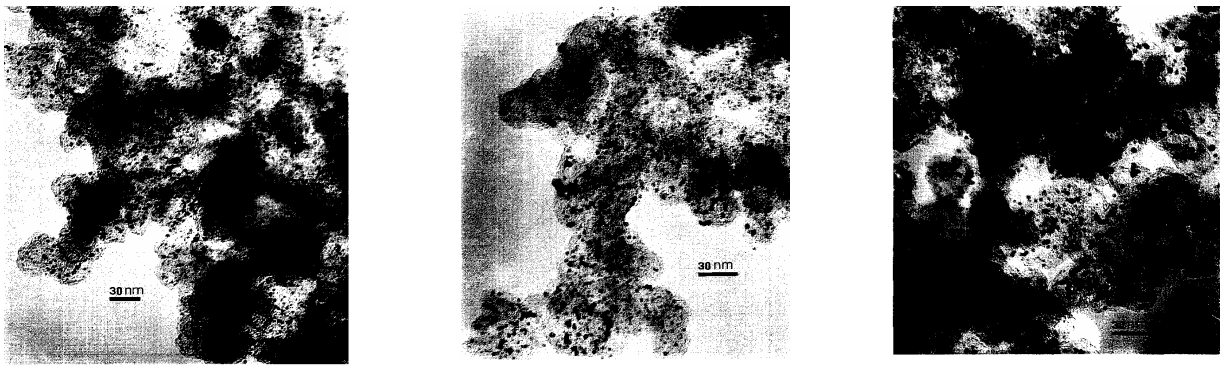

Raw 6h 73h

Figure 2-32. Uptake of electrolyte in the early period of operation.[75]

Besides catalyst sintering, the catalyst poisoning and contamination in a PEMFC can occur via two mechanisms, one of which is the geometrical effect by blocking the sites, e.g. only trace amount of carbon monoxide can block part of the platinum reaction sites; the other of which is via electronic effect such as changing the rate or selectivity of the electrochemical reaction by modifying the strength of chemisorption of the nearby sites.[70] The contaminants may come from the reactant gases, recycled liquid water, the degradation products of diffusion media, sealing material and membrane, as well as the corrosion rust of bipolar plate and current collector. What's more, the corrosion of Pt itself into PtO_2 at the cathode side was suggested in Ahn et al.'s paper, although platinum is a noble metal and has very high corrosion resistance.[72]

2.8.3.5 Ion Exchange Membranes

The time behavior of ion exchange membrane relies on its chemical structure. For instance, the earlier polystyrene sulfonic acid (PSSA) membrane were proven to degrade at a higher rate compared to Nafion membranes, due to the chemical attack of peroxide intermediates to the tertiary hydrogen at the α-carbon of the PSSA chain, leading to the simultaneous loss of aromatic rings and the sulfonic acid ($SO_3^-H^+$) groups.[76] The PSSA membrane has relatively low mechanical and dimensional stability. It may physically deform, crack and form some types of perforation, especially when hydration/dehydration cycling- induced local stresses or puncture of catalyst particles is taking place.

On the other hand, the Nafion 120 membranes were reported showing no deterioration (<0.1%) after 5000h of operation and only 2% degradation after 100,000h of operation.[76] The dissolution and thinning of Nafion membranes occurs at a comparatively slow rate, though pinholes may form at the end. Pinholes can cause the crossover of reactant gases. In this case, the fuel and oxidant react with each other directly on the surface of platinum without generating any electricity. The heat released by fuel and oxidant recombination could be sufficient to melt a small portion of the membrane around the pinholes and make the pinhole even bigger.[76] The sizes and locations of pinholes can be detected by use of an infrared camera, as shown in Figure 2-33 below.[71]

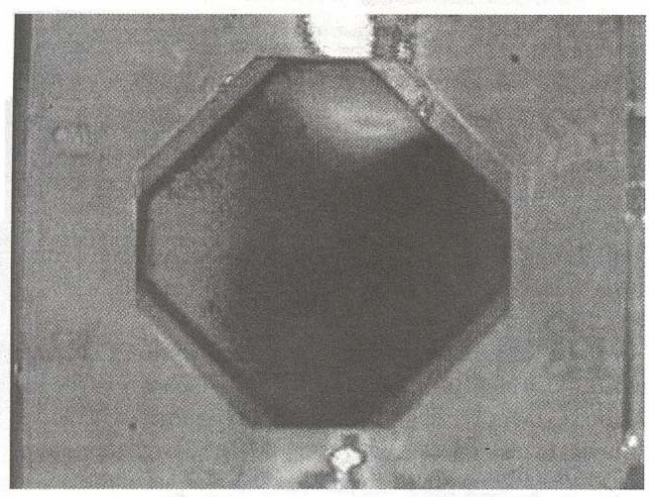

Figure 2-33. The formation of pinholes in the membrane, which can be detected by Infrared

camera.[71]

Stucki, Scherrer, Wilson et al. proposed the detailed membrane thinning mechanisms for fluorinated membranes.[76] It has been shown that the dissolution of PTFE backbone mainly occurs at the anode side. The gaseous oxygen molecules first dissolve into the membrane, diffuse from the cathode side to the anode side, and then react with hydrogen molecules chemisorbed on the anode platinum surface and generate hydrogen peroxide (H_2O_2). Because the reduction of hydrogen peroxide is inhibited at the H_2-covered Pt electrode, hydrogen peroxide accumulates at the anode Pt/membrane interface and diffuses back into the membrane. Following this step, the hydroxyl and hydroperoxy radicals are produced within the membrane, which attack the – CHF- groups in the polymer backbones as well as the sulfonic acid groups. The above processes can be summarized in a series of proposed chemical reactions as shown below:[76]

Step 1: $2Pt(s) + H2 \rightarrow 2Pt{\cdot}H$

Step 2: $Pt{\cdot}H + O_2 \rightarrow Pt{\cdot}HO_2$

Step 3: $Pt{\cdot}HO_2 + H{\cdot} \rightarrow Pt(s) + H_2O_2$

Step 4: $H_2O_2 + M^{2+}$ (Fe^{2+}, Cu^{2+}…) $\rightarrow M^{3+} + OH{\cdot} + OH^-$

Step 5: $OH{\cdot} + H_2O_2 \rightarrow H_2O+HO_2{\cdot}$ (hydrogen peroxide radical attacks the PEM)

It can be seen from above mechanism that the membrane degradation is influenced by the permeation of oxygen and the occurrence of contaminant metal ions in the membrane. If the oxygen dissolution and diffusion rates through the membrane become larger due to higher water content, it may transport more oxygen to the anode side and result in increased peroxide formation at the hydrogen electrode. The presence of liquid water in the membrane could also help transport leached impurities, which may decrease the membrane proton conductivity and water diffusion coefficient via the cation effect, since a large portion of the sulfonic acid groups may be attached with other cations instead of protons due to the high affinity.[76] Nevertheless, the lack of water in the membrane can decrease the proton

conductivity, change membrane dimensions and shape by shrinking, and put the membrane under mechanical-electrochemical stresses.

Membrane contamination is considered as a degradation source that always impairs the cell performance. Experimentally, Ahn et al. observed a thin film of silicon gasket formed on the surface of Nafion membrane by use of electron probe micro analyzer (EPMA).[72] The EPMA images revealed the presence of Si and O elements in the MEA and silicon-containing substances on the surface of membrane (shown in Figure 2-34). It was explained by the decomposition of the silicon gasket and leakage of the coolant.[72] Step 4 of the membrane dissolution mechanism demonstrates that metallic ions are involved in the formation of hydrogen peroxide radicals that attack the polymer chain. Therefore, the release of metallic species from the other components of a PEMFC may trigger the dissolution reaction of membrane. In addition, recent work has reported that the presence of chloride ions in the membrane could increase the yield of H_2O_2 at the anode by 20%. The carbon monoxide (CO) existing on the platinum surface shifted up the H_2O_2 yield by approximately 80%.[76]

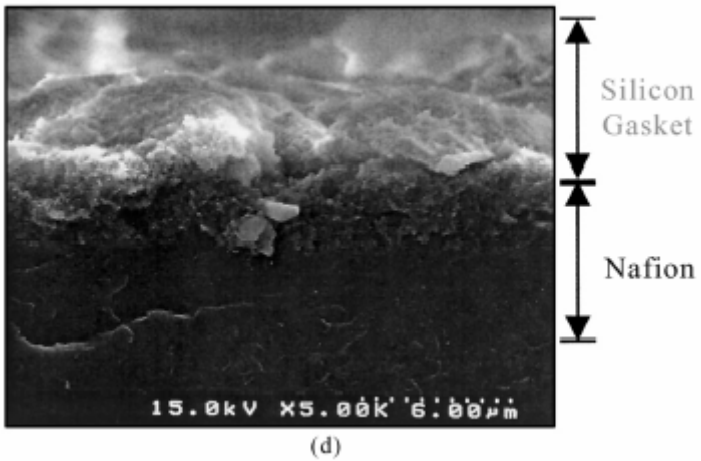

Figure 2-34. The silicon gasket observed on the surface of Nafion membrane.[72]

Two parameters are usually utilized to describe the degree of membrane degradation, one of which is the bonds broken per mole in the polymers, the other of which is the change in ion

exchange capacity (IEC). Therefore the membrane weight measurements as well as IEC determination are often performed to characterize the degradation. The membrane dissolution process can be simulated by placing the Nafion samples in Fenton's reagent, containing a small amount of hydrogen peroxide (3%) and Fe^{2+} ion accelerator (4ppm) in the form of ferrous ammonium sulfate. Aliquots of the reagent solution were then analyzed by titration with NaOH to its phenolphthalein end point.[76]

Fluoride ions, low molecular weight perfluorcarbon sulfonic acid and CO_2 were found in the solution after Nafion 120 membranes.[76] The cross-sectional SEM/EDX analysis of MEAs for S, Pt, F and foreign species (Si, Ca, Mg and Fe) was performed and the membrane was found to release F, C and S containing products in a fixed ratio.[76] It has been suggested that the accelerated degradation of Nafion membranes follows first order kinetics in terms of logarithmic ion exchange group loss. In other words, the reactions occurring in the Fenton's agents can be represented with a single rate constant k as $\log(\%\,\text{degradation}) = kt$.[76] From the slope of the Arrhenius plot, $k = Ae^{-E/RT}$, the activation energy of the reaction, E, was determined as 18 kcal for Nafion membranes.[76] It needs to be emphasized here that membrane thinning and dissolution might actually enhance the cell performance due to the reduction of membrane thickness and hence the overall resistance to proton conduction. Experiments indicated that freezing is not damaging to the MEA. When PEMFCs are used for stationary applications, high temperature (>200^{o}C) can decompose the sulfonic acid groups of the membrane.[70]

2.8.4 Durability Mathematical Modeling

Understanding of the degradation sources and mechanisms in a PEMFC stack by itself is not adequate to investigate the stack behavior with respect to time, since the operating conditions also have a considerable impact on the cell performance and lifetime. For example, the impact of degradations on performance is smaller for pure oxygen than for air, for high stoichiometric ratio than low stoichiometric ratio.[70] Using reformate as the fuel may

accelerate the degradation process, due to the reduction of catalyst effective surface area by CO-like adsorptions. In turn, CO tolerance will be decreased with aging because the fraction of catalyst sites to support H_2 oxidation decreases. Manipulation of in-plane gradients such as high stoichiometry and isothermal conditions could provide uniform reaction environment for PEMFCs, slowing down the degradation rate of the cells.

Therefore it is necessary to incorporate the aging processes into the cell performance analysis quantitatively in a mathematical model, because of the coupling nature of the steady-state operation and component degradation. The PEMFC durability study by mathematical modeling is believed to represent the changes occurring in a PEMFC in a more comprehensive and cooperative manner, which enables it to predict the voltage (efficiency) - time behavior of PEMFCs more accurately. Unfortunately there have been very limited papers published in this area, most of which adopted the semi-empirical methodology employing a few model parameters with ambiguous physical significances. Detailed mathematical descriptions are desired based on a combination of theoretical analysis and experimental characterization. The available durability models are reviewed below.

In 2001 Jiang and Chu developed the empirical equations to describe the voltage-time behavior of PEMFC stacks at constant current density.[77] A 42-cell stack was tested. When either ambient temperature or current density was too high, the stack exhibited rapid falling of cell voltage within a short period of time. It was concluded that inadequate mass transfer was likely the reason for the voltage dropping and membrane dehydration was responsible for the inclination of the voltage-time curves. The parametric study was undergone for the coefficients in the empirical equations, including the difference between the ambient temperature and the cell temperature $T_a - T$, time factor S, temperature to initial stack mass transfer overpotential T_m and voltage decreasing rate A. The calculated curves of stack temperature, voltage and current as a function of time were compared with the measured results, which showed a good fit (see Figure 2-35).

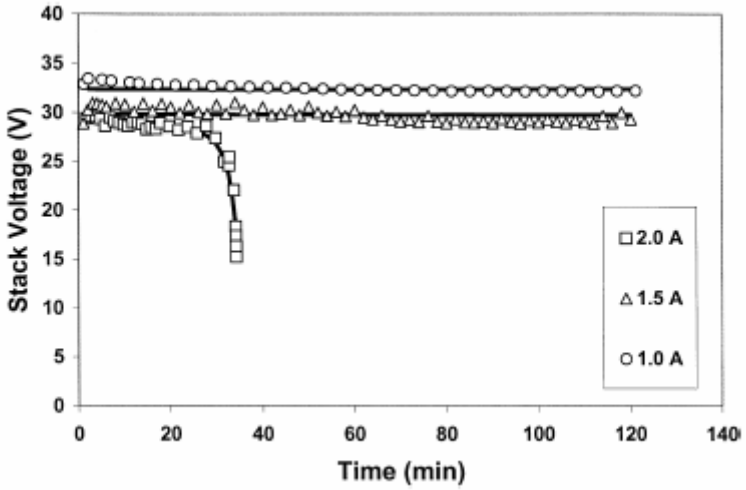

Figure 2-35. Stack voltage as a function of time: comparison between model predictions and experimental data.[77]

Fowler, Mann and Amphlett et al. incorporated the voltage degradation into the generalized steady-state model (GSSEM) by expressing the change of model parameters in semi-empirical equations in 2002.[78] New terms was introduced to account for the MEA aging, based on the concepts that the water-carrying capacity of the membrane deteriorates with time; and the apparent catalytic rate constant and active site density changes due to catalyst degradation. A third term dealing with the decrease in the rate of mass transfer within the MEA was also presented. Taking degradations into account, the ζ_2 parameter in the GSSEM model was rewritten as: $\zeta_2 = k_{DR} \times \frac{age}{T} + k_{cell}^0 + 0.000197 \ln A + 4.3 \times 10^{-5} \ln c_{H_2}^*$. The voltage-time behavior of a single cell was measured to compare with the model predictions. The membrane conductivity λ and k_{cell} were back calculated from the experimental data in conjunction with the GSSEM, and then plotted as a function of time. Both λ and k_{cell} decreased with time. It should be noted that this model did not account for the impact of contamination, thermal shocking and the hydration cycling situations as well as the coupled effects of these factors.

2.8.5 Summary of Durability Study

In a similar fashion to performance modeling, durability study of PEMFCs also has an interdisciplinary nature. It may not only involve the electrochemical, chemical, mechanical and physical characterizations, but the mathematical and statistical implementations as well. In a recent summary of PEMFC durability study, Fowler et al. attributed the degradations to reversible and irreversible changes respectively, depending on whether the performance loss will be recovered after the degradation source such as poor water management is eliminated from the cell.[76] However, essentially all changes induced by degradation sources should be considered irreversible, because the material properties are already affected by the operation history. Nevertheless, the recognition of above statement may lead to over-complex models that require simplifications. Well-defined assumptions and initial conditions along with focusing on the most predominant and unavoidable degradations may be a way to deal with the durability model without losing too much accuracy. The tradeoffs between model completeness and applicability will be inescapable for PEMFC durability study.

The cell uniformity and the coupling effects of cell degradation should also be discussed here for PEMFC stacks. The influence of neighboring cells on each other cannot be neglected in stack durability. From the statistical point of view, the cell reliability at time t for the stack, $R_{system}(t)$ is the nth power of the single cell reliability as $R_{system}(t) = [R_{cell}(t)]^n$.[70] Consequently, a high level of cell-to-cell consistency in the stack is required in a durable PEMFC stack, which can only be achieved with a high degree of MEA reproducibility by tight control of MEA fabrication conditions. Finally, the concept of primary and secondary effects of degradation needs to be taken into consideration.[70] The concept of secondary effects indicates the interplay of the different degradations and their coupled functions to the cell performance. A good example is: the metallic ions not only increase membrane resistance, but also affect the electro-osmotic drag due to the fact that protons have the smallest electro-osmotic drag coefficient in comparison to other ions. Insufficient supply of hydrogen may lead to cell reversal and then localized loss in catalyst surface area. It can alter the current distribution by

increasing the current densities in unaffected areas. These kinds of effects should be accounted for during the modeling work.

2.9 Summary and Limitations of PEMFC Modeling in the Literature

In summary, recent PEMFC performance models in the literature addressed two-dimensional or three-dimensional geometries, multi-component multi-phase gas flow in electrode gas channel, diffusion layer and catalyst layer, electrochemical reaction kinetics, ion transport, water (liquid and vapor) transport in membrane as well as heat transfer.

However, most of the performance models did not model the liquid water flow in gas channels, did not account for the phase change between water vapor and its liquid form and the corresponding absorbed/released potential heat, and did not account for the heat generated by the electrochemical reactions via the calculations of Gibbs free energy. Most of the three-dimensional models are still pseudo-3-D models with two directions on the membrane plane and one direction along the gas channel. Hence the shoulder effect of the gas distributor on cell performance needs further study. More robust solution approaches are required to solve the models accurately. The availability of input parameters (also to be a function of time, *f(t)*) should be improved. Designs of in-situ measurements for the PEMFCs are necessary to validate the individual pieces of model results. What's important, the transient models that describe the performance of PEMFCs under various loads are too less.

As for the durability study, a question was brought up recently by the researchers: could small active area cells used in fuel cell experiments embody all of the degradation processes occurring in large cells?[70] The answer to this question is still under investigation. It can be seen that the durability study of PEMFCs by now is in a stage of qualitative descriptions and interpretations. Aging tests were performed and degradation mechanisms were proposed, but durability models that quantatively incorporate the effects of aging process and predict the

polarization curves of cell with time have not been fully developed. These research facts motivate our PEMFC durability work, as stated in the next section.

2.10 Objectives of Current Work

A large number of mechanistic and semi-empirical models have been proposed to investigate the voltage-current density behavior of PEMFCs (the polarization curve), but none of them are able to predict the performance of PEMFCs well under various operating conditions. In addition, model parameters with ambiguous physical meanings and arbitrary values are employed in order to fit the experimental data, which has limited the roles of these models as a tool for PEMFC design optimization and operation. Currently, there is no real mechanistic model for the durability of PEMFCs, though the voltage-time curves and corresponding empirical equations have been presented in several papers.

The ultimate aim of our research is to establish a mechanistic model of PEMFC durability on the basis of the steady-state performance model. The unique feature of this effort will be incorporations of aging processes into the model equations by taking the property parameters of MEA, bipolar plates and current collector plates as functions of operation conditions and initial material selection. Those parameters include the interfacial resistance between the membrane and electrode, catalyst activity, membrane proton conductivity, fuel crossover, fuel leakage, and the electrical conductivity of the bipolar plate and current collector etc. After the proper degradation-related source terms and constitutive equations are specified, the adopted steady-state model will be solved with the variations of interested model parameters under the prescribed constrains set up by the initial conditions and model assumptions. Thus the polarization curve at a specific time and the voltage-time behavior of PEMFCs can be predicted by the model and the results will be compared to the experimental data from the literature or obtained as part of this effort. The proposed degradation mechanisms as well theoretical descriptions will then be validated by the trial-and-error method. Once the validity

of the model is proved, it may be utilized for further PEMFC design, operation and lifetime analysis.

The above statements present a guideline for our research in the long run. Due to its complexity, the PEMFC durability research has to be divided into smaller pieces and implemented step by step. In this dissertation, the experiments and results that are presented in details focus on the mechanical, proton conduction characterizations of membrane materials, as well as the long-term aging diagnosis of MEAs under simulated driving conditions with cyclic current profile. A phenomenological semi-empirical model has been set up to reflect the impact of end-of-period diagnosis results on the MEA performance. These research achievements launched the first milestone towards our ultimate goal of mechanistic durability modeling and provided valuable information for the PEMFC lifetime analysis.

Chapter 3. Tensile Behavior of Nafion® and Sulfonated Poly(Arylene Ether Sulfone) Random Copolymer Membranes and Its Morphological Correlations[113]

Dan Liu[1], Steven Kyriakides[2], Scott W. Case[3], John J. Lesko[3], Yanxiang Li[1], James E. McGrath[4]

[1] Macromolecular Science and Engineering, Virginia Polytechnic Institute and State University, Blacksburg, VA 24061

[2] Materials Science and Engineering, Virginia Polytechnic Institute and State University, Blacksburg, VA 24061

[3] Engineering Science and Mechanics, Virginia Polytechnic Institute and State University, Blacksburg, VA 24061

[4] Department of Chemistry, Virginia Polytechnic Institute and State University, Blacksburg, VA 24061

3.1 Abstract

In this paper, the tensile stress-strain behavior of Nafion® (N117) and sulfonated Poly(arylene ether sulfone) random copolymer (BPSH35) membranes were explored with respect to the effects of initial strain rate, counterion type, molecular weight and the presence of inorganic fillers. The yielding properties of the two films were found being most affected by the change of strain rate. The stress-strain curves of Nafion® films in acid and salt forms exhibited larger deviations at strains above the yield strain. As the molecular weight of BPSH35 samples increased, the elongation at break was shown to improve significantly. Enhanced mechanical properties were observed for the BPSH35-ZrPP (zirconium phenylphosphonate, 2%, w/w) composite membrane compared to its matrix BPSH35 film. The stress relaxation behavior of Nafion® and BPSH35 membranes was measured at different strain levels and different initial strain rates. Master curves were constructed in terms of stress relaxation modulus and time plots in double logarithm scale. A three-dimensional "bundle-cluster" model was proposed to interpret the above observations, combining the concepts of elongated polymer aggregates, proton

conduction channels as well as states of water. The rationale focused on the polymer bundle rotation/interphase chain readjustment before yielding and polymer aggregates disentanglements/ reorientation after yielding.

Key words: Mechanical Behavior, Morphology, Proton Exchange Membrane, Bundle-Cluster Model

3.2 Attribution

Dan Liu: Performed the tensile property measurements (including casting the BPSH35 films) and atomic force microscopy imaging and developed the "Bundle-Cluster" model.
Steven Kyriakides: co-performed the tensile property measurements as a summer undergraduate student research program (SURP) student.
Scott W. Case: Advised on the tensile experiments and guided the writing of the manuscript.
John J. Lesko: Reviewed and guided the writing the manuscript.
Yanxiang Li: Synthesized the BPSH35-MW polymers.
James E. McGrath: Designed the synthesis of the BPSH35-MW polymers and provided valuable discussions with the primary author.

3.3 Introduction

Increasing effort has been focused on the development of a new generation environmental-friendly hybrid electric vehicles (HEVs) during the past twenty years. As one of the candidate power sources for the HEVs, proton exchange membrane fuel cells (PEMFCs) present a promising power source in comparison with rechargeable batteries or other hybrid sources. PEMFCs use sulfonated solid polymers as the electrolytes, making them suitable for transportation applications in terms of room temperature start-up, moderate temperature operation, and corrosion reduction.[2]

Durability and cost are the two main obstacles for PEMFC commercialization.[79] The importance of long-term mechanical behavior of proton exchange membranes (PEMs) in a fuel cell has been

often underestimated. PEMs must possess not only good proton conductivities, gas separation, but stable mechanical properties for long times (~ 5000 h in operation). PEMFCs operated in automotive applications demand constant, ramp and cyclic power outputs. During vehicle operation, the fuel cell must respond to and endure these transient conditions. The corresponding membrane and electrode water sorption/desorption and swelling/contraction processes can produce compressive/tensile stresses within the membranes and shear stress at the membrane-electrode interfaces. Due to the constraints imposed by the bipolar plates, stress relaxations occur within the membrane-electrode-assembly (MEA). Meanwhile, a membrane thinning process, initiated by local mechanical creep and chemical degradation (the loss of fluoride ions due to hydrogen peroxide radical attack) may cause the mechanical properties of the membranes to deteriorate. As the stresses induced during operation are comparable to the aged strength of the membrane, pinhole ruptures in the membrane and weakened adhesion at membrane-catalysts-gas diffusion layer (GDL) interfaces may occur, leading to increased reactant gas crossover, increased interface resistance and ultimately degradation of performance.

To predict the long term performance of PEMFCs, degradation mechanisms of PEMFC components and their kinetics must first be understood. Quantitative durability modeling is the next step that is needed. For membrane pinhole modeling, the tensile and compression behavior of membranes under various temperature and humidity combinations must be understood to define constitutive relations. Cyclic hygro-thermal mechanical loading conditions should also be applied to correlate the change of ionomer morphology with aging as a function of time/cycles. Unfortunately, little systematic work has been undertaken in this area and very few papers in the literature have focused on mechanical testing of PEMs. Among the limited sources that are available, Kyu and Eisenberg et al. employed dynamic mechanical analysis (DMA) and measured the mechanical properties of Nafion® with different equivalent weights (EW), counterion types, temperatures and water contents in the 1970s.[80] They obtained the storage moduli of the membranes, assigned and compared glass transition temperatures, and developed stress relaxation master curves for films in air as well as in water. The concepts of ionic aggregation from multiplets to ionic-clusters and crystallinity of hydrophobic phases were adopted to explain the occurrence and shifts of glass transition temperatures.

Kawano, Wang and Palmer et al. investigated the stress-strain behavior of Nafion® 117 membranes using DMA with different solvent contents and with different cations.[81] The results showed that the initial moduli of Nafion® membranes decreased with the increase of water content as well as the addition of low carbon alcohols. When the cation was varied, the initial moduli of Nafion® in the salt forms increased with cation type (with an order of Li^+, Na^+, K^+, Cs^+ to Rb^+). It should be noted that the ultimate properties of some of the specimens (those with high modulus or large elongation at break) were not presented due to instrument limitations.

Recently, Bauer, Denneler and Willert-Porada examined the storage moduli E', $\tan\delta$ and swelling ratios for Nafion® 117 films in both the machine direction (MD) and transverse direction (TD) at five different humidity levels.[82] It was found that water stiffened the membranes at elevated temperatures, a behavior which they explained by the presence of stabilized hydrophilic network clusters. The mechanical strengths of the membranes were shown to increase with water uptake at very low humidity levels. Formation of hydrates as well as hydrogen bonding was suggested as the underlying causes.

In general, the papers summarized above did not present a clear mechanical-morphology relationship in PEMs, which is critical for modeling their long term behavior under hygro-thermal mechanical conditions. Quite a few Nafion® morphological models have been proposed in the literature, such as the ionic-cluster model presented by Gierke et al. in 1983 (still the most frequently cited model to describe the PEM structure-property relationship),[83] the Eisenberg-Hird-Moore (EHM) model in the 1990s,[84] the core-shell model by Haubold et al.,[85] and the elongated polymer aggregates model by Rubatat, Gebel and Diat et al.[86-89] Most of these models focus on either the organization of sulfonic acid groups associated with proton conduction,[83,90-92] or the arrangement of backbone structure supported by X-ray scattering experiments.[86-89,93] A comprehensive model taking into account both effects does not exist.

In this paper, a mechanical-morphological correlation is attempted based upon the “dry” membrane mechanical testing observations. The tensile stress-strain behavior of Nafion® 117 and sulfonated poly(arylene ether sulfone) random copolymer membranes are explored under ambient conditions with respect to initial strain rate, counterion type, molecular weight and

inorganic additives. The stress relaxations of the membranes are also examined at different strain levels and different initial strain rates. After considering the tensile behavior and proton conductivity (details given in a separate publication), we propose a new "bundle-cluster" model that depicts the co-continuous hydrophobic/hydrophilic phases in PEMs, combining the concepts of "elongated polymer aggregates",[86-89] nanophase-separated "ionic-cluster",[83,90] and states of water[94] in a PEM. The model is shown to present a rational description of the "dry" PEM system and will be extended to include the environmental effects in future studies.

3.4 Experimental

3.4.1 Materials

Commercial Nafion® 117 films (N117-Na, extruded, DuPont, Fuelcellstore.com) were used as-received in their sodium form and also acidified by "method two",[95] which consists of boiling the films in 0.5 M H_2SO_4 for 2 h, and then boiling in deionized water for another 2 h. After acidification, the Nafion® acid form films (N117-H) were dried and flattened between two glass plates overnight in a vacuum oven at ca. 70 ^oC to make the films suitable for tensile testing.

In addition, sulfonated poly(arylene ether sulfone) random copolymer materials with 35% of sulfonation in their potassium form, with ~ 40K number average molecular weight (BPS35-R, intrinsic viscosity (I.V.) = 0.66 with NMP and LiBr, Hydrosize Technologies, Inc.),[96] and controlled number average molecular weights (BPS35-MW, 20K, 30K, 40K, 50K, 70K, Virginia Tech)[97] were obtained. The BPS35-MW random copolymers were end-capped using 4-*tert*-butylphenol (TB, Fisher) except for the 70K random copolymer, which was synthesized using the same procedures as the BPS35-R Hydrosize materials. The materials in particle form were dissolved in N, N-dimethylacetamide (DMAc, Fisher) at ca. 40 ^oC for two days, forming yellow transparent solutions. The solutions were then filtered onto a 7.5 × 9.0 cm glass plate and dried under an IR lamp using 140-Watt power for two days. The films, on the glass plates, were placed in a vacuum oven for 2 h at ca. 60 ^oC to further dry them. Subsequently, the films were removed from the vacuum oven and placed in deionized water for 4 h. Following this step, the films were peeled from the glass plates and the excess water was removed. Before acidification, the films

were dried in a vacuum oven at ca. 100 ^{o}C overnight. The series of BPS35 films were also acidified based on method two. Finally, the acidified films (BPSH35 series) were dried and flattened overnight using a vacuum plate at ca. 75 ^{o}C. The BPSH35-ZrPP composite films with 2% (w/w) of zirconium phenylphosphonate (ZrPP) additives were tested as-received. The BPSH35-ZrPP film preparation procedures were described in ref 98.

3.4.2 Measurements

The N117 and BPSH35 films were equilibrated under ambient conditions for a minimum of 72 h prior to mechanical testing. Each film was cut into straight-sided specimens 60-mm long and 12-mm wide. For N117 specimens, the longitudinal direction was in alignment with the machine direction (MD) of the film. The measured thicknesses of the N117 specimens were close to the nominal thickness, i.e. 0.178 mm. For BPSH35 materials, isotropic properties were assumed due to the solution-casting procedure employed. This procedure resulted in thicknesses of BPSH-R samples that varied slightly within a range of 0.125 to 0.150 mm. The BPSH35-MW samples ranged in thicknesses from 0.025 to 0.050 mm.

3.3.2.1 Uniaxial Tensile Testing

Uniaxial tensile loading tests were performed using a screw-driven Instron 4468 Universal Testing Machine with a 1 kN load cell under ambient conditions ca. 23 ^{o}C and 40% RH. Pneumatic grips (similar to Instron 2712 series pneumatic grips) with elastomeric gripping surfaces were utilized to hold the ends of samples in the Instron machine with ~ 200 kPa of pressure. The gauge lengths were all set to 40 mm. At least three replicates were tested for N117 films along the MD, while one or two replicates were examined for BPSH35 films. In this context initial strain rate has the definition of crosshead displacement speed divided by original gauge length. When studying the initial strain rate effects on the mechanical behavior of N117 and BPSH35-R films, five different nominal initial strain rates, 0.025, 0.07, 0.12, 0.3, and 0.7 min^{-1} were applied. For comparison purposes, all BPSH35-MW samples were tested using the same strain rate of 0.12 min^{-1}.

3.4.2.2 Stress Relaxation

Stress relaxation tests were conducted on the same Instron machine with the same pneumatic grip pressure and sample dimensions under ambient conditions. The N117-H stress relaxation behavior was investigated at different strain levels including 1, 3, 6, 7.5, 25, 50, 100 and 200% strain with a 0.12 min^{-1} initial strain rate. The initial strain rate effects on N117-H stress relaxation were studied at 3 and 50% strain. For BPSH35-R materials, only the stress relaxation at different strain values (1, 2.5, 7.5, 10, 25, and 40%) were tested at an initial strain rate of 0.12 min^{-1}.

3.4.2.3 Membrane Water Content

After uniaxial loading and stress relaxation measurements, the specimens were dried under vacuum at ca. 100 ^{o}C overnight and their dry weights were measured. Sample water contents were calculated using the following equation:

$$\text{Water content (\%)} = \frac{\text{wet weight - dry weight}}{\text{dry weight}} \times 100 . \qquad -(39)$$

The water contents of the N117-H and N117-Na specimens were determined as 5.3 ± 1.5% (number of water molecules per sulfonic acid group, $\lambda \sim 3$) and 4.8 ± 0.8% immediately after the tensile testing. The BPSH35-R samples had water contents of 14.5 ± 3.8% ($\lambda \sim 6$) while the BPSH35-MW samples had relatively lower water contents of 10.5 ± 2.1% ($\lambda \sim 4$).

3.5 Results and Discussion

There have been many new PEMs developed to meet the Department of Energy (DOE) target for PEMFC high temperature low humidity operation, that include various types of fluorinated and hydrocarbon structures as the polymer backbone.[99-101] As reported previously, the ionic groups in PEMs act as physical crosslinks between polymer backbone, the electrostatic interactions of which can be altered by the presence of solvent molecules, the counterion type, and the

organic/inorganic additives.[80,81,102,103] The polymer backbone and the ionic groups form unique morphological structures that lead to the special properties of PEMs: proton conduction, gas and electron impermeability, chemical resistance and mechanical properties. To further examine the PEM morphology, we measured the tensile behavior of "dry" N117 and BPSH35 materials and interpreted the results along with the proposal of a new "bundle-cluster" model.

3.5.1 Uniaxial Loading

3.5.1.1 Initial Strain Rate Effects

Typical stress-strain curves of N117-H films under ambient conditions at five initial strain rates are shown in Figure 3-1. The shape of the curves are similar to that of Teflon (PTFE) films[81] as well as Nafion® precursor with an EW of 1100,[104] although the crystallinities of these films were different (PTFE: almost 100%;[81] 1100 EW Nafion® precursor: ~ 23%;[91] and 1100 EW Nafion®: ~ 3-12%[91]).

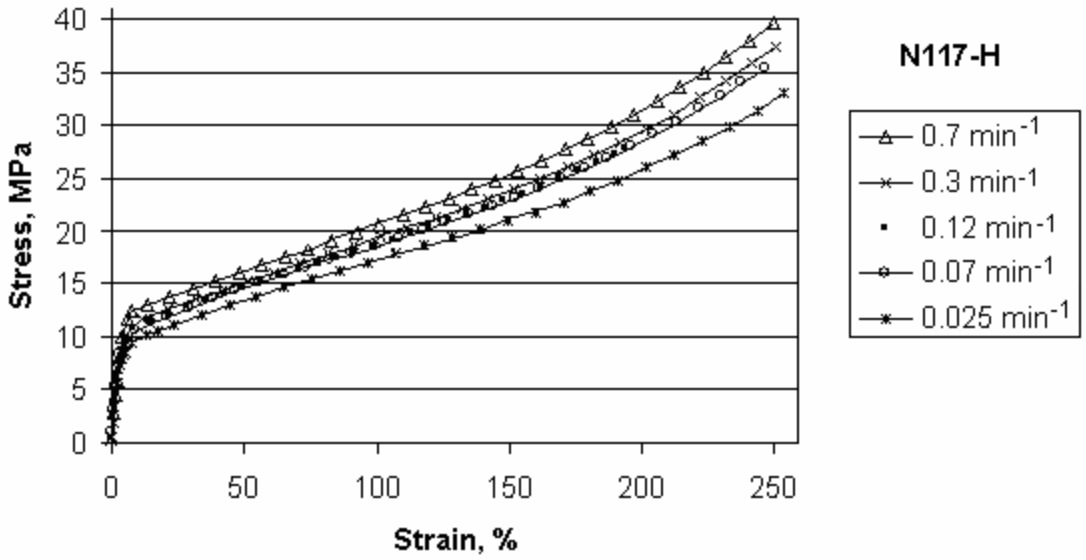

Figure 3-1. Stress-strain curves of N117-H films at different initial strain rates under ambient conditions show that the yielding behavior was affected.

It is worthwhile mentioning that for N117-H, linear deformations occurred at very low strains (< 0.5%). We define the initial modulus as the ratio of stress to strain at 0.2% strain. Initial strain

rate had little effect on the initial modulus and ultimate properties of N117-H films, as summarized in Table 3-1. In our study, the yield of N117-H films was defined as the point where the tangent moduli (local slopes of stress-strain curve) dramatically changes. The results showed that yield stresses increased and the yield strains decreased with an increase in initial strain rate. After yielding, the tangent moduli of five stress-strain curves were comparative until approximately 200% strain. The initial strain rate effects were also investigated for N117-Na membranes and found to show similar trends to those of N117-H.

Table 3-1. Summary of selected tensile properties of N117-H films at different initial strain rates under ambient conditions[a]

Initial strain rate (min^{-1})	Initial Modulus (MPa)	Yield Stress (MPa)	Yield Strain (%)	Ultimate Strength (MPa)	Elongation at Break (%)
0.7	270 ± 4	12.6 ± 0.2	6.6 ± 0.8	36.5 ± 2.4	251 ± 14
0.3	253 ± 7	11.7 ± 0.1	7.5 ± 0.3	34.2 ± 2.9	235 ± 14
0.12	256 ± 18	10.9 ± 0.3	7.8 ± 0.9	25.9 ± 2.1	177 ± 27
0.07	263 ± 10	10.8 ± 0.2	8.3 ± 0.6	36.7 ± 2.3	262 ± 16
0.025	250 ± 5	9.8 ± 0.4	9.4 ± 0.5	31.8 ± 2.3	250 ± 9

[a] Samples prepared using the same treatments and tested under the same environment. The water contents were 5.3 ± 1.5%.

The BPSH35-R films were tested under ambient conditions with the same sets of initial strain rates (Figure 3-2). These films exhibited nonlinear stress-strain behavior starting at extremely small strains. In contrast to N117-H samples that deform uniformly until break, conspicuous yielding and necking behavior took place in the BPSH35-R films during the uniaxial loading. The resulting stress-strain curves resembled those characteristic of the cold-drawing behavior of thermoplastic polymers. Consequently, the yield was defined as the point where the slope of the stress-strain curves reached a value of zero. From Figure 3-2, a clear relationship was illustrated between the elongations at break and the initial strain rates. The yielding behavior and ultimate strengths were influenced to some extent, but not as much as the elongation at break. The trend between initial moduli and initial strain rates was not distinct. Table 3-2 summarizes the tensile parameters for BPSH35-R films.

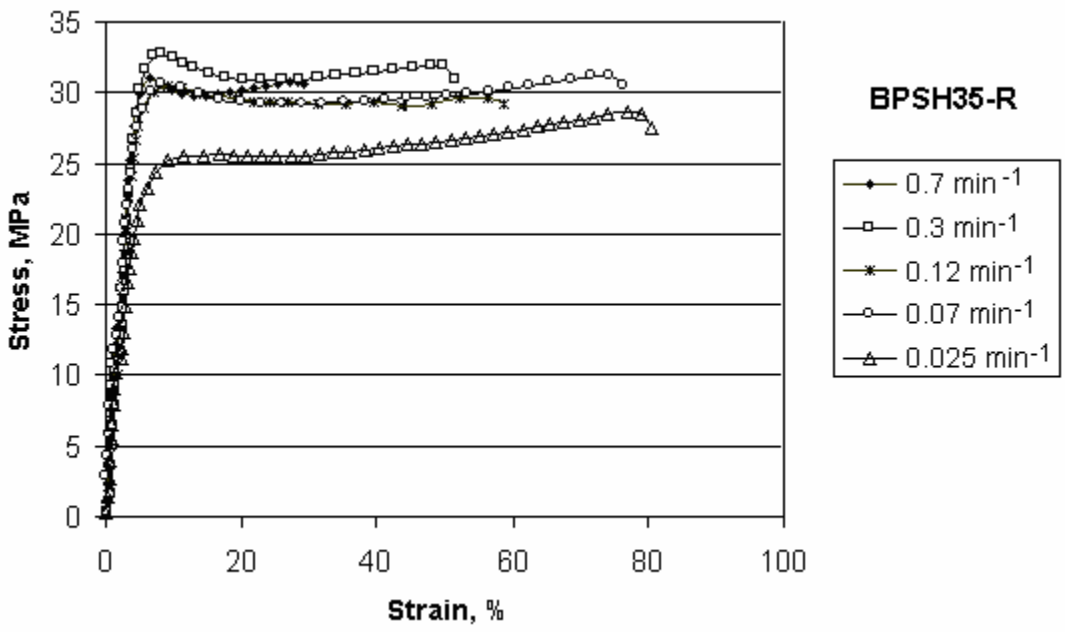

Figure 3-2. Stress-strain curves of BPSH35-R films were measured at different initial strain rates under ambient conditions. Elongation at break was sensitive to initial strain rate.[105] (Permission of reproduction from ACS publications)

Table 3-2. Summary of selected tensile properties of BPSH35-R films at different initial strain rates under ambient conditions [a,b]

Initial strain rate (min^{-1})	Initial Modulus (MPa)	Yield Stress (MPa)	Yield Strain (%)	Ultimate Strength (MPa)	Elongation at Break (%)
0.7	963	31.8	6.7	30.7	29.2
0.3	961	33.6	7.2	31.7	50.7
0.12	826	32.3	7.4	29.2	58.5
0.07	925	31.6	8.6	30.5	76.3
0.025	772	26.7	9.5	27.8	80.2

[a] Samples prepared using the same treatments and tested under the same environment. The average water content was 14.5 ± 3.8%.
[b] No statistical information provided herein due to limited amount of replicates.

3.5.1.2 Counterion Type

The stress-strain curves of N117-H and N117-Na films at the same initial strain rate of 0.3 min^{-1} under ambient conditions are compared in Figure 3-3. It should be noted that similar relative behavior was also observed at the other initial strain rates. Prior to yielding, no significant difference between the initial moduli of these two materials was found, with the N117-Na films

having slightly higher moduli of 265 ± 10 MPa. Beyond yielding, the N117-H and N117-Na stress-strain curves displayed larger deviations in tangent modulus starting at approximately 50% strain. The actual strain values where the deviations started varied with the initial strain rates.

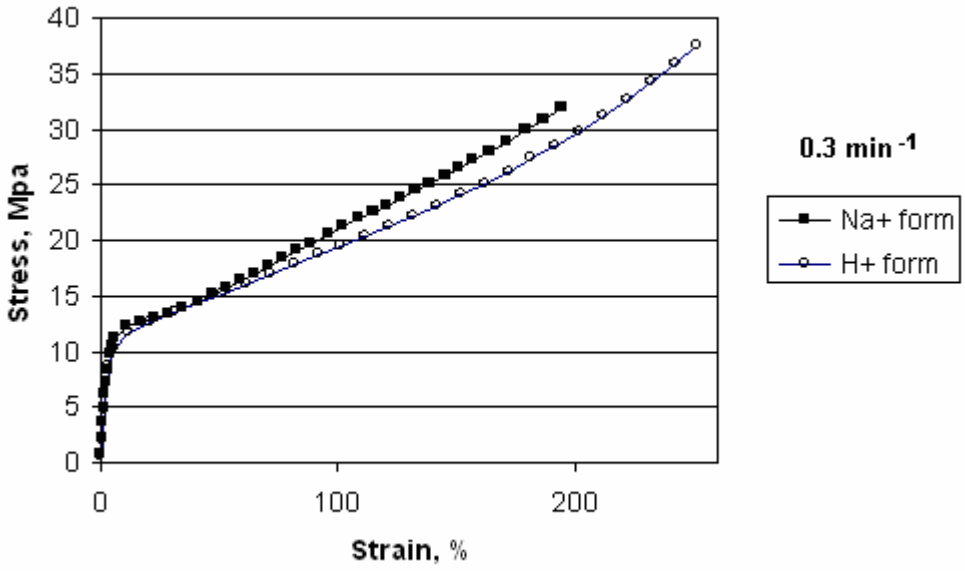

Figure 3-3. The stress-strain curves of N117-H and N117-Na films at an initial strain rate of 0.3 min^{-1} under ambient conditions exhibited deviations at high strains. The water contents of the N117-H and N117-Na sample were 5.4 and 5.1% respectively.

3.5.1.3 The Effects of Molecular Weight

Selected stress-strain curves for BPSH35-MW specimens at an initial strain rate of 0.12 min^{-1} are plotted in Figure 3-4. For each film specimen, the stress-strain curve with the greatest elongation at break was chosen because it best represents the mechanical behavior of the film, (i.e., the specimen did not fail by macroscopic defects). The inset is a magnification of the yielding region of the stress-strain curves. In spite of the variability, the values of the tensile parameters (summarized in Table 3-3) did show some expected trends. With the exception of the yield stress and yield strain, as the sample molecular weight increased, the ultimate strength and elongation at break increased accordingly. Among these parameters, the elongation at break varied the most with molecular weight, changing from approximately 16% for BPSH35-20K to 79% for BPSH35-50K. In particular, the BPSH35-control-70K material exhibited the highest yield point

and ultimate strength. Its elongation at break was not the greatest, but this may be attributable to the solution-casting defects.

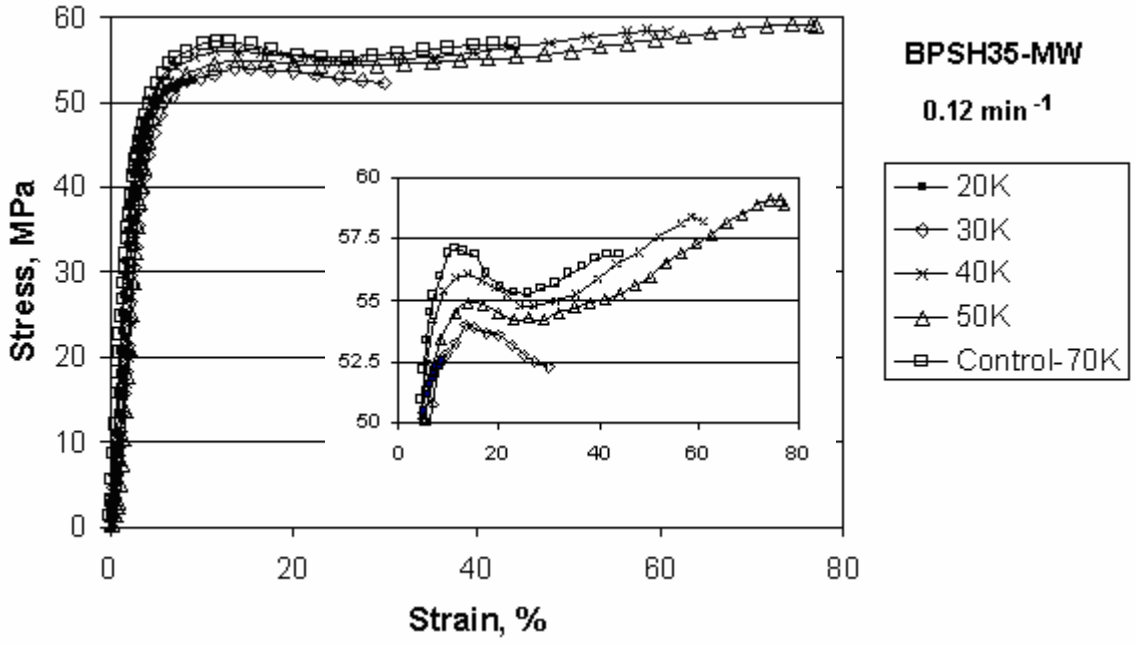

Figure 3-4. Stress-strain curves of BPSH35-MW films were tested at an initial strain rate of 0.12 min^{-1} under ambient conditions. The inset of the high stress region shows variations in yield behavior and elongation. Samples were prepared simultaneously and tested under the same environment.

Table 3-3. The tensile properties of BPSH35-MW specimens at an initial strain rate of 0.12 min^{-1} under ambient conditions [a,b,c]

Mn[a] (g/mol)	Initial Modulus (GPa)	Yield Strain (%)	Yield Stress (MPa)	Strength[b] (MPa)	Elongation at Break (%)[b]
20K	1.46 ± 0.28	3.1 ± 0.38	39.6 ± 7.7	52.0	15.7
30K	1.08 ± 0.23	4.3 ± 0.21	38.0 ± 8.4	52.1	32.3
40K	1.36 ± 0.24	4.8 ± 0.28	47.9 ± 7.7	57.7	63.4
50K	1.53 ± 0.27	4.2 ± 0.69	44.1 ± 10.2	59.0	78.7
Control-70K[c]	1.92 ± 0.30	3.7 ± 0.79	58.1 ± 7.1	66.3	48.8

[a] Mn: Number average molecular weight determined by ^{1}H NMR technique.
[b] For strength and elongation at break data, the values are selected from the longest stress-strain curve for each type of specimen .
[c] Molecular weight determined by comparing the intrinsic viscosities of BPSH35-MW samples. The control-70K samples were synthesized without use of the end-capping process.

3.5.1.4 Inorganic Additives

The reinforcement of the BPSH35-R membranes by the addition of the inorganic additive, zirconium phenylphosphonate (ZrPP, 2%, w/w), is demonstrated in Figure 3-5. The BPSH35-R and BPSH35-ZrPP specimens were tested with an initial strain rate of 0.3 min^{-1} under ambient conditions. The comparisons of stress-strain curves in Figure 3-5 show enhanced tensile properties such as higher initial modulus and better fracture behavior after the addition of ZrPP fillers.

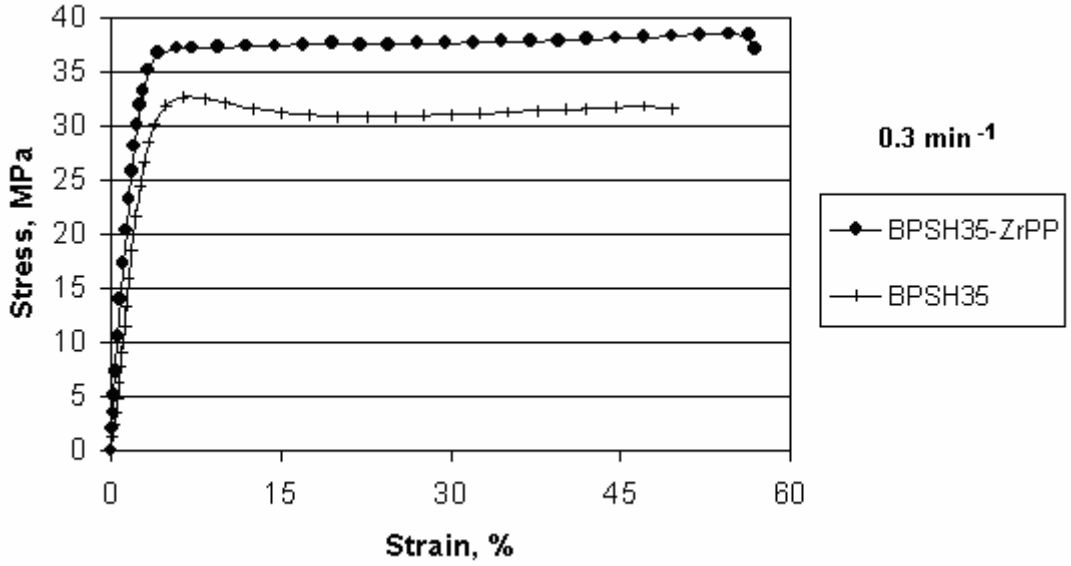

Figure 3-5. Comparisons of stress-strain curves of BPSH35-R and BPSH35-ZrPP (2%) films at a n of 0.3 min^{-1} under ambient conditions show that ZrPP fillers enhance the mechanical properties.

3.5.2 Mechanical Morphology Correlation

The correlation between mechanical properties and PEM morphology provides new insights into the structure-property relationship of ionomer systems. The ionic-cluster model presented by Gierke et al.[83] focused on the arrangements of pedant ionic groups in the ionomer and described the ionomer as a network of ionic clusters connected by channels, as shown in Figure 3-6. A depiction of the ionic-cluster network alone is not able to explain the distinct stress-strain behavior observed for Nafion® and BPSH35 membranes (Figure 3-10). Therefore, it is necessary

to consider the backbone structure of the co-continuous hydrophobic phase, along with its interactions with the ionic-cluster network.

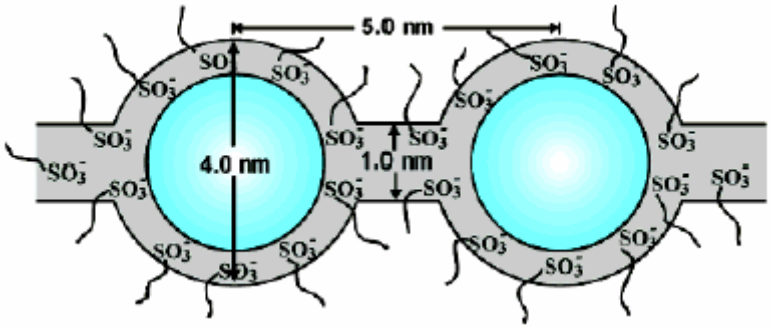

Figure 3-6. Ionic-cluster model for the morphology of Nafion® proposed by Gierke et al.[83] (permission of reproduction from Elsevier)

On the other hand, the elongated polymer aggregates model presented by Rubatat, Gebel and Diat et al. considered the Nafion® structure as an "organization of bundles of elongated aggregates made of more or less aligned and ordered polymeric chains surrounded with the ionic groups and water molecules" (refer to Figure 3-9).[87] They also published data from small angle x-ray scattering (SAXS), small angle neutron scattering (SANS), birefringence, Fourier and real space studies to provide evidences for this model.[86-89] Although the elongated polymer aggregates model emphasize the hydrophobic backbone structure, the details on locations and transport of ionic species as well as water molecules were not given.

Kim, Dong and Hickner et al. investigated the states of water in Nafion® 1135 and BPSH35 membranes using differential scanning calorimetry (DSC) and ^{1}H nuclear magnetic resonance (NMR) T_2 (proton spin-spin relaxation time) techniques.[94] The variations in the appearance of the melting endotherm peak revealed the presence of freezable water in specimens above certain water contents (~ 11% for Nafion 1135, ~ 20% for BPSH40). The shift of glass transition temperature indicated that nonfreezing tightly bound water acts as a plasticizer to the polymer backbone. The loosely bond water not only gives rise to a broader melting peak in DSC thermogram, but to a longer T_2 decay component.

Based upon these studies, we incorporate the concepts of ionic cluster,[83] states of water[94] and proton conduction[90] and propose a three-dimensional "bundle-cluster" model for PEMs as sketched in Figure 3-7. In Figure 3-7 we extrapolate our tensile observations for the "dry" membranes and the schematic of the bundle-cluster model represented the PEMs with intermediate water contents when free water exists in the membrane. The purpose of using intermediate water content as an example is to better illustrate the water molecule distributions and the corresponding proton conduction in PEMs.

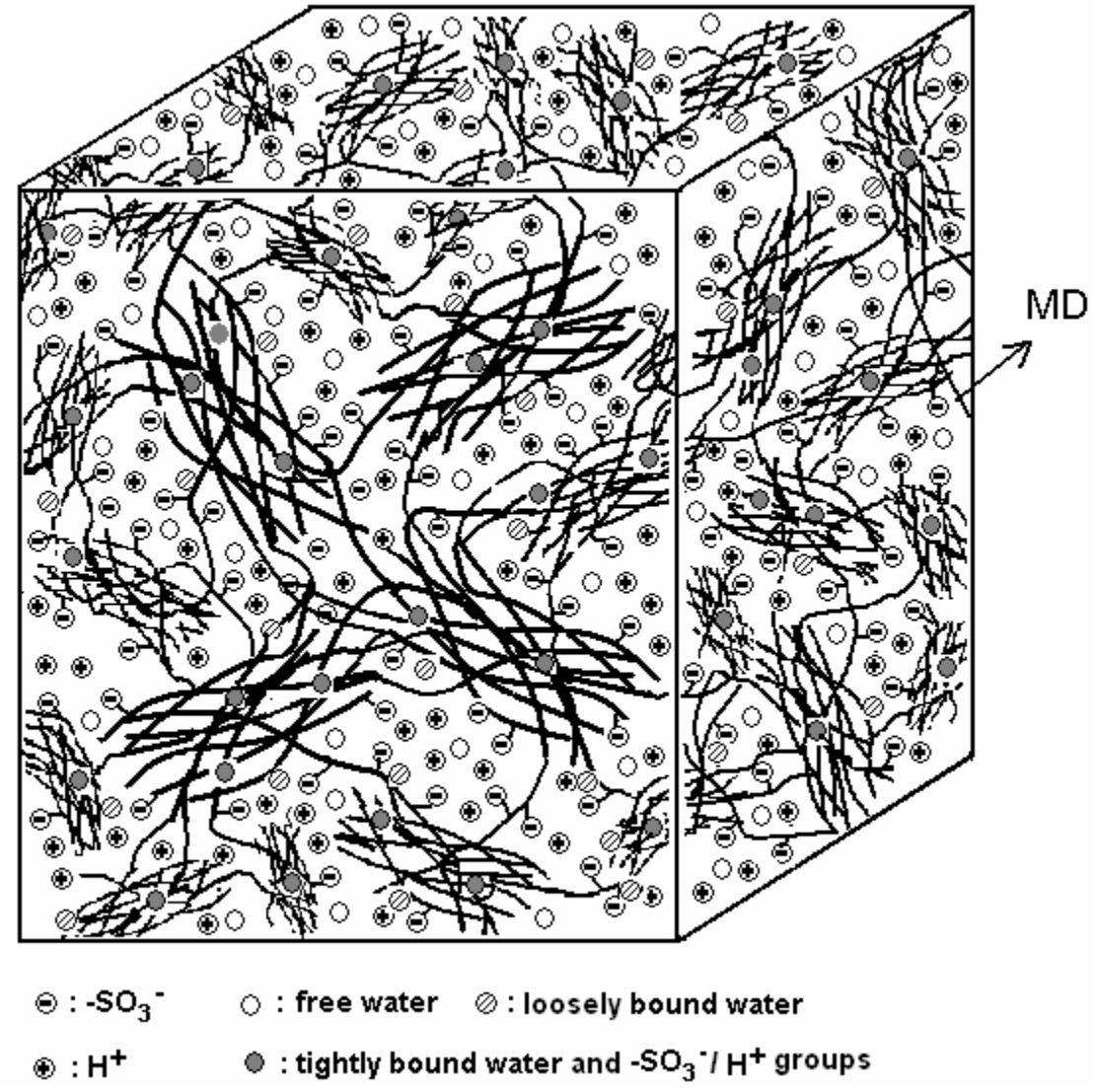

Figure 3-7. A three-dimensional schematic of the proposed "bundle-cluster" model for PEMs at an intermediate water content. The bundles will be more oriented along the MD if the PEMs are

extruded films. The model combines the concepts of elongated polymer aggregated model by Rubatat, Gebel and Diat et al.,[86-89] proton conduction model by K. D. Kreuer[90] and states of water by Kim, Dong and Hickner et al.[94]

3.5.2.1 "Bundle-cluster" Model

In our bundle-cluster model, the hydrophobic phase consists mostly of the bundles of polymer backbone aggregates, similar to that proposed by Rubatat, Gebel and Diat et al.[86-89] The ionic multiplets or clustering of the pendant sulfonic acid groups result in slight separations between the aggregates, which reduce the possibilities of crystallization. For EW 1100 Nafion® whose repeat units are tetrafluoroethylene (TFE) and polar perfluorosulfonic vinyl ether (PSVE), the crystallinity is highly reduced compared to that of Teflon.[91] It is conceivable that 3 to 12% of crystallization occurs between adjacent chain segments where the polar pendant groups are not present. As is well known, processing histories play substantial roles for the polymer morphology. The bundles of aggregates would most likely orient themselves towards the MD if PEMs are extruded. For solution-casting films, the orientation of bundles will be much more random. We believe that the interphase chains connect the bundles of aggregates. Hence a continuous hydrophobic phase can be formed in the ionomer system, which affords the mechanical foundation for withstanding external loads.

Weber and Newman suggested percolation of the Nafion® hydrophilic channels occurs at a minimum water content of $\lambda = 2$.[106] Two to three water molecules per sulfonic acid group ($\lambda = 2-3$) are considered necessary for proton dissociation.[92] When the PEMs are equilibrated under ambient conditions or in the so-called "dry" state, continuous hydrophilic channel structure already exists in the middle of hydrophobic bundles, with mostly tightly and weakly bound water associated with the pendant sulfonic acid groups. There is little free water available, as indicated by the lack of endotherm peaks from the DSC thermograms.[94] The proton conduction mechanism under such circumstances is vehicular,[92] i.e., diffusion of proton and weakly bound water jointly in the form of H_3O^+. As the water content of PEMs reach an intermediate value (e.g. $\lambda = 10$) , free water become present in the hydrophilic channels. Hydrogen bonding is largely developed in this region with free water molecules diffusing through the channels. Free water expands the channels, enhance the dissociation of sulfonic acid

groups and lead to a higher concentration of excess protons along the hydrophilic channels. This will facilitate the transport of protons by structure diffusion at high water contents.[92]

We note that the bundle-cluster model should be applicable for both semi-crystalline and amorphous PEMs. For amorphous materials such as BPSH35 random copolymers, the different structural features rely on the intermolecular distances/interactions between the aromatic backbone, the bundle size and orientations, the distributions of states of water, and the volumetric concentration of ionic groups, etc. However, the underlying morphological structure may be similar to that of Nafion®, as evidenced by their phase-mode atomic force microscopy (AFM) images (Figure 3-8a/8b) and similar water content effects on DSC thermograms with temperatures scanned from -60 to 200°C.[94]

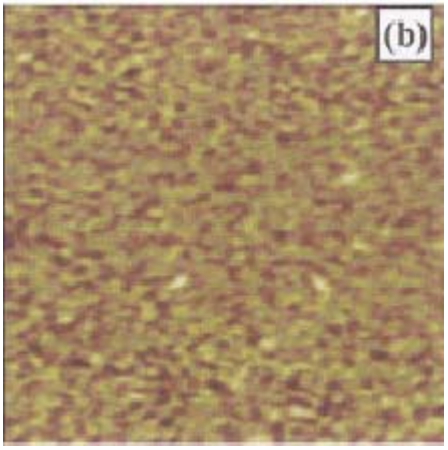

Figure 3-8a. BPSH-35 phase images (b) after method 2, scan size: 500 nm, phase angle: 10°.[95]

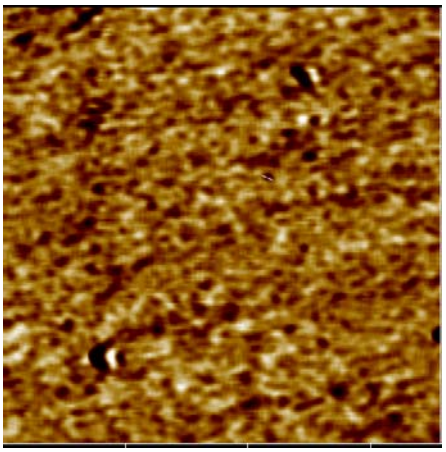

Figure 3-8b. N117-H phase images after method 2, scan size: 400 nm, phase angle: 10°.

3.5.2.2 Substantiation of the Model for the Hydrophobic Phase by Mechanical Testing

For the purpose of investigating PEMFC durability, the knowledge of static morphological model alone is not sufficient to describe the change of PEM mechanical behavior under actual fuel cell operating conditions. The transient motion of the hydrophoblic/hydrophilic phases and ionic species must also be understood. Our research found that as PEMs are stretched under constant strains, their proton conductivities increased first and then decayed with time (further

discussed in a separate publication[107]). In this paper, the speculations with respect to the hydrophobic aggregates/bundle in the bundle-cluster model are examined based on the uniaxial loading and stress relaxation data of the "dry" N117-H and BPSH35-R films. Validating the hydrophilic aspect of the model requires the testing results of membranes under higher water contents, which is the next step of our work and beyond the scope of this paper.

With regard to hydrophobic phase, Rubatat, Gebel and Diat et al. described the possible reactions of polymer bundles in Nafion® subjected to a tensile load. They proposed that when Nafion® films are under tension, at low strains the bundles of aggregates rotate, and then at higher strains the aggregates orient themselves within a bundle (Figure 3-9).[86-89]

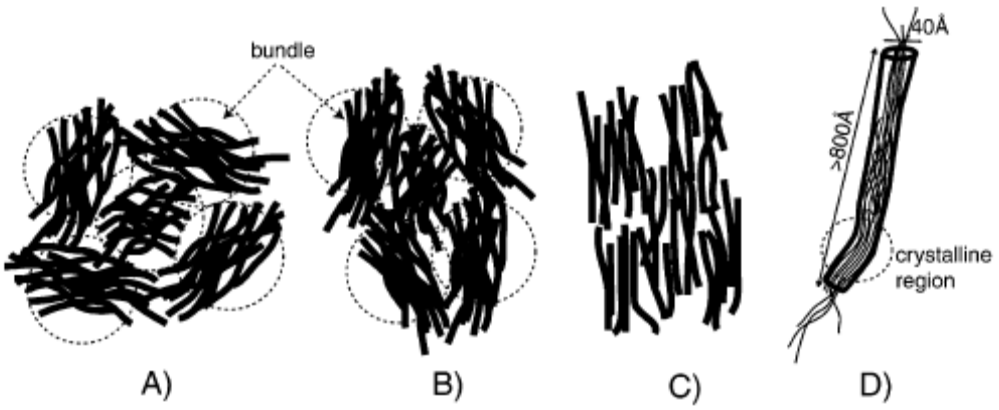

Figure 3-9. The sketch of Nafion® under low and high strains based upon the elongated polymer aggregates model by Rubatat, Gebel and Diat et al.[86-89]

Here we continue developing this speculation and give interpretations for our N117 and BPSH35 stress-strain data. It can be hypothesized that before yielding, the straining process of PEMs is controlled by the rotation of the hydrophobic bundles which act as pseudo-springs that are independent of initial strain rate. Yielding occurs when the polymer backbone chains begin to disentangle. The faster the load is applied, the less time the polymer chains have to relax and change their relative positions. Therefore, less free volume will be generated during stretching in the specimen and the initial stress-strain region can be pushed higher without the onset of disentanglements. At lower initial strain rates, the rotation of bundles lasts longer, producing higher yield strains. After yielding, the polymer aggregates inside a bundle become more and

more disentangled, and thus, are able to be orientated towards the longitudinal direction. To better illustrate above processes, a diagram correlating the stress-strain response and bundle/aggregates reactions is presented in Figure 3-10.

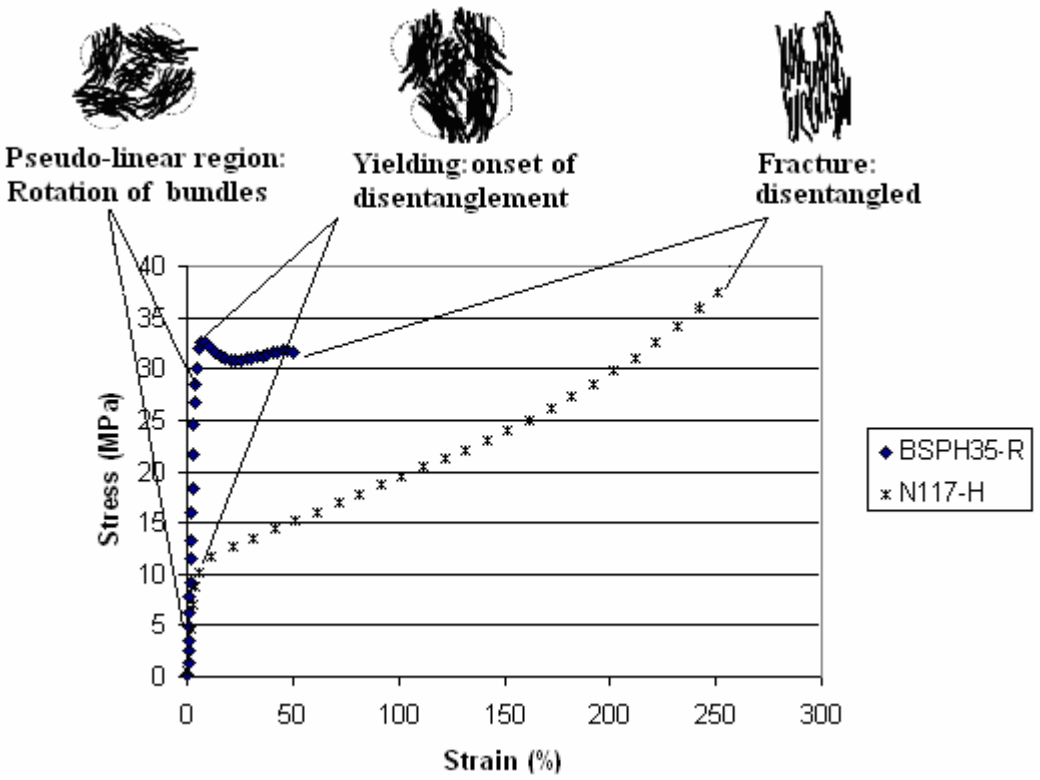

Figure 3-10. A representation of the correlation between the stress-strain behavior of N117-H and BPSH35-R membranes and the possible bundle/aggregates reactions proposed based upon the elongated polymer aggregates model.[89]

Since the backbone chain connections can be weakened by disentanglements, the interactions between the ionic sites should play a more important role in terms of stress-strain behavior beyond yielding. Hence, a more distinct change in the slope of the stress-strain curve should be observed at higher strains provided the counterion type is different. This hypothesis agrees well with the data reported in Ref 81 for the dissimilar stress-strain behavior of Nafion®-Li^+, K^+, Cs^+ and Rb^+ forms. For our N117-H and N117-Na samples (both with ~ 5% water contents), the deviations of the two tangent moduli at higher strains were less than those shown for other counterions.[81] This phenomenon is most likely because the hydronium network in the N117-H

film takes on the same magnitude as the ionic interactions in the N117-Na material in terms of the inter- and intra-bundle connections. The electronegativity, size and solvent affinity of the counterions certainly affect the morphology and performance of the ionic polymer aggregate/ bundle system.

In addition, the augmentation of mechanical properties with increased molecular weight for BPSH35-MW materials can be correlated with polymer chain entanglements. The higher the molecular weight, the more entanglements per chain exist in the ionomer system. The entanglements would very likely be maintained longer during the deformation, improving the large strain properties of the random copolymer. In the case of the ZrPP-reinforced BPSH35-ZrPP films, the strong interactions between the ZrPP fillers and sulfonic acid groups may suppress the hydrophilic channels, form more dispersed hydrophobic/hydrophilic phases, and therefore enhance the mechanical parameters in all aspects.

3.5.3 Stress Relaxation

The stress relaxation behavior of N117-H and BPSH35-R membranes was measured at different strain levels with an initial strain rate of 0.12 min^{-1}. The plots of stress relaxation modulus, $E(t)$ (defined as the stress $\sigma(t)$ divided by the applied constant strain $\hat{\varepsilon}$) versus time, t (in minute) were shifted to obtain the master curves (Figure 3-11 and 12). The logarithmic shift factors $\log a_{\varepsilon}$ were also plotted against the reciprocal of percent nominal strains as insets to Figure 3-11 and 3-12. For both N117-H and BPSH35-R films, the reference strains were chosen as 1%.

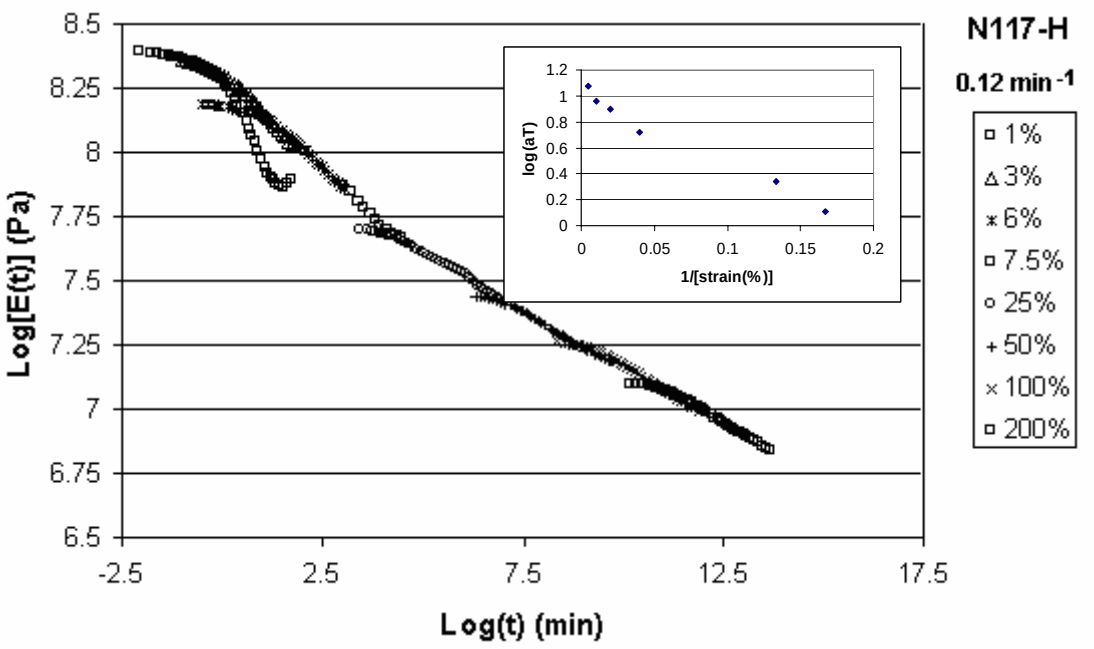

Figure 3-11. Shifted Logarithm plot of stress relaxation modulus $E(t)$ versus time (in min) for N117-H films and $\log a_\varepsilon$ versus 1/[strain(%)] plot.

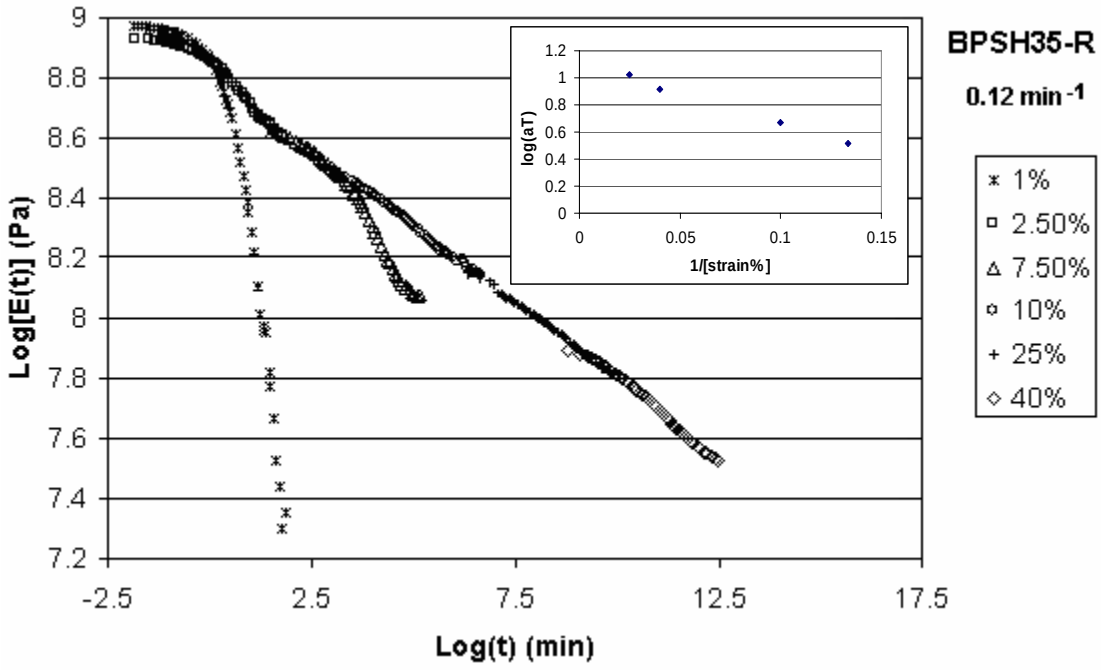

Figure 3-12. Shifted Logarithm plot of stress relaxation modulus $E(t)$ versus time (in min) for BPSH35-R films and $\log a_\varepsilon$ versus 1/[strain(%)] plot.

It is interesting to note that the two master curves appear more reasonable at higher strains where the individual plots of $\log E(t)$ versus $\log t$ are almost linear. At strains lower than the yield strains (N117-H yield strain: 7.6%; BPSH35-R yield strain: 7.3%), there are greater relaxations of the stress relaxation moduli and hence big deviations from the master curves. The deviations cannot be related to the instrument utilized for stress relaxation, since the minimum strain applied was within the sensitivity range of displacement control. However, one possible reason to explain the rapid decay of stress relaxation modulus at low strains may be the softening effect of a small amount of water uptake at the beginning of stress relaxation process. The magnitude of the hygral strain generated in this case was comparable with the nominal mechanical strain, which could deteriorate the accuracy of the load measurement. Obviously, nonlinear viscoelasticity modeling is the best tool to quantify these relaxation processes and define the constitutive relations.

In addition to the stress relaxation modulus – strain master curves, the stress relaxation behavior of N117-H films was studied with respect to initial strain rate under ambient conditions. The strains were kept constant at 3 and 50% strain respectively with initial strain rates of 0.7, 0.3, 0.12, 0.07 and 0.025 min^{-1}. The plots of stress relaxation moduli $E(t)$ against $\log t$ were shown in Figure 3-13 and 3-14. Our bundle-cluster model implies that the presence of nanophase-separated hydrophobic/hydrophilic phase and the partitioning of water and ionic species into these two phases would result in complicated relaxation behavior. The relaxation of backbone chains will be affected and restricted by the ionic interactions among the acidic groups. As mentioned earlier, when the specimens are stretched to levels below yielding, the bundles of polymer aggregates rotate along the longitudinal direction. We speculate that once the loading is terminated and the strain held constant, the movements of interphase chains and the adjustment in the relative positions of the bundles reduce the global stress. On the other hand, when the film is stretched above yielding, the chain aggregates in the bundles will become disentangled and reoriented. At this time the main relaxation mechanism may be copolymer chain disentanglements.

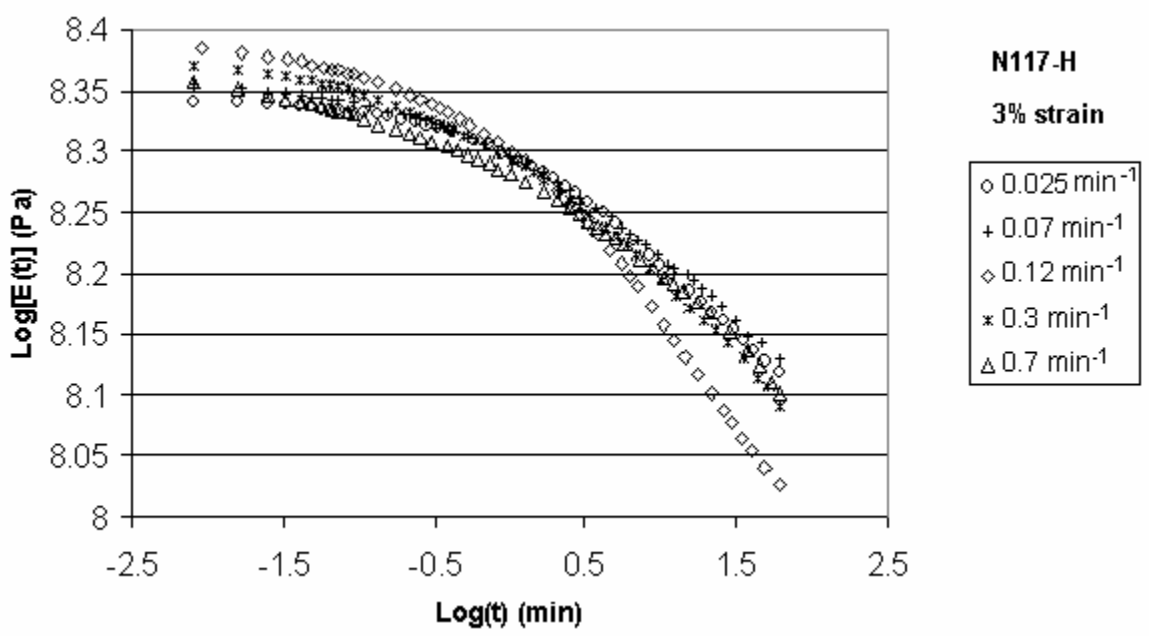

Figure 3-13. Logarithm plot of stress relaxation modulus $E(t)$ vs. time (in min) for N117-H films at 3% strain with different initial strain rates under ambient conditions.

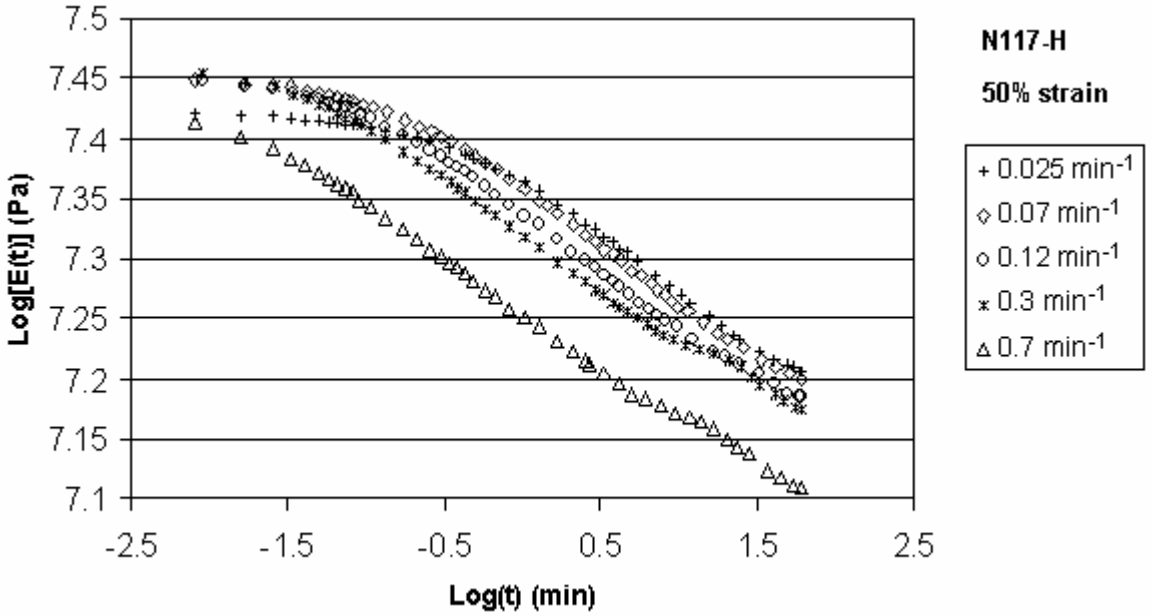

Figure 3-14. Logarithm plot of stress relaxation modulus $E(t)$ vs. time (in min) for N117-H films at 50% strain with different initial strain rates under ambient conditions.

From Figure 3-13, no apparent order can be discerned for N117-H stress relaxation modulus versus time at 3% strain with crossed individual curves. This may suggest that the adjustment of bundles do not depend on the speed of loading after a strain that is smaller than yield strain is applied. This reconciles the uniaxial tensile testing results where the initial moduli of N117-H films were almost constant at different initial strain rates.

Conversely, the plot in Figure 3-14 did show a trend for N117-H stress relaxation at 50% strain with five different initial strain rates. Although the stress relaxation moduli at time approaching zero (i.e. log(t) ~ -2.3) did not follow an ordering from low to high as the initial strain rate increased (probably due to experimental error), the stress relaxation moduli decayed with approximately equal slopes once the relaxation processes reached steadiness. This proves that polymer chain disentanglement is the major relaxation mechanism beyond yielding, which possesses similar time dependences at a single specific strain with different initial strain rates.

3.6 Conclusions

In this paper, the tensile stress-strain properties of N117 and BPSH35 materials were investigated in terms of the effects of initial strain rate, couterion type, molecular weight and inorganic fillers. It was found that the yielding behavior was affected for both N117 and BPSH35-R films. The stress-strain curves of N117-H and N117-Na samples exhibited larger deviations at strains above the yield strain. Increase of molecular weight for BPSH-MW specimens resulted in improved elongation at break. Enhanced mechanical properties were observed for the BPSH35-ZrPP (2%, w/w) composite membrane compared to its matrix BPSH35-R film. The correlation between mechanical behavior and PEM morphology led to the hypothesis of a three-dimensional bundle-cluster model. This model combines the concepts of the elongated polymer aggregates model,[86-89] proton conduction model,[90] as well as consideration of the states of water.[94] It can be utilized to interpret the observed stress-strain phenomena well. The rationale focuses on the bundle rotation before yielding and polymer aggregates disentanglement/reorientation after yielding. In addition, the stress relaxations of N117 and BPSH35 films were measured at different strain levels and different initial strain rates.

Although the relaxations fall into the nonviscoelasticity regime, preliminary morphological explanations based upon the bundle-cluster model were presented.

One method of further validating the “Bundle-Cluster” model would be to perform the tensile tests in wet conditions and compare with the model predictions. The testing results are beyond the scope of this paper and will be reported in ref 107. When the water content of a PEM is higher, one would expect weakened intermolecular/electrostatic interactions in the hydrophobic/ hydrophilic phase due to the plasticizing effect of water molecules, and further development of hydrogen bonding. These would lead to larger diameters of ionic-clusters, more randomly-oriented bundles, swollen channels and decreases in mechanical modulus and strength.[95,107,108,109]

Summarizing, testing and analyzing the mechanical behavior of PEMs will enable improved prediction and understanding of their long-term performance in a fuel cell. The morphological change of PEMs under cyclic, hygro-thermal mechanical loading conditions is a key to characterize the pinhole formation, in conjunction with the proper stress state analysis. It should be kept in mind that morphology also determines the proton conductivity of a PEM, which is an inevitable issue to consider for PEMFC durability modeling.

Chapter 4. Relaxation of Proton Conductivity and Stress in Proton Exchange Membranes under Strain[107]

Dan Liu [1], Michael A. Hickner [2], Scott W. Case [3], John J. Lesko [3]

[1] Macromolecular Science and Engineering, Virginia Polytechnic Institute and State University, Blacksburg, VA 24061, USA

[2] Chemical and Biological Systems Department, Sandia National Laboratories, Albuquerque, NM 87123, USA

[3] Engineering Science and Mechanics, Virginia Polytechnic Institute and State University, Blacksburg, VA 24061, USA

4.1 Abstract

The stress relaxation and proton conductivity of Nafion 117 membrane (N117-H) and sulfonated poly(arylene ether sulfone) random copolymer membrane with 35% sulfonation (BPSH35) in acid forms were investigated under uniaxial loading conditions. The results showed that when the membranes were stretched, their proton conductivities in the direction of the strain initially increased compared to the unstretched films. The absolute increases in proton conductivities were larger at higher temperatures. It was also observed that proton conductivities relaxed exponentially with time at 30^{o}C. In addition, the stress relaxation of N117-H and BPSH35 films under both atmospheric and an immersed (in deionized water) condition was measured. The stresses were found to relax more rapidly than the proton conductivity at the same strains. An explanation for the above phenomena is developed based on speculated changes in the channel connectivity and length of proton conduction pathway in the hydrophilic channels, accompanied by the rotation, reorientation and disentanglements of the polymer chains in the hydrophobic domains.

KEYWORDS: Proton Conductivity, Stress, Relaxation, Proton Exchange Membrane, Activation Energy, Hydrophilic Channel Connectivity

4.2 Attribution

Dan Liu: Performed the proton conductivity and stress relaxation measurements as well as the curve fitting experiment, interpreted the results.
Michael A. Hickner: Helped set up the device for proton conductivity relaxation and provided instructions on using the hinstruments.
Scott W. Case: Advised on the relaxation experiments and guided the writing of the manuscript.
John J. Lesko: Reviewed and guided the writing the manuscript.

4.3 Introduction

Proton conductivity is one of the key parameters for proton exchange membranes (PEMs) in fuel cell applications. It strongly impacts the fuel cell performance in terms of ohmic loss. In the literature, this important membrane property has been reported for different types of PEMs at different temperature and humidity levels.[110-112,95] The common measurement procedure is to equilibrate the membrane in a controlled temperature/humidity environment for a certain period of time and measure the proton conductivity at equilibrium using electrochemical impedance spectroscopy.[111]

Local conditions in an operating fuel cell (liquid water, humidity, stress) may change the conductivity of the membrane and a uniform description of the conductivity (mostly using a constant value) as most models[37,38,46,58] treat this parameter is not applicable. As summarized by Kreuer et al.,[92] the proton conduction mechanisms in a polymer electrolyte are the vehicle mechanism at low water content and structural diffusion at high water content. For PEMs under high humidification conditions as in a fuel cell (i.e. > 13 water molecules per sulfonic acid group), the protons first dissociate from the sulfonic acid groups, form complexes with the solvent water, and then diffuse structurally via hopping through the water molecule hydrogen-bond network. These mechanisms are intimately related to the acidity of the sulfonic groups, the dielectric constant of the water of hydration, and the dispersion of hydrophobic and hydrophilic phases in the PEMs, as suggested by Ref 92. Consequently, PEM morphology that is associated with hydrophoblic/hydrophilic phase separation has a strong influence on the proton conductivity of a membrane.

The morphology of PEMs can be altered by not only temperature and moisture, but mechanical loading.[86-89] We proposed a "bundle-cluster" model in a previous publication to interpret the tensile behavior of PEMs based upon the potential morphological changes under tension.[113] The bundle-cluster model combines the concepts of elongated polymer aggregates, [86-89] proton conduction channels[92] as well as states of water, [94] correlating the stress-strain curves of PEMs with polymer bundle rotation/interphase chain readjustment before yielding and polymer aggregates disentanglements/ reorientation after yielding. This model goes beyond the previous work of Gierke and Hsu ("ionic-cluster" model)[83] in that it includes the hydrophobic domain movements, and that it directly addresses the states of water.

Under fuel cell operation environment, membrane stresses are produced by differential hydrothermal expansion/contraction where the membrane is constrained by bipolar plates and other membrane-electrode-assembly (MEA) components (gas diffusion layers, gaskets, etc.). Cyclic power demand for a fuel cell would result in time-dependent and non-uniform local stresses in the membrane. The corresponding morphological and proton conductivity changes of the membrane will have a considerable effect on the fuel cell durability. For example, if one piece of the membrane has a higher conductivity than its surrounding areas, local heating may occur due to increased current density in this region that may result in membrane thinning and eventually pinhole formation. The heat generated by the direct reaction of hydrogen and oxygen through the pinholes can promote creep to the surrounding membrane, leading to the enlargement of the pinholes. Thus the total fuel cell failure may take place shortly. In spite of its significance, the mechanical strain-induced proton conductivity variation and the corresponding time-dependent behavior in a PEM have not been addressed in the open literature.

In this article, the proton conductivities in Nafion and sulfonated poly(arylene ether sulfone) films subjected to mechanical strains are studied. The relaxations of proton conductivity as functions of time are also presented. Stress relaxation with the same sets of strain values as proton conductivity measurements are provided for membranes under ambient conditions and immersed in water. Underlying morphological interpretations for proton conductivity relaxation are discussed using our bundle-cluster model. Finally, the temperature hysteresis of proton conductivity for Nafion with different equivalent weights is addressed to support the morphological hypothesis with respect to the activation energy of proton conduction.

4.4 Experimental

4.4.1 Materials

Commercial Nafion 117 films (extruded, DuPont, Fuelcellstore.com) were acidified by boiling the films in 0.5 M H_2SO_4 for 2h and then boiling in deionized water for another 2h. After acidification, the Nafion films in acid form (N117-H), were either stored in deionized water at room temperature for conductivity and stress relaxation measurements in water, or dried and flattened overnight in a vacuum oven at ca. 70 ^oC for stress relaxation under ambient conditions. The Nafion 1135 (N1135-H, in acid form, extruded) and Nafion 1035 (NE1035-H, in acid form, extruded) films were kindly supplied by DuPont. Both films were fully immersed in deionized water at room temperature prior to testing.

Sulfonated poly(arylene ether sulfone) random copolymer particles with 35% of sulfonation in their potassium form (BPS35, intrinsic viscosity = 0.66 with N-methyl-2-pyrrolidone (NMP) and LiBr, Mn~40K by ^1H nuclear magnetic resonance (NMR) spectroscopy, Hydrosize Technologies, Inc.) were provided.[96] The particles were cast into a thin film and then acidified using procedures described in ref 113. In a similar manner, acidified BPS35 films (BPSH35) were stored in deionized water for conductivity and stress relaxation measurements. Other pieces were dried and flattened overnight using a vacuum plate at ca. 75 ^oC for stress relaxation tests under ambient conditions. Care (including the use of glass containers and nitrile gloves) was taken during the handling of the specimens to prevent the contamination of the films with other cations.

4.4.2 Measurements

The films were equilibrated under ambient conditions for at least 72h prior to stress relaxation tests in air and ambient relative humidity. For stress relaxation in water at 30 ^oC and the proton conductivity measurements at various temperatures, the films were fully immersed in deionized water for at least 24h before testing. The dry thicknesses of the N117-H, N1135-H and NE1035-H specimens were close to their nominal thicknesses, i.e. 0.178 and 0.089 mm. The BPSH35 specimens were approximately 0.125 mm thick when dried. The equilibrated films (both dry and

immersed) were cut into rectangular specimens with dimensions of 9 mm in width and 110 mm in length. The gauge lengths used for stretching the films along the machine direction (MD) in conductivity and stress relaxation measurements were all set as 55 mm.

4.4.2.1 Proton Conductivity

The proton conductivities of N117-H and BPSH35 films were measured using a Solartron SL 1260 Impedance/Gain-Phase Analyzer between frequencies of 100 kHz to 1 Hz. A stainless-steel screw-driven fixture constructed in house was utilized to stretch the films while they were immersed in deionized water. The widths and thicknesses of the films were recorded after stretching and used to calculate the proton conductivity. A two-point conductivity cell was used to measure the conductivity of the strained film sample, with constant distance between the two electrodes before and after stretching, as sketched in Figure 4-1. The fixture (Figure 4-1) was immersed in deionized water at 30 ^{o}C (the starting temperature). The temperature of the water was managed by a hot plate, thermocouple and temperature PID controller combination.

4.4.2.1.1 Conductivities at a Constant Strain

The conductivities of a N117-H film were studied before and after stretching to a constant strain at different temperatures. First the conductivity of an unstretched N117-H film was measured at 30, 50 and 70 ^{o}C. The same film was then re-equilibrated at 30^{o}C, stretched to 7.5% strain (along MD) and allowed to relax. The conductivity of the stretched film was recorded immediately after stretching and at 1h 45min of relaxation. The water temperature was increased to 50 ^{o}C. The proton conductivities were measured at the moment when the temperature (50 ^{o}C) was stabilized and 1h 45 min after that. The same procedure was applied to the stretched film at 70 ^{o}C.

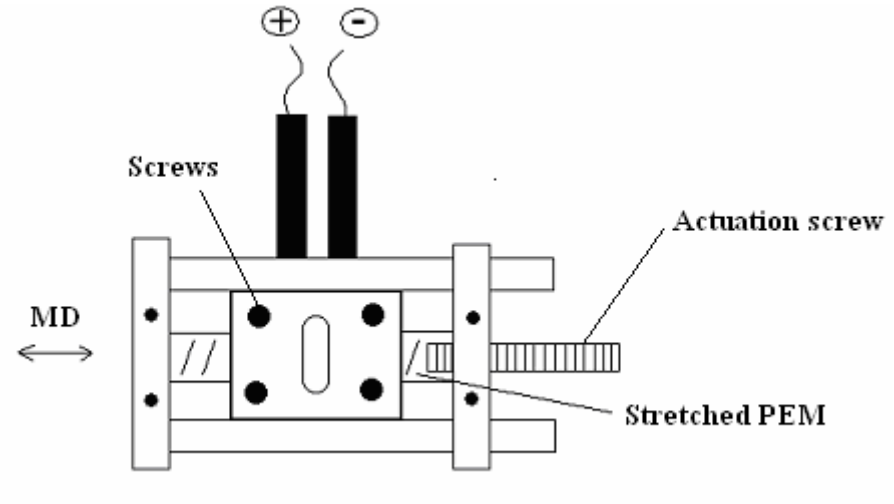

Figure 4-1. A schematic of the screw-driven stainless-steel stretching fixture and the two-point conductivity cell. The whole apparatus was put into deionized water to measure the proton conductivity of the stretched sample at specific strains and temperatures.

4.4.2.1.2 Conductivity Relaxations at Different Strain Levels

The conductivity relaxations of the N117-H and BPSH35 films were examined with respect to different strain levels at 30 ^{o}C. For N117-H samples, 25 and 50% strain were employed while 7.5% and 25% strain were applied to the BPSH35 samples. Smaller strains were used for BPSH35 films because their elongation at break is less than Nafion. The proton conductivity of the stretched sample was monitored for a total of 200 min for each strain.

4.4.2.2 Stress Relaxation

4.4.2.2.1 Ambient Conditions

The stress relaxation tests of N117-H and BPSH35 specimens were performed using an Instron 4468 Universal Testing Machine with a 1 kN load cell under atmospheric conditions ca. 23 ^{o}C and 30% RH. Pneumatic grips (similar to Instron 2712 series pneumatic grips) with elastomeric gripping surfaces were employed to hold the samples in the Instron machine with ~ 200 kPa of pressure. The same group of strain values was chosen for stress relaxation under atmospheric conditions, being consistent with the proton conductivity measurements. The time duration for stress relaxation was 200 min.

4.4.2.2.2 Submerged in Water

A Tytron 250 MTS machine was utilized to carry out the stress relaxation of N117-H and BPSH35 films immersed in deionized water. Customized grips were fabricated to accommodate and stretch the samples in water. The bending moment acted upon the load cell (500N, Model # 661.11B-02, MTS) was minimized by using rigid joints between the horizontal aluminum bars and the stainless steel pendant clamps. The bath temperature was maintained by PID-controlled immersion heaters. Insulation was used on the water tank to prevent excessive heat loss (Figure 4-2). Before tests, the fully immersed N117-H and BPSH35 samples were mounted to the stainless steel grips in water. Once again, after the film specimen was stretched to one specific strain, the stress relaxation data were obtained while the strain was kept constant at 30 ^{o}C. The N117-H samples were measured at strains of 25 and 50% as the BPSH35 samples were measured at 7.5 and 25% strain. Relaxations of each of the stresses at applied strains were recorded for 200 min.

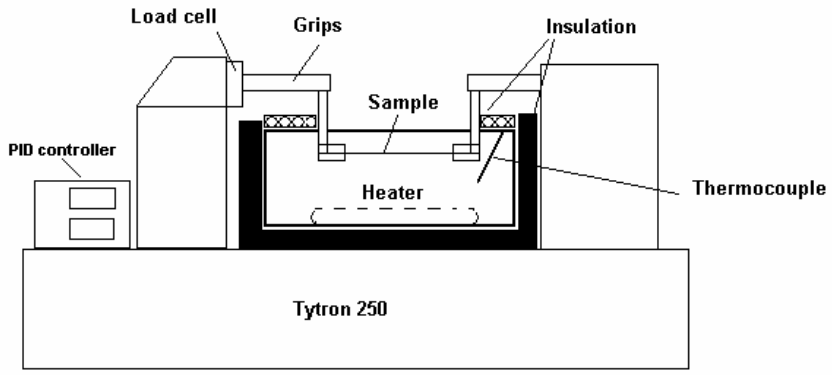

Figure 4-2. A schematic of the set-up for measuring the stress relaxations of N117-H and BPSH35 samples immersed in deionized water.

4.4.2.3 Temperature Hysteresis

The proton conductivities of N1135-H and NE1035-H samples were measured using the same Solartron SL 1260 Impedance/Gain-Phase Analyser with a frequency range 100 kHz to 1 Hz in an unstreched state. The samples were transferred directly from storage in deionized water to the

conductivity cell. The cell was then submerged in water at 30 ^{o}C. The conductivity data were collected for a heating-cooling cycle at temperatures of 30, 50, 70, 80 and 90 ^{o}C, where 90 ^{o}C was the peak temperature from heating to cooling. Target temperatures were reached rather quickly (in less than 2 min) by gently exchanging large amount of hot or cold water with the tank water. The samples were allowed to equilibrate in water at each temperature for 45 min (except 90 ^{o}C), at the end of which the proton conductivity was measured.

4.5 Results and Discussion

Figure 4-3 compares the proton conductivities of the unstretched, stretched (to 7.5% strain), and relaxed (1h 45 min) N117-H film at temperatures of 30, 50 and 70 ^{o}C. When the film was stretched, its proton conductivities increased compared to the unstretched state. The absolute increases in proton conductivities were larger at higher temperatures. It was also observed that the proton conductivities of the stretched N117-H film decreased with time. The higher the temperature, the faster proton conductivity relaxed.

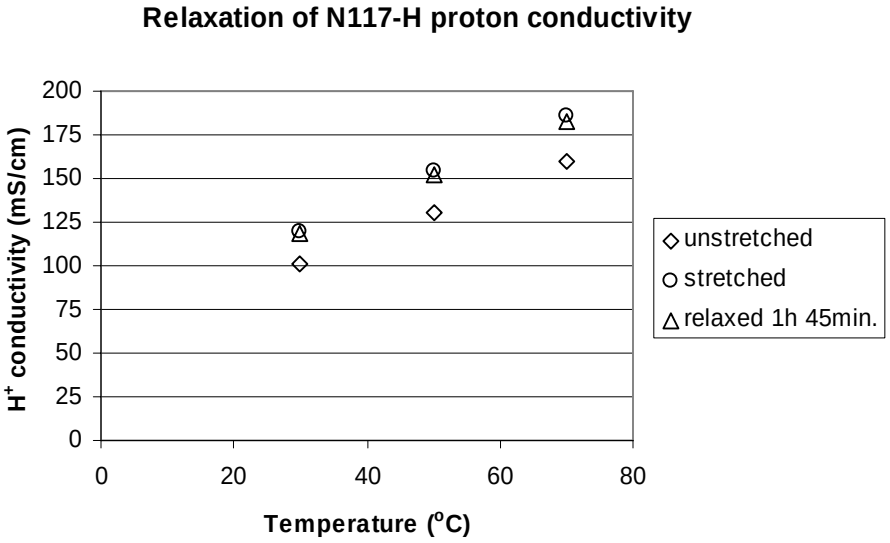

Figure 4-3. The proton conductivity of a N117-H film measured before, immediately after stretching to 7.5% strain and after 1h 45 min relaxation at 30, 50 and 70 ^{o}C

It has been suggested that the proton conductivities of Nafion and BPSH35 membranes follow the Arrhenius type of relationship:

$$\sigma_{con} = \sigma_{con0} \exp(\frac{-E_a}{kT}) \quad \text{- (40)}$$

where σ_{con} is the proton conductivity, E_a is the activation energy for proton conduction, k is Boltzmann's constant and T is the absolute temperature.[114-116] Therefore, the activation energies for proton conduction can be calculated by multiplying the slopes of $\ln\sigma$ versus $1/T$ plots with $-k$, the results of which are listed in Table 4-1 along with the conductivity data.

Table 4-1. Summary of unstretched/stretched/relaxed proton conductivities and their activation energies

	Temp. (^{o}C)	Unstretched	Immediately after stretching	Relaxed after 1h 45 min
Conductivity (mS/cm)	30	101.2	119.4	118.8
	50	130.7	154.1	152.7
	70	159.7	186.1	182.9
Activation Energy (kJ/mol)		9.87	9.62	9.34

Interestingly, the activation energy of proton conduction slightly decreased not only from unstretched state to stretched state, but also from stretched to relaxed state. Since no chemical changes are reasonably expected to occur during the deformation, the decrease in activation energy implies that easier proton movement or better connected hydrophilic domains were achieved during the stretch-relax process due to the rearrangement of polymer chains. Hence, the improvement of proton conductivity for stretched PEM should be elucidated based upon its morphological variations. As suggested by Rubabat, Heijden, Gebel and Diat et al.,[86-89] when a PEM is stretched, the bundles of polymer aggregates would first rotate at low strains and the aggregates themselves begin to disentangle and reorient at higher strains (Figure 4-4).

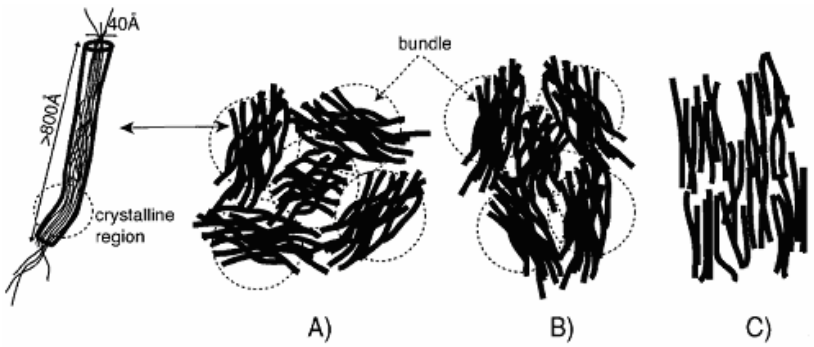

Figure 4-4. The sketching of Nafion under low and high strains based upon the elongated polymer aggregates model by Rubatat, Heijden, Gebel and Diat et al.[87] (permission of reproduction from ACS publications).

We proposed in our "bundle-cluster" model[113] that the boundaries of bundles of polymer aggregates define the main pathway for proton conduction, as the partitioning of water molecules in the PEM hydrophobic/hydrophilic domains facilitates the free water and proton diffusion in the hydrophilic channels (Figure 4-5). The rotation of hydrophobic bundles under small strains leads to a more oriented hydrophilic channel structure along the loading direction, reducing the length of the proton transport path. As a result, the proton conductivity increases, given that the proton dissociation and diffusion coefficients (D_σ) remain the same (the chemical structure of the PEM does not change).

As shown in Table 4-1, increases in proton conductivities were not permanent and decayed with time. The detailed relaxation behavior of proton conductivity under strain was investigated at short intervals (~ 5-30 min). Since it is the movement of hydrophobic domains that give rise to the changes in proton conduction pathways, the global response that is directly related to the copolymer motions, the stress, was also examined under the same conditions.

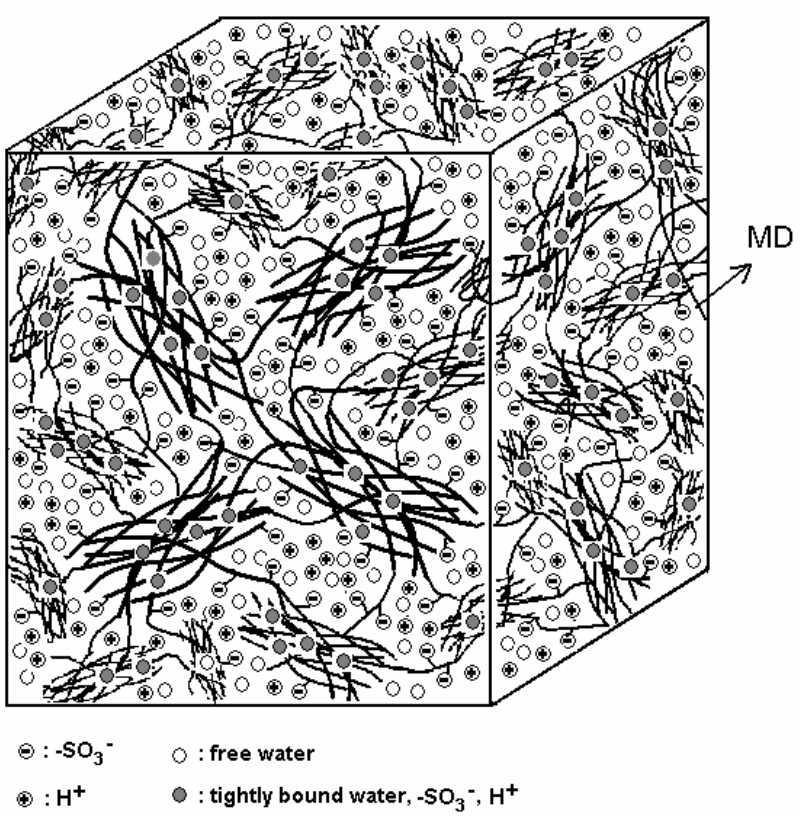

Figure 4-5. A schematic of the proposed bundle-cluster model[113] for PEMs. The boundaries of hydrophobic bundles define the pathway of proton conduction.

Figure 4-6 shows the proton conductivity (30 ^{o}C), stress tested in air (23 ^{o}C) and stress measured in water (30 ^{o}C) of the N117-H film stretched at a 25% strain. It can be seen that the proton conductivity decreased in an exponential form. There was a larger percentage of stress decay in the beginning of relaxation in air than in water. Similar behavior also occurred for the N117-H films at 50% strain and the BPSH35 film at 7.5% strain (Figure 4-7).

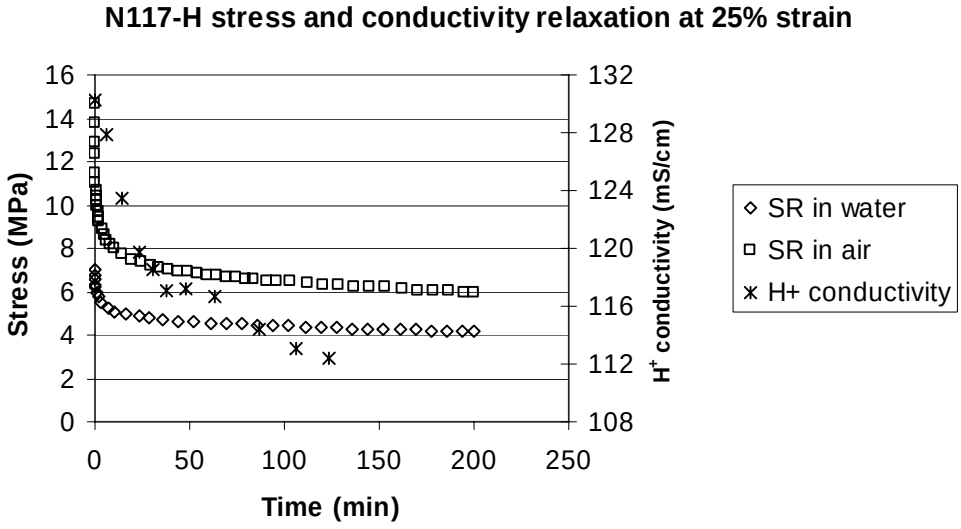

Figure 4-6. Relaxation of proton conductivity and stress of N117-H film at 25% strain, 30 ^{o}C (SR denotes stress relaxation)

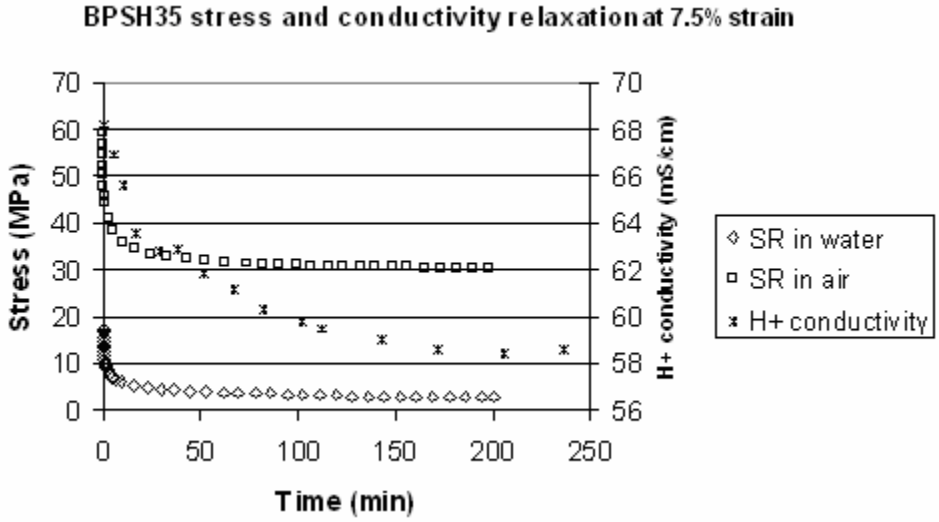

Figure 4-7. Relaxation of proton conductivity and stress of BPSH35 film at 7.5% strain, 30 ^{o}C

The relaxation at 50% strain proceeded more rapidly than that at 25% strain, as expected (Figure 4-8). The previous study of Nafion and BPSH35 films[113] clearly revealed that the stress relaxation behavior of these two PEMs fell into the nonlinear viscoelasticity regime at extremely low strains (<0.5%). Nevertheless, the 3-term Prony Series can give reasonable curve fits to the

stress relaxation and proton conductivity data. The fitting process involved the sum of three exponential terms with their individual "relaxation time" (τ_1, τ_2, τ_3), i.e.:

$$\sigma = \sigma_\infty + \sigma_1 e^{-t/\tau_1} + \sigma_2 e^{-t/\tau_2} + \sigma_3 e^{-t/\tau_3} \qquad \text{- (41)}$$

The fitting results are summarized in Table 4-2.

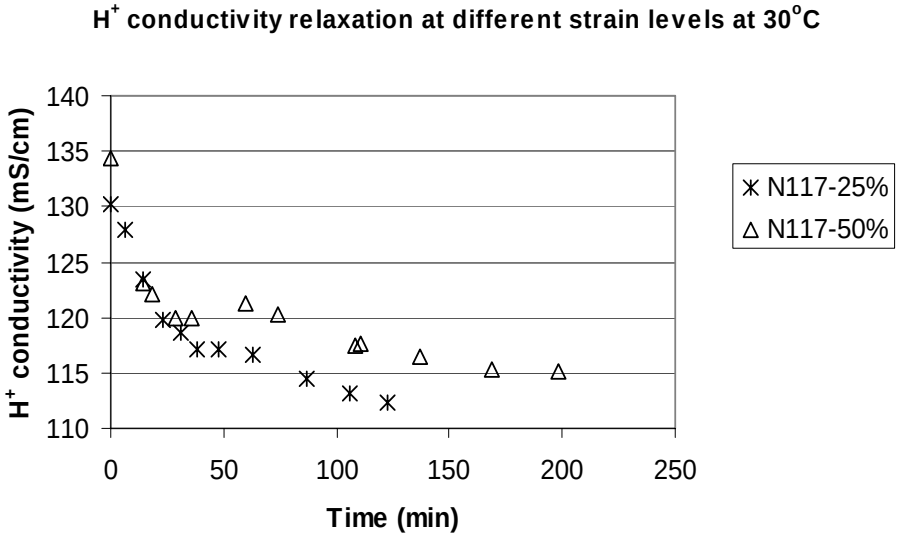

Figure 4-8. Comparisons between relaxations of proton conductivities of N117-H films at 25 and 50% strain, 30 ^{o}C.

Surprisingly, from Table 4-2, the relaxation times followed an ascending order of stress relaxation in air, stress relaxation in water and proton conductivity. To examine this observation, the morphological background of stress and proton conductivity relaxation has to be understood. The hydration isotherm[92] shows the water contents of N117-H films (λ) at 300K and 30% RH and fully immersed in 300K water are approximately 1.8 and 22 water molecules per sulfonate group. Such a big difference would certainly affect its stress relaxation behavior. At room temperature and 30% RH, very few water molecules exist in the membrane. Consequently, the hydrophilic channel structure is minimized and the continuous phase of polymer bundles dominates the stress response when the material is subjected to constant strains. In this case the

stress-strain behavior of the PEM is controlled by its backbone structure. If the strain is smaller than the yield strain, the stress relaxation mechanism is readjustments of the bundles by interphase chain movement. At higher strains, continued chain sliding/disentanglements result in the decay of stress, as suggested in Ref 113.

Table 4-2. Summary of the curve-fitting results for proton conductivity (30 ^{o}C), stress in air (23 ^{o}C), and stress in water (30 ^{o}C) for N117-H film at 25 and 50% strain and BPSH35 film at 7.5% strain[1,2]

Sample	Data[1]	τ_1 (min)	τ_2 (min)	τ_3 (min)	Fitting R-square
N117-H: 25%	H+ conductivity	16.1	138	196	0.9864
	Stress in water	0.68	6.8	98	0.9989
	Stress in air	0.33	5.8	41	0.9998
N117-H: 50%	H+ conductivity[2]	---	51	12183	0.9993
	Stress in water	0.36	9.0	428	0.9990
	Stress in air	0.33	2.8	27	0.9995
BPSH35: 7.5%	H+ conductivity[2]	---	25	4507	0.9930
	Stress in water	0.25	4.7	59	0.9979
	Stress in air[2]	0.21	12	---	0.9930

[1]Curve-fitting process performed using MATLAB 7.0 curve fitting toolbox.
[2]The equation $\sigma = \sigma_\infty + \sigma_1 e^{-t/\tau_1} + \sigma_2 e^{-t/\tau_2}$ gave a better fit.

On the other hand, for a fully immersed membrane such as N117-H, a large quantity of free water expands the hydrophilic channels. Percolation of the ionic clusters occurs under this conditions, since λ is much higher than the percolation threshold ($\lambda = 2$) proposed by Weber and Newman.[106] The plasticizing effect of tightly bound water would reduce the modulus of the fully hydrated membrane. Therefore, the absolute stress decay during the relaxation process was smaller compared to that measured under ambient conditions, resulting longer mathematical relaxation times.

Referring to the proton conduction mechanisms in a PEM with high water content, it is assumed that proton conduction is a combined effect of hydrophilic channel structure, the local acidic concentration and proton hopping. When the PEM is stretched and then held at a constant strain

above the yield strain, the motion of interphase chains and disentanglements of polymer aggregates will initiate the reorganization of nanophase separated domains. It may loosen the hydrophobic aggregates, expand chains into the hydrophilic channels, and hence break up and reconnect some of the hydrophilic channels. As a result, the conduction pathway length that had been previously reduced due to alignment of the hydrophilic channels during the stretching process (decreasing tortuosity, and hence increasing conductivity) is then increased as the chain segment relaxation breaks up some of the domains (decreasing the conductivity). However, the increased channel connectivity lowers the activation energy for proton conduction. This cooperative process takes place at a slower rate than the stress relaxation of polymer chains in the stress relaxation measurements, since the motions of the hydrophobic backbone, pedant ionic groups and water molecules are all related to and restricted by one another. In summary, the ascending order of relaxation times for stress relaxation in air, stress relaxation in water and proton conduction is determined by their underlying morphological evolutions in the hydrophobic/hydrophilic domains. It appears that the more mechanisms the relaxation is involved with, the longer it takes for the system to balance out and reach its final equilibrium.

In addition to the relationship between the hydrophilic channel connectivity and the activation energy of proton conduction, the temperature hysteresis of N1135-H and NE1035-H conductivity was explored (Figure 4-9 and Figure 4-10) to study the influences of thermal energy on the activation energy of proton conduction. The proton conductivities were measured at 45 min after the designated temperature was first reached. Alberti, Casciola and Massinelli et al.[112] performed similar type of tests for N117 membranes at 34 and 50% RH with temperature cycling in the range of 100 to 160 ^{o}C. Higher proton conductivities were observed for the heating cycle and the increases in proton conductivity were attributed to irreversible crystallization of the membrane at elevated temperatures.

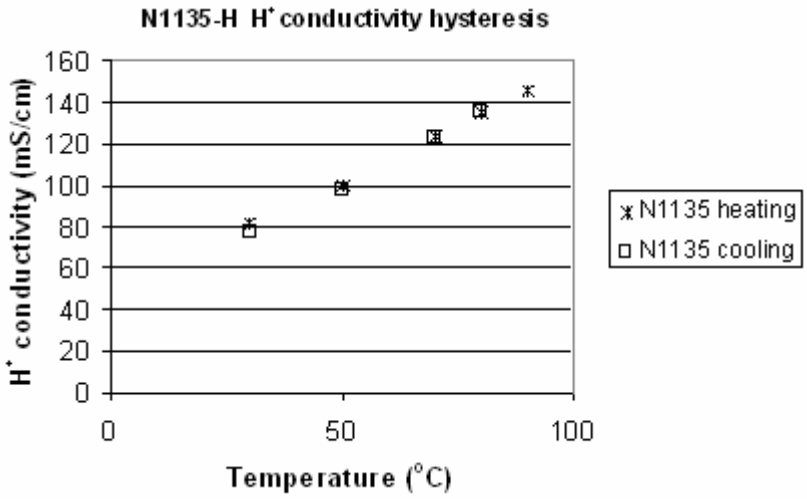

Figure 4-9. Temperature hysteresis of proton conductivity of N1135-H film.

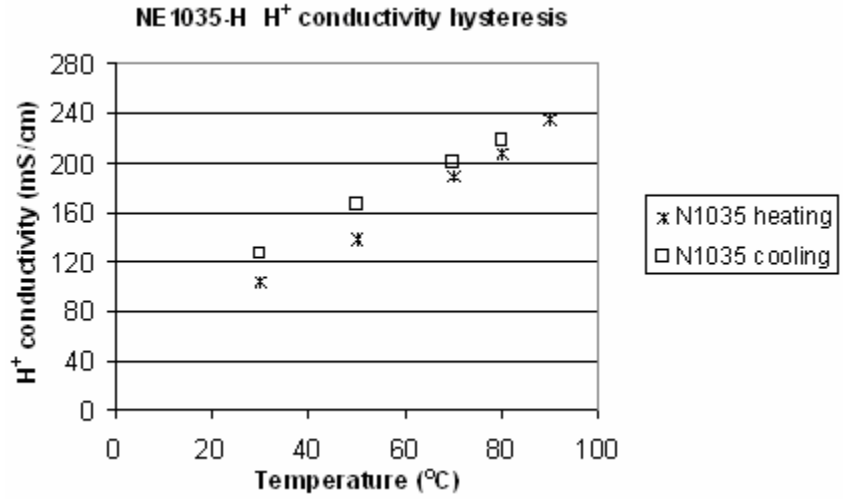

Figure 4-10. Temperature hysteresis of proton conductivity of NE1035-H film.

In our case, the films were fully immersed in liquid water and the employed temperature range was below the N1135-H crystallization temperatures (120~230 ^{o}C)[117]. The N1035-H film may not be crystallizable because of its high ionic concentration. It was found that more pronounced hysteresis existed for NE1035-H films, the equivalent weight of which was lower than that of N1135-H specimen. The activation energies of proton conduction were calculated for N1135-H and NE1035-H films as 8.98 and 12.6 kJ/mol respectively upon heating and 10.1 and 9.53

kJ/mol upon cooling. There was a significant activation energy decrease seen for NE1035-H film for the cooling cycle, in contrast to slight increase of activation energy for N1135-H. It may be speculated that there are a larger fraction of acid groups dispersed in the hydrophobic domains in NE1035-H film because of its higher acid content. When the NE1035-H film is heated in water, structural evolutions occur which may drag the previously excluded acid groups into the hydrophilic domain, giving rise to even higher local acid concentrations. The higher concentrations of acid groups as well as water molecules would very likely be maintained because it is thermodynamically unfavorable for the formerly dispersed acid groups to reenter the hydrophobic phase. Therefore, the proton conductivities of the NE1035-H film increased during the cooling cycle, with a considerable decrease in activation energy for proton conduction. We emphasize, however, that this is speculation consistent with our experimental results, but has not been directly validated.

4.6 Conclusions

In this article, the relaxation of proton conductivity and stress of N117-H membranes under ambient conditions and immersed in water were measured at a constant strain at temperatures of 30, 50 and 70 ^{o}C and different strain levels at 30 ^{o}C. The proton conductivities of the stretched film increased compared to those at the unstretched state. Detailed relaxation experiments revealed that proton conductivities relaxed exponentially with time under strain. The stresses of N117-H film relaxed faster in air and in water than proton conductivity. The speculation for above phenomena may be related to the combination effects of bundle rotation/aggregates disentanglements and the hydrophilic channel connectivity/reorientation. Similar trends were also found for BPSH35 materials. The NE1035-H membrane exhibited more pronounced proton conductivity hysteresis. Larger swelling irreversibility of NE1035-H film was assigned as the reason. When modeling the change of PEMFC performance as function of time, the information obtained thus far would be valuable to define the constitutive relations.

Chapter 5. Durability Study of Proton Exchange Membrane Fuel Cells under Simulated Driving Conditions with Cyclic Current Profile

Dan Liu [1], Scott W. Case [2]

[1] Macromolecular Science and Engineering, Virginia Polytechnic Institute and State University, Blacksburg, VA 24061, USA

[2] Engineering Science and Mechanics, Virginia Polytechnic Institute and State University, Blacksburg, VA 24061, USA

5.1 Abstract

This work addresses issues of long-term durability of hydrogen-air proton exchange membrane fuel cells (PEMFCs) under cyclic current loading conditions, simulating the real road driving conditions for automotives. The same type of membrane-electrode-assembly (MEA) was also aged under constant current mode as a control and the results were compared with those of the cyclically aged MEA. Both MEAs were characterized by cell polarizations, impedance spectra, Tafel plots, hydrogen crossover rates as well as electrochemical active surface areas at intervals of 100h of aging. It was demonstrated that hydrogen crossover increased dramatically after 500h of current cycling due to pinhole formation and was the most dominant degradation source. The fuel cell approached the end of its useful lifetime after 1000h of operation. On the other hand, the hydrogen crossover rate remained approximately constant for the MEA under constant current operation. Mass transport limitations were identified as the major source of decreased performance during the constant current operation. This decrease in performance was partially reversible when cathode flooding was resolved by setting the cell at lower current densities. At the end, a phenomenological durability model was established successfully to describe the aging processes and cell performance at different time nodes.

Key words: Proton Exchange Membrane Fuel Cell, Durability, Cyclic Current Mode, Aging Diagnosis, Hydrogen Crossover, Mass Transport Limitation, Phenomenological Modeling

5.2 Attribution

Dan Liu: Performed the long-term durability tests and end-of-period diagnosis of MEAs under cyclic and constant aging mode, established the durability phenomenological model.
Scott W. Case: Advised on the aging experiments and guided the writing of the manuscript.

5.3 Introduction

Durability studies of proton exchange membrane fuel cells (PEMFCs) have attracted enormous attention for the last three years. A great deal of research effort has been devoted to meeting the Department of Energy (DOE) targets, such as 5,000h of operational lifetime for PEMFC stacks in automotive applications.[79] There are two stages associated with the durability studies of PEMFCs. In the first stage, the degradation sources and mechanisms of PEMFC components/system are identified, with respect to different system configurations, various material selections, and different operation conditions. Experimental observations are conducted to characterize the aging phenomena as functions of time. In the second stage, mathematical models are developed to predict the degradations in a PEMFC system, in which expressions of the aging phenomena and aging effects are incorporated into performance models through constitutive relations. For the durability model to achieve good accuracy and maximum predictive power, multi-dimensional microscopic modeling based on the classic conservation laws is required, leading to great complexity. As an intermediate step, a phenomenological model with values of aging parameters substituted into the semi-empirical fuel cell performance equations at different time nodes can be employed to begin the durability modeling process. But in the literature, the durability study of PEMFCs remains in the first stage, with mostly experimental characterizations presented.[71]

As is known, the operation conditions associated with PEMFCs include a strong acidic environment (pH~2), oxygen in gaseous phase and dissolved phase, water in vapor and liquid

phase, tensile/compressive stresses, contamination, cyclic temperature and dynamic load cycles. The associated aging processes may occur in the polymer membrane, catalyst layers, electrodes, membrane-catalyst interface, monopolar/ bipolar plates, sealing materials and current collectors. Reference 71 provides a nice summary of the reported degradation sources from PEMFC components. Long-term aging studies were also conducted to investigate the effects of operation conditions on fuel cell durability.[71,118-120]

St-Pierre, Wilkinson and co-workers at Ballard Power Systems performed a series of aging tests for PEMFC stacks (primarily MK5 and MK513 stacks) under different operating conditions.[120] The effects of water management with high and low humidification levels, contamination, pressure, temperature and reactant stoichiometry were inspected with the introduction of possible mitigating strategies. They concluded that poor water management could cause PEMFC performance degradation due to mass transport limitations. Counterflow patterns in the bipolar plates, temperature gradients, changes in substrate hydrophobicity and load cycling were examined to help reduce the mass transport issues. In addition, the influence of freeze-thaw cycles was examined. These cycles showed insignificant degradations in PEMFC performance after 55 cycles.

Recently, Xie, Wood, and Wayne et al. carried out a long-term durability study of hydrogen-air PEM fuel cells. Two types of MEAs were investigated under constant current mode with different current settings and high humidity level for 2000h.[121] Characterizations of the aged MEAs were performed periodically, including voltage decay, polarization, electrochemical active surface (EAS) area, and fluoride ion and catalyst metallic concentration in cathode exhaust water. The result revealed that one type of metal particles in the catalyst alloy migrated from cathode to anode during the aging process, reducing the EAS area. Scanning and transmission electron images of MEA cross-sections after aging showed the loss of carbon-supported catalyst clusters and possible dissolution of recast Nafion ionomer. Fluoride and sulfate anions were detected in the cathode outlet water by high performance liquid chromatography (HPLC) - mass spectrometry (MS) technique, proving the degradation/ dissolution of ionomers.

The paper by Xie, Wood, and Wayne et al. presented a comprehensive list of characterizations for PEMFCs after aging. Nevertheless, they inspected the MEA performances under constant current mode, which is different from the real road driving scenario. The degradations of cell components may vary with respect to the current/power output spectrum. Wilkinson and St-Pierre examined the dynamic operation of 8-cell and 20-cell PEMFC stacks with modified urban transit authority (UMTA) driving cycles.[71] Small performance degradation was demonstrated for these stacks over 5000h; most of the performance loss was found to be reversible. They did not provide detailed diagnosis for sources of the degradation in their report. Neither were the impacts of urban driving cycles on the PEMFC material and system deterioration identified.

In this article, the aging mechanisms of the same type of commercially available hydrogen-air MEAs were characterized under cyclic and constant current loading conditions. Both MEAs were aged for 1000h in total and diagnosed every 100h of operation. A semi-empirical phenomenological model was set up to incorporate the observed aging phenomena and describes the cell performance at different aging times. Distinct degradation mechanisms were illustrated after comparing the results under two different aging modes. These results reinforce the need to conduct systematic inspections of PEMFCs to identify the causes of changes in the cell's long-term performance, which are related to the aging behavior of materials, structure, hardware design and operation conditions. They also point to the need for the establishment of standard PEMFC aging protocols.

5.4 Experimental

5.4.1 Materials

Two 5 cm^2 standard hydrogen/Air MEAs were purchased (fuelcellstore.com, 5L HP-A MEA, item # 590514). The catalyst loadings of both anode and cathode were 0.5 mg/cm^2. Acidified Nafion 112 film was employed as the membrane and ETEK ELAT® carbon cloth was applied as the gas diffusion layers (GDL). The MEAs were tested as-received using Fuel Cell Technologies Inc. (FCT) fuel cell test stations. Standard 5 cm^2 PEMFC fixtures were obtained from FCT, with stainless steel monopolar plates and gold-coated copper current collector plates. The ultrapure

hydrogen gas (Airgas, UHP-300) cylinder and breathing air (Airgas, Air-300) cylinder were attached to the FCT stations to supply fuel and oxidant for fuel cell operations. Ultrapure nitrogen gas (Air, UPN-300) was utilized for electrochemical measurements.

5.4.2 Measurements

5.4.2.1 Aging Mode

There were two aging modes applied for the aging processes.

Cyclic current aging

The cyclic current spectrum was provided as a preliminary cycling profile for durability testing of PEM fuel cells. One of the two MEAs, denoted as MEA1, was aged by use of this cyclic current profile for a total of 1000h. Each current aging cycle composed of 16 steps including open circuit, low current settings, intermediate current settings and the highest current setting, the details of which are shown in Table 1. One cycle took approximately 6 min to complete. The MEA1 was aged for 10 aging periods, with 1000 cycles or 100h per period and characterized for a full set of performance and component parameters after each 100h aging period. The MEA1 operation was performed at a cell temperature of 80 ^{o}C, anode/cathode temperatures of 80 ^{o}C and anode/cathode preheater temperature of 81 ^{o}C. Both gas lines were fully-humidified. The hydrogen flow rate was 200 standard cubic centimeters per minute (sccm) while the air flow rate was 500 sccm. Both electrodes had a backpressure of 138 kPa (20 psi). The MEA1 was tested using an FCT test station with an EMREL-50A-100W electronic box (denoted as test station #1).

Table 1 describes the test protocol to assess the performance and durability of fuel cells for automotive propulsion applications. The goal of this testing is to assess cell and stack performance against DOE targets. This protocol is proposed by an automotive company but not intended to be comprehensive as there are many issues critical to a vehicular fuel cell (e.g., start/stop). It should be recognized that the cycles specified herein have not been fully validated and correlated with data from systems operated under actual drive cycles. Therefore, durability

results from this protocol may not be predictive of lifetime in an actual fuel cell vehicle subjected to actual driving and start/stop cycles.

Table 5-1. The Current cycling profile

Step	Duration sec	Current Density (A/cm^2)		Step	Duration sec	Current Density (A/cm^2)
1	15	0		9	20	0.4
2	25	0.2		10	15	0.05
3	20	0.4		11	35	0.2
4	15	0.05		12	20	1.06
5	24	0.2		13	35	0.86
6	20	0.4		14	8	0.02
7	15	0.05		15	35	0.4
8	25	0.2		16	40	0.05

Constant current aging

The constant current aging was conducted on MEA2 at the highest current setting from the cyclic aging spectrum (1.06 A/cm^2). For the purpose of control, all operation conditions were kept the same as those of cyclic aging. An FCT test station (EMREL-10A-60W load box, other features are the same as or comparable to that used for MEA1) was utilized for MEA2 operation and characterizations. (This test station is denoted as test station #2.)

5.4.2.2 End-of-Period Diagnosis

The same end-of-period diagnosis procedures were executed for both MEAs. Following the 100h aging periods, cell operation was halted and the cell polarization, impedance, Tafel plot, H_2 crossover rate and cyclic voltammetry (CV) were evaluated. Aging for the next 100h period resumed after all characterizations were finished on the next day.

Lifetime

To maintain the desired current profile while collecting the lifetime data, a cyclic current step protocol was written to control the load box settings and output. This protocol was based on the Set Protocol.vi from the FCT test station software library, in which users can specify the current settings of the load box under constant current mode, as well as the time delay for each of the current setting after the specification has been reached. At the same time, voltage, current, gas flow rates and temperatures of the running MEA were monitored and recorded via an independent Labview file (Alone LT.vi from the software library) with a sampling rate of 120 point/h. For the constant current aging mode, current was simply adjusted to the set point while the lifetime test was running. In both cases, the aging data collection began when the MEA was re-heated for the next aging period and then lasted 100h covering the whole aging period. In particular, open circuit voltages (OCV) and voltages at specified current densities were collected and compared at the beginning and end of each aging period.

Cell polarization

The cell polarizations were examined in both ascending and descending current control modes shortly after the aging period was ended. The current density range was between 0 and 1.3 A/cm^2, with a delay of 30 seconds at each current setting. Before each of the polarization measurements, a shunt calibration was performed. The shunt resistances were approximately 5.00×10^{-3} ohm for test station #1 and 1.53×10^{-2} ohm for test station #2. High frequency resistances of the cell were measured at all stepwise current levels when polarization data were being taken. Beside that, the independent high frequency resistance control panel (HFR.vi) was executed to validate the resistance of the cell (evaluated by polarization experiments) with a signal magnitude of 7.00×10^{-2} A and frequency of 6000 Hz.

Impedance test

Cell impedance tests were implemented using an FCT in-box AC-impedance system at three different current density levels, 0.17, 0.64 and 1.10 A/cm^2 - representing the kinetic, ohmic and mass transport region of a PEM fuel cell polarization curve. Sinusoidal current waves were emitted through the cell and shunt, with a frequency range of 10000 to 0.1 Hz. The magnitude of current wave was also 7.00×10^{-2} A. By examining the voltage drop over the shunt, the complex resistance of the fuel cell electrodes (especially cathode) can be calculated. The Nyquist plots,

which are plots of the imaginary resistance versus the real resistance, were generated by the software. From these plots, the values of resistances and capacitances in the PEMFC electrodes (see the equivalent circuit in Figure 5-1) R_1, R_2 and C_p were determined.

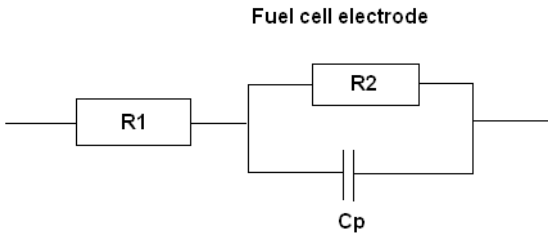

Figure 5-1. Schematic of the PEM fuel cell electrode equivalent circuit[122]

Tafel Plot

The Tafel plots of MEA1 and MEA2 were obtained in potientiodynamic mode by a Solartron Analytical 1480 multistat. Channel 1 of the multistat was connected to the positive (red) and negative (black) leads of the fuel cells, with the H_2 electrode acting as both the counter and reference electrodes. The potential of the fuel cell was controlled by the multistat to decrease from OCV to the potential where the current density reached 0.2 A/cm^2 continuously with a rate of 1 mV/sec. A sampling rate of 100 point/sec was applied. When making the Tafel plot of voltage vs. log(current density), the potential of the cell was compensated for by adding the product of current and high frequency resistance. The mass transport corrections for cell potential were not performed. The Tafel test was repeated two times to ensure reproducibility.

Hydrogen crossover

The hydrogen crossover rate is an important parameter for determining the permeability of membrane in a fuel cell. If the hydrogen crossover rate from the anode to cathode increases dramatically, it is usually assumed that macroscopic pinholes have formed in the membrane. This would give an indication that the fuel cell is at the end of its useful lifetime. When measuring the hydrogen crossover rate, the cathode gas flow was switched from air to ultrapure nitrogen, with a flow rate of 200 sccm and still having a back pressure of 138 kPa (20 psi). The anode hydrogen flow remained 200 sccm and 138 kPa (20 psi) back pressure. After 40 minutes

of gas equilibration, a potentiostatic assessment at 0.8 V was conducted to measure the current through the fuel cell at 1 point/second for 5 minutes. The measured current corresponds to the oxidation of the hydrogen molecules at the cathode side in the presence of platinum catalysts. The anode was taken as the counter/reference electrode, whereas the nitrogen-flowing cathode served as the working electrode. A total of three tests were performed for each end-of-period diagnosis, with the average values recorded.

Electrochemical active surface

The evaluation of EAS area was conducted the morning after the hydrogen crossover tests were completed and after the test station was shut down overnight (with the fuel cell connected to the station). The fuel cell fixture had sat for approximately 12h and cooled to room temperature. There are two reasons for this test procedure: (1) to try to eliminate the adverse effect of hydrogen crossover on CV experiments at high temperatures; and (2) to simulate the overnight parking of a passenger vehicle. The EAS areas of both the anode and cathode were estimated by use of a three-cycle-triangle CV. The cathode EAS was first measured by purging H_2 through the anode line (reference/counter electrode) and N_2 through the cathode line (working electrode) with 200 sccm of gas flow and no backpressure for 35 min. After three cathode CV tests were taken, the extension tubing was employed to change the flow path, with 200 sccm of H_2 flowing through cathode and N_2 flowing through anode. In this case, the counter/reference-working electrodes were switched within the fuel cell. Therefore the leads connecting to the multistat were re-wired, with the black anode lead from the fuel cell joining the red working electrode lead from the multistat. Once again the gases were allowed to flow for 35 min before the CV experiment was started and repeated two times. After anode and cathode CV, both electrodes were purged with N_2 at 200 sccm with zero backpressure for 35 min. By doing so, the CV baselines were obtained and the hydrogen gas left on the cathode when performing the anode CV was able to be discharged, which greatly reduced the chance of cathode catalyst evolution due to the intermediates from the electrochemical reaction of air and residual hydrogen molecules. Then the next aging period was started.

Fluoride ion concentration/pH measurements

In order to examine the degree of chemical degradation in the ionomer, the fluoride ion concentrations and the pH values of cathode outlet water were evaluated. The cathode water was collected into an environmental sampling glass jar (pre-cleaned, cap with PTFE lining, VWR.com) during the last 48h (cyclic) or 12h (constant) of the aging period, when the cathode venting system was believed to be flushed thoroughly from the previous operation. The jars were washed again before use by deionized water and then isopropyl alcohol for three times, and then blown dry using ultrapure nitrogen gas. A standard solution with fluoride ions was prepared in advance to calibrate the Orion 96-09 fluoride ion combination electrode with low-level total ionic strength adjustment buffer solution (TISABII) added into the standard solution. An Orion 4-star pH/ISE bench top meter was utilized to read out the DC millivolt signal from the fluoride ion combination electrode. The direct calibration method was applied to determine the fluoride ion concentration in the cathode water by measuring the output voltage of the sample solution and comparing with the calibration curve. Meanwhile, pH values of the cathode water were determined using an Orion 520A pH meter.

5.5 Results and Discussions

5.5.1 Experimental Observations

In this section, the observations and results from the two MEAs aged under cyclic and constant current conditions are summarized and compared. Discussions regarding to the impacts of aging profile on MEA degradations are also presented.

5.5.1.1 Lifetime Data

The voltage profiles of MEA1 in 3 complete cycles are plotted for each 100h aging period in Figure 5-2, along with the values of high frequency resistance R_1, electrode resistance R_2 (the result of subtracting R_1 from the real resistance at low frequency) and the electrolyte-catalyst differential capacitance C_p at an intermediate current density. It can be seen that the voltages needed to maintain the specified current output decreased with time, and the voltage profile

shifted downward quickly for the last three aging periods. During the last 100h aging period from 900-1000h, voltage was just above 0.1V at 1.06 A/cm^2, implying that the MEA1 was close to its lifetime if the highest current level had to be reached. This may be the case for vehicles being driven in an uphill road situation. It should be noted that the lifetime of MEA1 seems rather short, compared to the literature values.[71,118-121] Unfortunately we were not able to obtain the manufacturing details for the commercial MEAs that we tested in our experiments. Nevertheless, the chances of experimental artifacts were minimized when we characterized the two MEAs, by carefully monitoring the operations of the FCT test stations with regard to temperature, pressure, gas flow and humidification control.

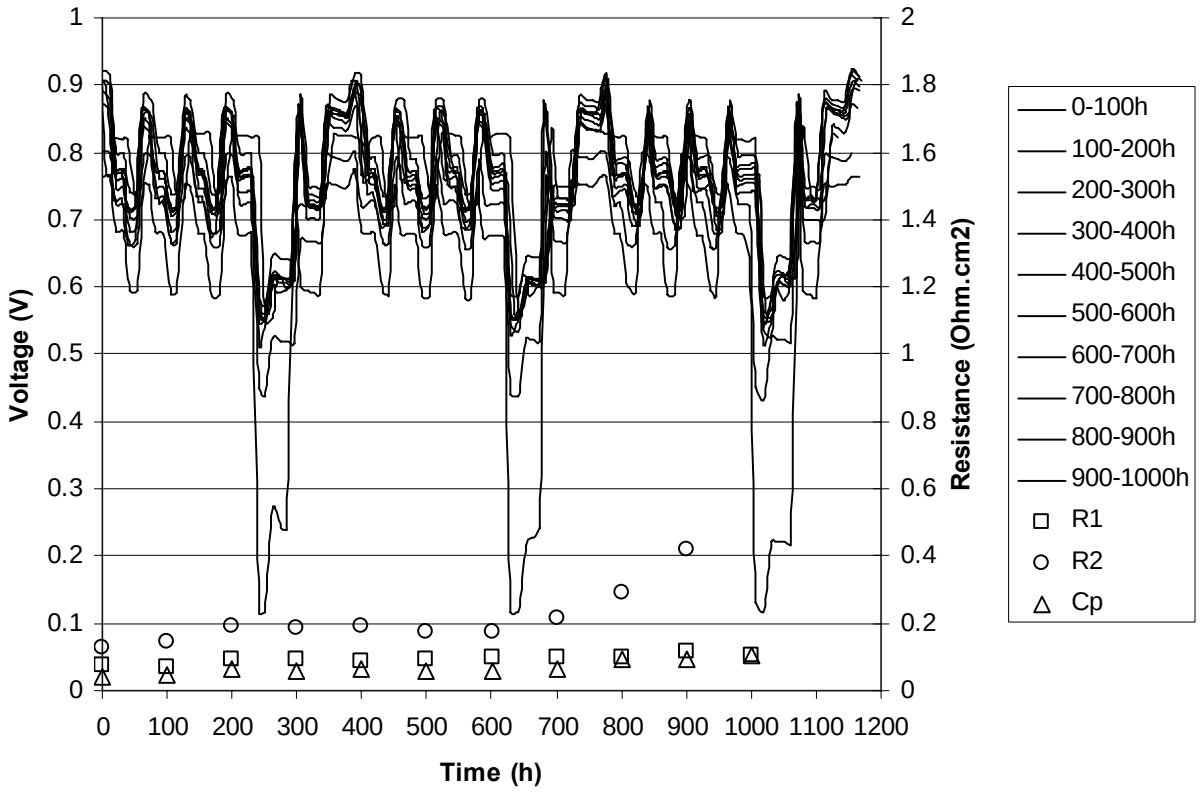

Figure 5-2. Comparisons of voltage profile of MEA1 (in 3 complete cycles) showed lower and lower voltages during the cyclic current aging process.

Figure 5-3 also reveals that high frequency resistance R_1 and capacitance C_p had almost constant values throughout the entire aging process. The electrode resistance at low frequency, R_2, increased more significantly by approximately 100% at 900 h. The value of R_2 could not be estimated at the end of 900-1000h aging period due to the unsteady current during the impedance measurement. According to Lefebvre, Martin and Pickup, R_2 can be considered as the specific combination of electronic resistance and ionic resistance from the membrane phase in the catalyst layer.[123] The increase of R_2 along with time indicates that the carbon support beneath the platinum particles might have been corroded or the recast ionomer at the electrolyte-catalyst interface had degraded, or both. More details in this regard will be discussed later in conjunction with the cathode water analysis.

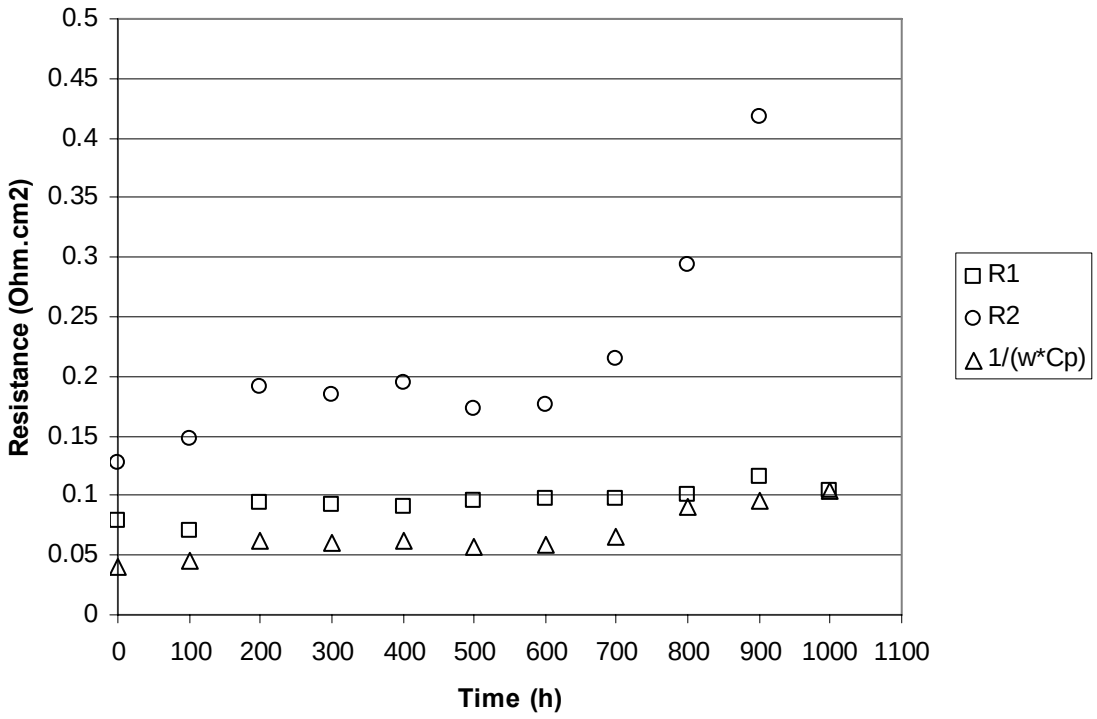

Figure 5-3. The low frequency resistance of MEA1, R_2 increased more significantly with time, here $w = 2\pi f$ and f is the frequency at 100 Hz.

Figure 5-4 illustrates the decay of voltages at the constant current density of 1.06 A/cm^2 for MEA2. The voltages were recorded and averaged at the beginning and end of 10 constant aging periods. Once again, the voltage decay was observed to occur very rapidly, with estimated rates of -160 uV/h for voltages at the beginning of aging periods and -255 uV/h at the end. The rates were considerably higher than those reported in the literature (~ -21 to -127 uV/h).[71] In addition, there was continuous decrease of voltages within each 100h aging period as shown in Figure 5-4 (by comparing the voltages vertically at the same time nodes), mainly due to the mass transport limitations existent on the cathode side. It was observed that the voltage continued to decrease for certain amount of time when the constant current operation resumed after the end-of-period diagnosis, and then reached a stable value for the rest of the aging period.

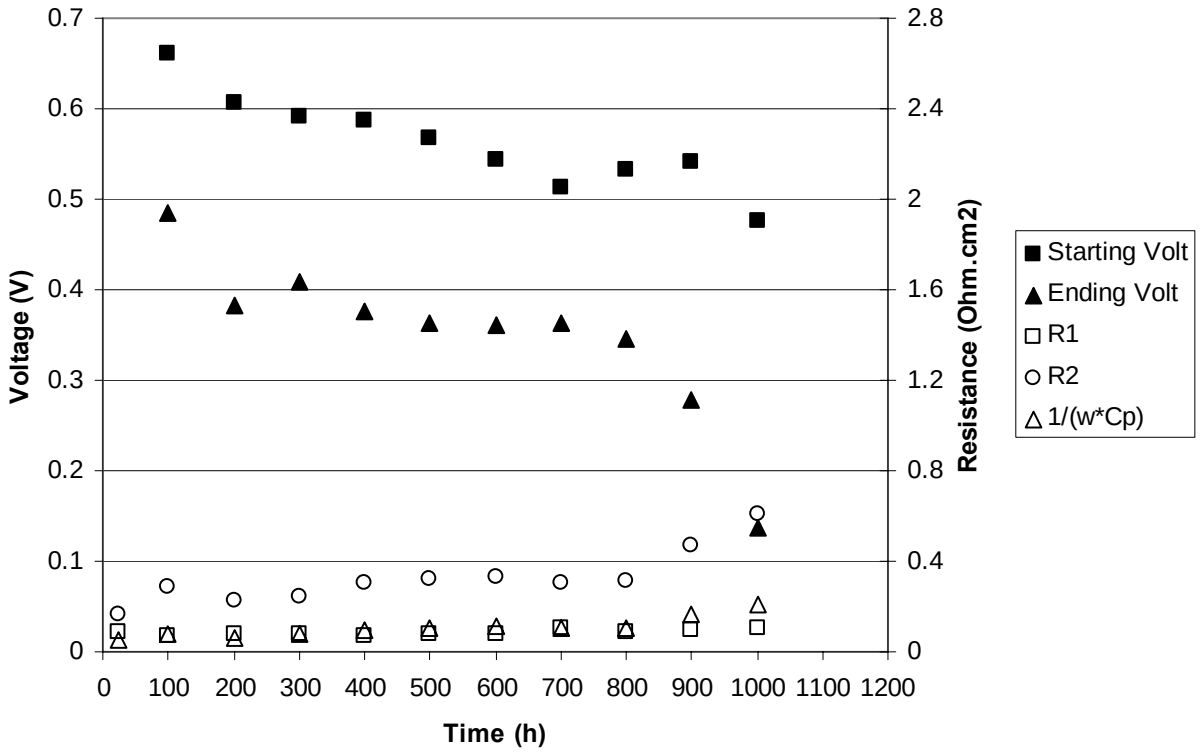

Figure 5-4. Cell voltages of MEA2 at 1.06 A/cm^2 showed continuous decreases at the beginning and end of the 10 aging periods under constant current mode. Similarly, R_2 increased with time. Here $w = 2\pi f$ and f is the frequency at 14.7 Hz.

The reason behind this phenomenon may be related to the slow competition among product water, humidification vapor and cathode water discharge. The cathode of MEA2 went through stages of initial dryness, water accumulation and final saturation at 1.06 A/cm^2. Since we were utilizing the standard 5 cm^2 test fixture and Teflon-coated fiber glass sealing gaskets, it may be that the commercial MEAs (supplied with GDL) did not possess good water expelling properties. Similar to MEA1 under cyclic aging conditions, the electrode resistance R_2 almost doubled at 1000h. The electrolyte-catalyst differential capacitance C_p also increased, indicating more charges may be stored in the carbon-catalyst-ionomer three-phase region.

5.5.1.2 Hydrogen Crossover Rate and Open Circuit Voltage

The trends of OCVs at the beginning and end of aging periods as well as the hydrogen crossover rates as a function of time are shown in Figure 5-5 for the cyclic current mode and Figure 5-5 for the constant current mode. The OCVs of cyclically aged MEA1 remained at approximately 0.9 V until 500h, when there were small differences between the values of OCVs at the beginning and end of aging periods. After 600h, bigger discrepancies began to exist due to aging and the OCV decreased almost linearly. At the end of 900-1000h aging period, the OCV was as low as 0.28 V. The decrease of OCV can usually be related to the mixed potential due to the direct reaction of fuel and oxidant at the cathode side. In our case, the OCV decay was in good accordance with the results of hydrogen crossover measurement. The hydrogen crossover rate rose considerably high after 500h and the potentiostat was not able to hold the fuel cell at 0.8V for a certain amount of time without exceeding the instrument limit between 800 and 1000h. Thus no data points were plotted in Figure 5-5 at these times. A reasonable explanation for the dramatic leap of hydrogen crossover rate was formation of pinholes in the thin N112 membrane after 500h of current cycling. Although it is difficult to attribute the pinhole formation to sole mechanical or chemical degradations in the membrane, the outcome of the degradations was permanently changing the membrane by forming macroscopic holes in it. Otherwise the hydrogen crossover rate would not be as high as 0.3-0.95 A/cm^2, assuming under normal circumstances the hydrogen molecules that migrated from anode to cathode came all from dissolved hydrogen.

Recently, there have been a trend towards the use of thinner membranes to reduce ohmic resistance and obtain higher efficiency for the fuel cell.[47,52,56,124] Our results from accelerated cyclic current aging suggested that the resistance of membranes to chemical and mechanical degradations is very important to sustain the fuel cell through various operation conditions and to last long enough in automotive transportation. Therefore, the durability of the membrane materials has to taken into account when developing the next generation proton exchange membranes, particularly the ability of the membranes to endure not only the attack of hydrogen peroxide radicals, but also hygrothermal mechanical stress. This may require the membranes to be a comprehensive product of tailored properties such as thickness, proton conductivity, mechanical strength/modulus, swelling behavior and so on.

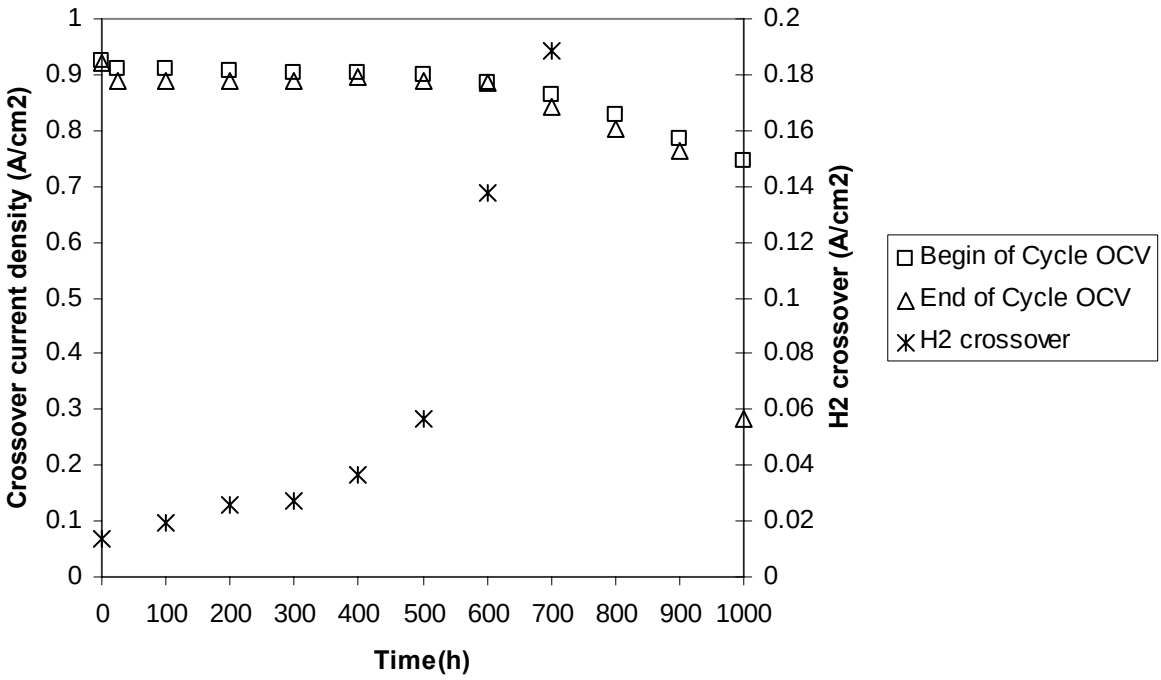

Figure 5-5. Decay of OCVs at the beginning and end of the 100h aging periods complied well with the trend of hydrogen crossover rate for MEA1 under cyclic current mode.

On the other hand, the OCVs of constant-current aged MEA2 fell into the 0.92-0.98 V region during the entire 1000h of aging. The hydrogen crossover rate fluctuated around 0.01 A/cm^2. No physical holes should have appeared in the membrane; otherwise considerable hydrogen

crossover would have caused the OCVs to drop to a large extent. This may be due to the fact that the membrane was wet for most of the time (operated at constant current density of 1.06 A/cm^2). The membrane was expected to have less mechanical degradations while the cyclic stresses due to dry-wet cycles did not exist in the MEA2 under constant current operation.

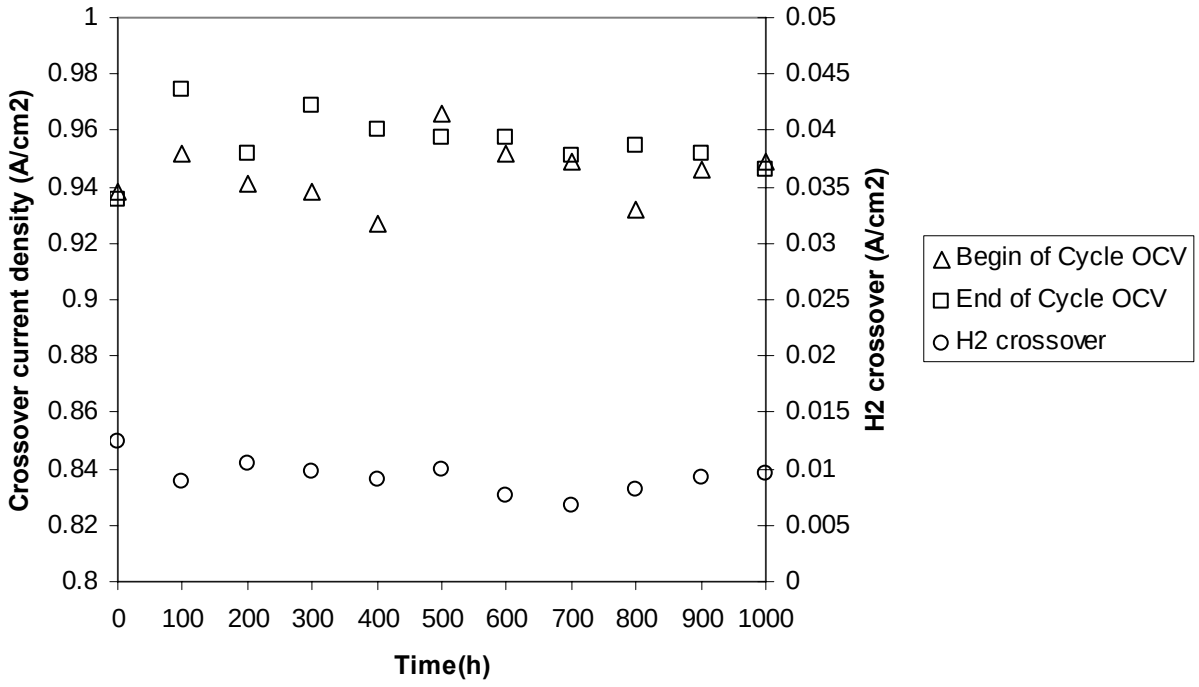

Figure 5-6. The OCVs of MEA2 at the beginning and end of the 100h aging periods and the hydrogen crossover rate remained relatively constant under constant current mode (1.06 A/cm^2).

5.5.1.3 Polarization Curves

The polarization curves of MEA1 under cyclic current aging mode are shown in Figure 5-7. When one examines the kinetic, ohmic and mass transport regions of the polarization curves, it is clearly illustrated that the most significant degradation that occurred to MEA1 was the lowering of the OCV, caused by the large amount of hydrogen crossover. The slopes of the curves at the ohmic region were very similar until 900h. The polarization curve at the end of 1000h aging was almost a straight line at very low current and voltage levels, indicating that MEA1 was approaching the end of its lifetime.

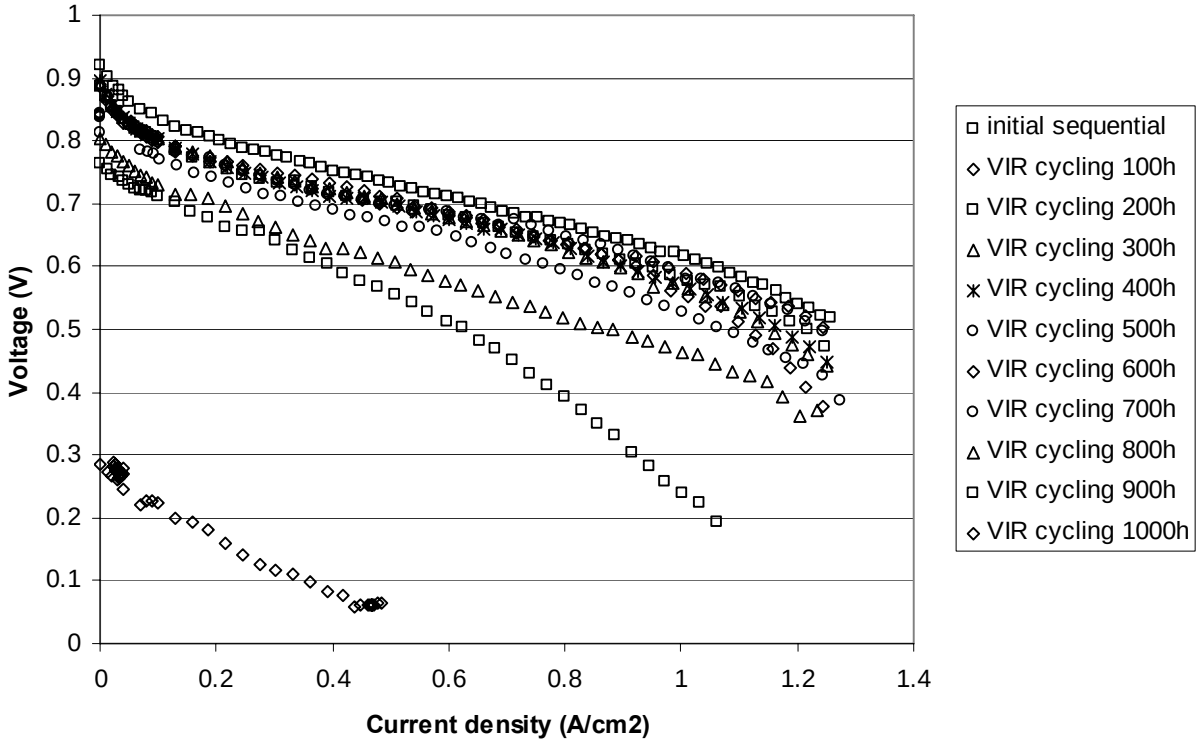

Figure 5-7. The polarization curves of MEA1 shifted downward during the cyclic current aging process mainly because of the lowering of OCV caused by hydrogen crossover.

The polarization curves of MEA2 aged under constant current are plotted in Figure 5-8. They demonstrate a very different trend compared to those of MEA1. Being consistent with the OCV result, the polarization curves converged to the approximate value of ~0.96 V at zero current density. There are larger discrepancies at the ohmic region of the polarization curves for MEA2, though the values of electrode resistances and capacitances (R_1, R_2, C_p measured from the impedance tests) did not change much through the aging process (see Figure 5-4). This may be attributed to the influence of mass transport on system characteristics. As mentioned before, the MEAs that we investigated in this study did not possess satisfactory long-term water management properties. The situation may have become so bad that the mass transport overpotential of the MEA2 began to decrease the cell voltage at a lower current density. However, the mass transport degradations that occurred to MEA2 were partially reversible, as

we performed the end-of-period diagnosis with lower current densities. By the time the impedance measurements were taken, the degree of water saturation on the cathode side of MEA2 may have already changed from that when MEA2 was actually aged at the current density of 1.06 A/cm^2.

The reversibility of mass transport limitation could also help explain why the polarization curves for MEA2 did not shift downstream in a straight order of 100, 200, 300h … to 1000h. The fuel cell characterizations themselves may control the MEA to be under certain conditions, which could perhaps alter the state of the MEA itself. As a result, the long-term characteristics of fuel cell MEAs should be judged relatively, because the results are affected by the operation history of the MEAs by various instruments. Therefore, there is a need to establish a standard protocol for PEMFC durability diagnosis, simply to make the test results obtained from different agencies comparable.

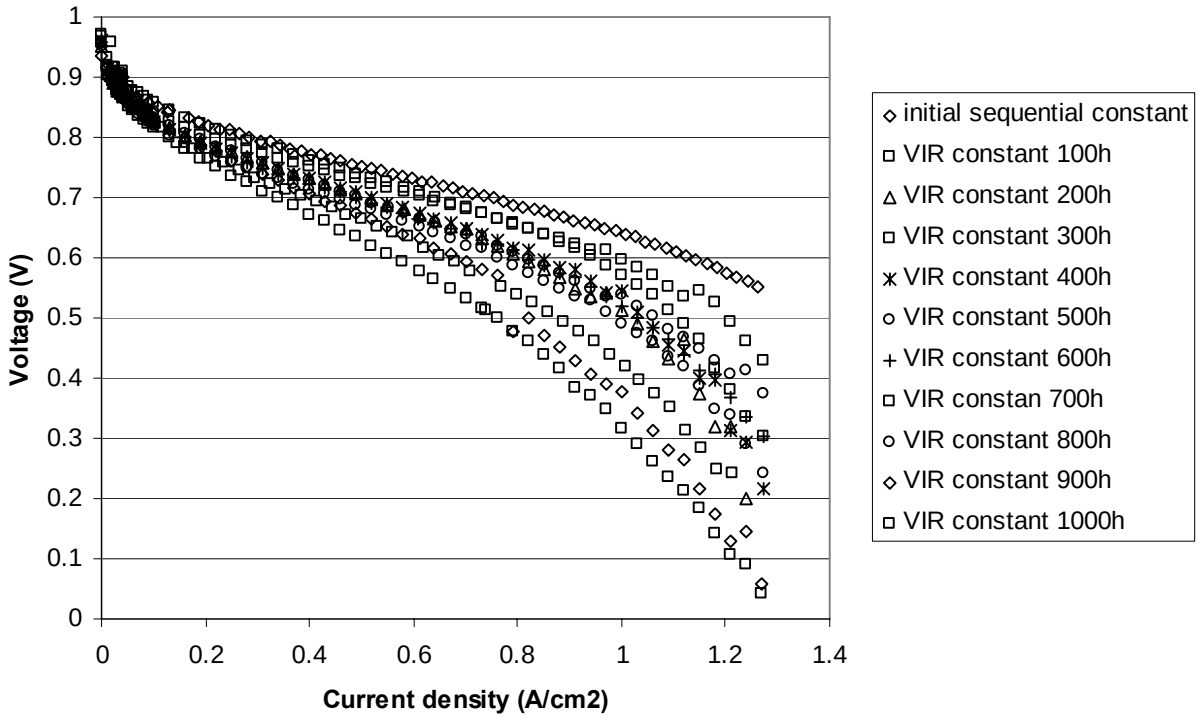

Figure 5-8. Comparisons of the polarization curves of MEA2 illustrated major degradations in the mass transport region during the constant current aging process.

5.5.1.4 Tafel Plots

Figure 5-9 shows the Tafel plots of the MEA1 from break-in to the last aging period. The Tafel plots can be divided into two groups with the division marked by a large shift-down between 600 to 700h, corresponding to the large increase of hydrogen crossover rate. This further demonstrates the change in the fuel cell system at that time, most likely due to pinhole formation in the membrane. Although an attempt was made to extract electrochemical kinetic parameters from the Tafel plots, no reasonable values for Tafel slope b and exchange current density i_0 were successfully obtained. From Figure 5-9, it is discernable that the voltage - log(i) plots formed nearly horizontal lines till 10^{-4} to 10^{-3} A/cm^2 of current densities and then curled up continuously at higher current densities. There were no distinct linear regions from these curves, which resulted in great difficulty and uncertainty in determining the values of Tafel slopes and extrapolating the curves to intercept the highest horizontal lines at equilibrium. Wang, Myers and Kumar at Argonne National Laboratories (ANL) employed a rotating ring-disk electrode (RDE) apparatus to evaluate the oxygen reduction reaction (ORR) kinetics.[125] By applying the RDE technique, a well controlled mass transfer environment was provided for the electrochemical reactions to occur in a much more delicate manner than that manipulated by a fuel cell test station. Consequently, the mass transport effect on potentiodynamic cell operation was minimized and the current density of the fuel cell can go down to as low as 10^{-11} A/cm^2. The ANL effort showed that the exchange current density for ORR at the platinum/carbon/Nafion interface at 90^{o}C was about 3.1×10^{-9} A/cm^2, a number that is beyond the lowest limits of the Tafel plots we obtained by simply connecting the fuel cell test station with the potentiostat. Therefore, despite the fact that the current state-of-the-art fuel cell test station could perform the bulk of the MEA characterizations, development of more accurate mass transport control is required as to improve the accuracy of electrochemical kinetics measurements.

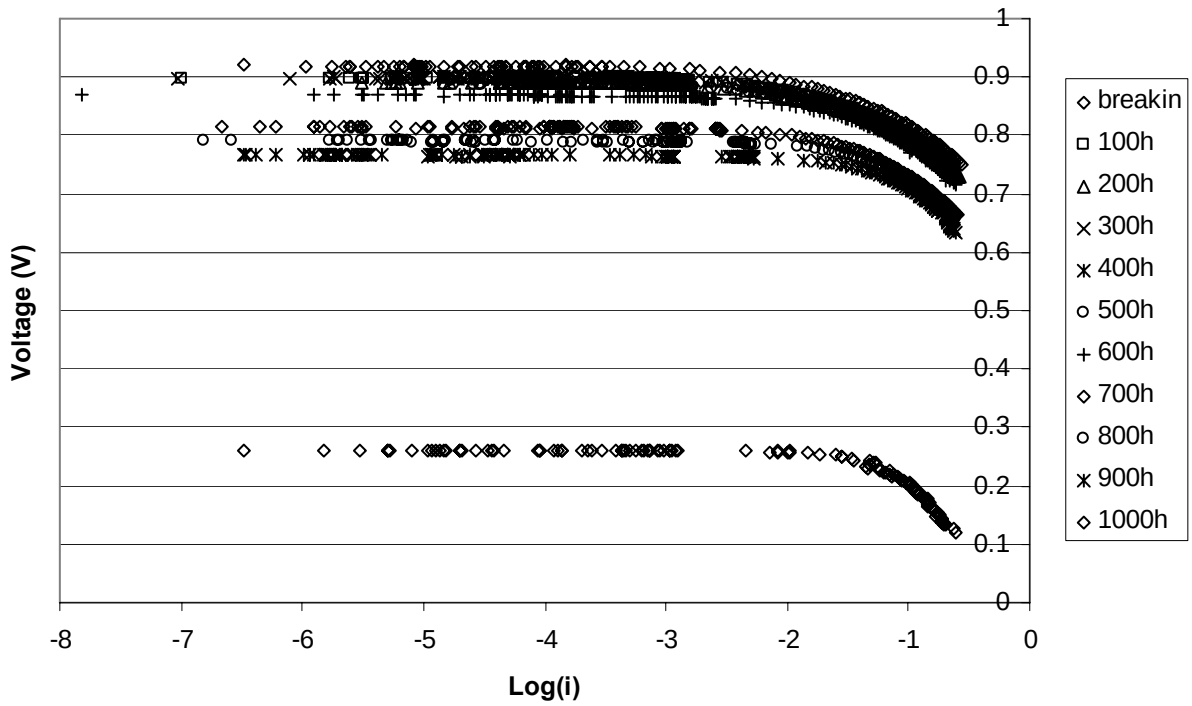

Figure 5-9. Tafel plots of MEA1 operated using FCT test station #1 had lower and lower voltages at current densities up to 0.2 A/cm^2 during the cyclic current aging process.

It can be seen in Figure 5-10 that the Tafel plots for MEA2 under constant aging mode were almost identical except the one taken right after break-in period. These results substantiated the reversibility of mass transport-induced degradations in fuel cell performance. Again, when the Tafel plots were acquired, the water content in the MEA2 cathode further decreased. Air could flow better and reach the reaction sites much easier after the flooding problem was resolved at the cathode. The Tafel plots did not display significant degradations even at 1000h with current densities ranging between 0 and 0.2 A/cm^2. Although the aging experiment was terminated, it is reasonable to expect that the lifetime of MEA2 could be well above 1000h. The mass transport issues can be mitigated by frequently drying out the MEA2. Based upon above observations, we found out that the current output profile of the fuel cell has had a strong impact on its degradation mechanisms, long-term performance and ultimately, the lifetime. Hence, simplistic testing and verification of new materials (especially membranes) after break-in via polarization curve measurements may not be sufficient to support the full validity of those materials to be

utilized as fuel cell components. Systematic evaluation with respect to various operation conditions is preferred.

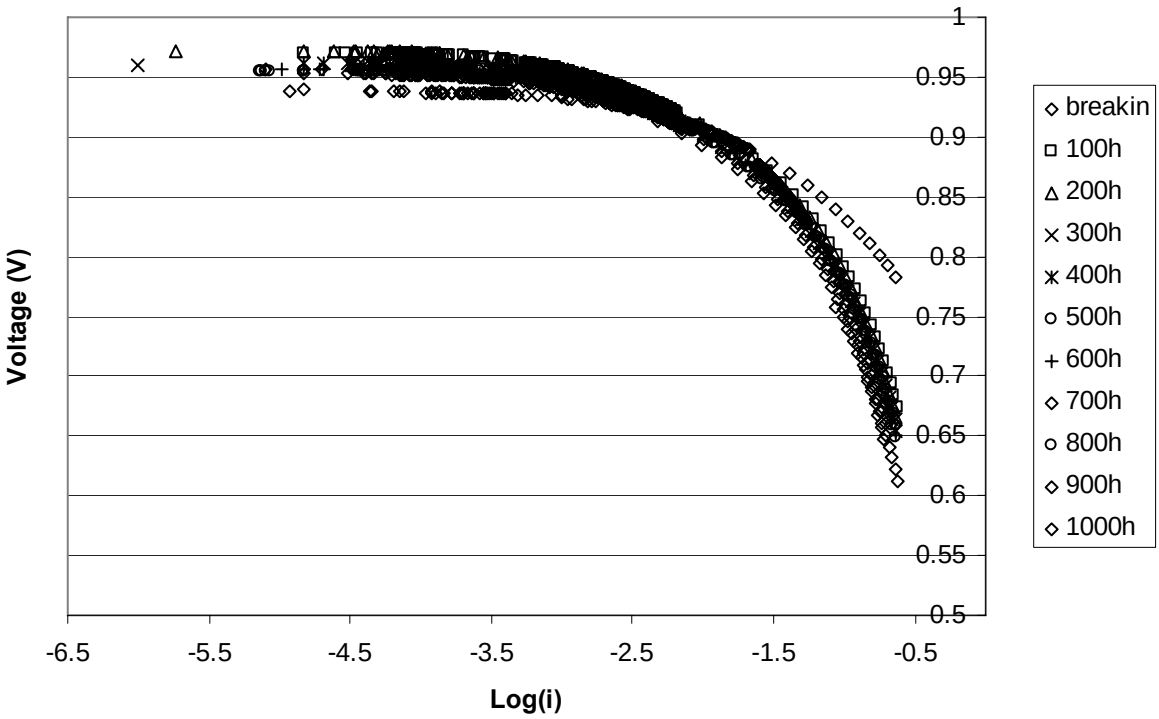

Figure 5-10. Tafel plots of MEA2 were almost identical except the one taken after break-in during the 1000h of constant current aging process.

5.5.1.5 Electrochemical Reactive Surface (EAS) Trends for Both Electrodes

Figure 5-11 illustrates both of the anode and cathode EAS areas against time for MEA1 and ME2. The EAS could not be measured by CV after 600-700h of aging under cyclic current aging conditions due to large amount of hydrogen crossover. In spite of the fact that the two MEAs were supposed to be manufactured the same way, the initial EAS areas of MEA2 were almost twice as those of MEA1, which implies that the current MEA manufacturing technique may still have limitations in terms of product consistency. Nevertheless, the EAS of both MEAs showed similar trends of exponential-like decay, while the constant current-aged MEA2 lost its EAS at a faster speed. Based on our current understanding, the decrease of EAS will have a significant

impact on the fuel cell performance. For most of the cases, the output current produced from an energy device is quantified in the form of current density, defined as the current divided by the active surface area of the device. In the case of fuel cells, the current density is calculated using the nominal MEA area (such as 5 cm^2), i.e., the area of a common region shared by the fuel cell membrane, catalyst layer and gas diffusion layer. Yet, the current drawn from a fuel cell system is actually generated at the electrochemical active sites. If less EAS (hence less energy density) is available for the electrochemical reactions to take place while the output current density is still regulated as the same by the electronic load box, one can imagine that the voltage needed to drive the fuel cell has to be lower according to the polarization nature of the fuel cell. In order to reflect this process, a mathematical manipulation was invented by use of a term named "local current density", which is the outcome of nominal current density and percentage of residue EAS on the fuel cell electrodes. The influence of EAS on cell performance has been taken into account during our phenomenological durability modeling, as further described in section 5.5.2.

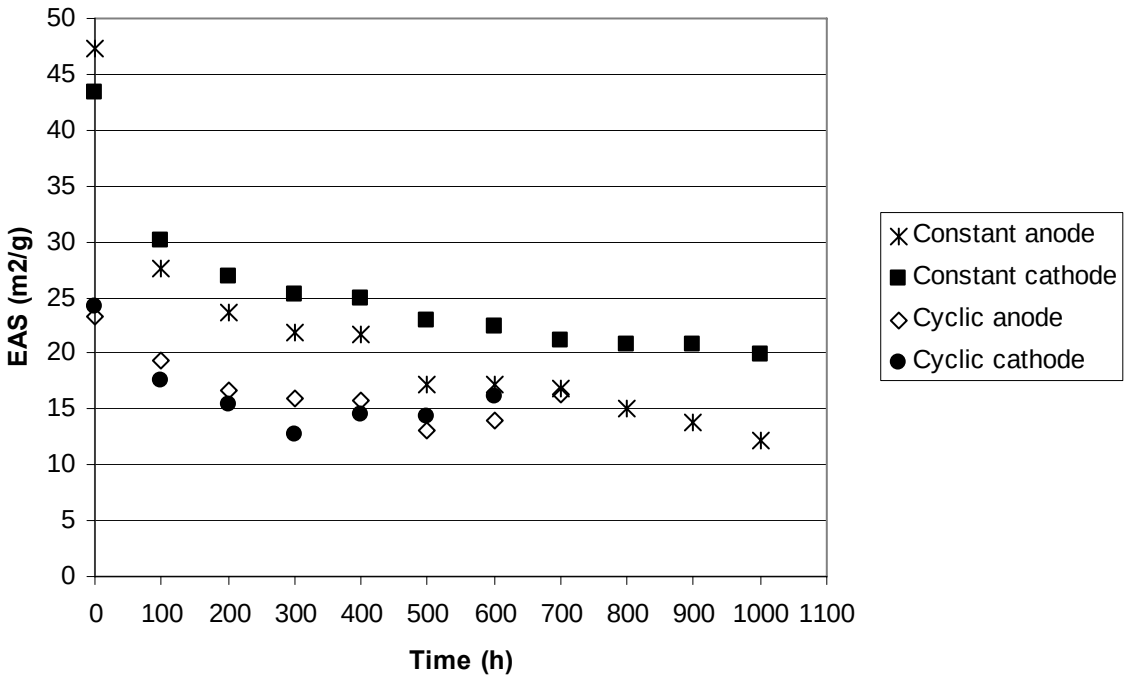

Figure 5-11. The changes of EAS areas as a function of time were shown for both anode and cathode of MEA1 and MEA2. The catalyst loadings were 0.5mg/cm^2.

5.5.1.6 Fluoride Ion Concentration and pH Values

The trends of fluoride ion concentration in the cathode exhaust water were compared for MEA1 and MEA2 in Figure 5-12. The fluoride ion concentrations decreased along with time, as opposed to the results reported by Xie and co-workers.[121] The probability of artifacts from contamination of the water sample was small, because there was enough time including MEA break-in period to wash away any residue fluoride ions left in the fuel cell testing system before the first water sample was collected. If we assume the fluoride ion release rate from the MEA was proportional to the fluoride ion concentration in the cathode outlet water, it is very likely that the fluoride ions came from the decomposition products of the recast ionomer in the catalyst layer (corresponding to the increase of R_2) and/or the membrane. The trends of the fluoride ion concentration in Figure 5-12 resembled the solution to first order reaction kinetics equation:

$$\frac{dM}{dt} = -kM \qquad \text{- (42)}$$

where M is the mass of the recast ionomer/membrane (Nafion) present and k is the rate constant for decomposition. This observation coincides with the remarks given in Ref 76 that the kinetics of Nafion membrane degradation in Fenton's reagent can be represented by the expression of

$$-\log(\%\,\text{degradation}) = kt \qquad \text{- (43)}$$ [76]

It also appears that the fluoride ion concentrations from MEA1 under cyclic current aging conditions were about 30 fold higher than those from MEA2 under constant current operation. Although more experiments need to be performed to confirm our observation, the fact of early membrane failure with cyclic current output implies that there might be strong interactions between the chemical and mechanical degradations of ionomers. Hygromechanical stress may accelerate the chemical decomposition of Nafion, most likely, the dissolution of recast Nafion ionomer in the catalyst layer, referring to the suggestions by Xie[121] and LaConti et al.[76]

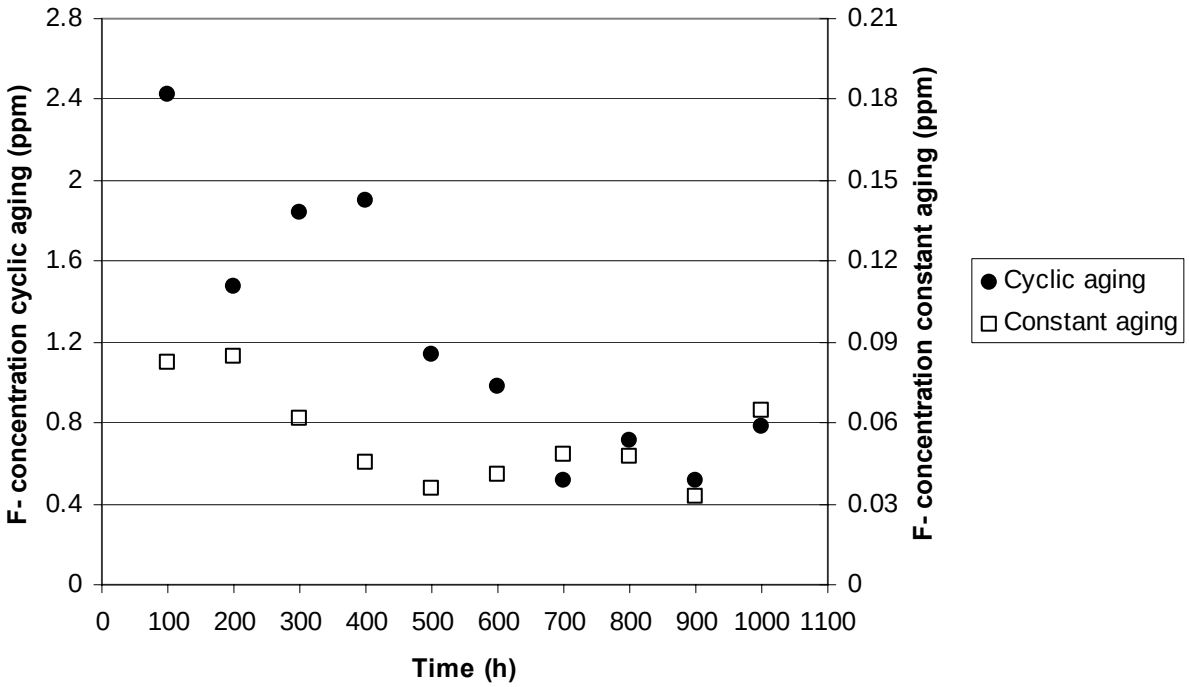

Figure 5-12. The fluoride ion concentrations in cathode outlet water were measured for MEA1 under cyclic aging conditions and MEA2 under constant aging conditions. The fluoride ion release rate was about 30 fold larger for MEA1 than that of MEA2.

The detailed study of Nafion membrane decomposition in Fenton's reagent or in the fuel cell environment has been carried out in companies including Dupont, General Motor (GM), United technology (UTC) fuel cells and 3M. The chemical degradation mechanisms were investigated based on the method of model compounds and some basic agreements have been reached. It is usually considered that the peroxides and their radicals attack the carboxylate end groups of Nafion, which release carbon dioxide (CO_2), hydroxyl radical ($OH\cdot$) and hypofluoric acid (HF) and form new carboxylate groups at the chain ends. By repeating the process, the attack propagates along the main chain of the polymer (refer to Schematic 1).[126] Consequently, one could expect variations with respect to the pH values of cathode exhaust water. Figure 5-13 illustrates the changes of pH as a function of time for both MEA1 and MEA2. Surprisingly, the pH values showed opposite trends for cyclic and constant current mode. The pH of cathode water collected under cyclic aging conditions decreased first, and then increased. It can be speculated that the membrane degradation had taken place more thoroughly with cyclic current profile,

where a certain amount of hypofluoric acid was generated. Hence the pH value decreased. As the chemical degradation of Nafion slowed down because of the reduction in mass of the available ionomer, less HF acid was produced and the pH increased. Meanwhile, for the case of constant current aged membrane, the peroxide attack might have been terminated at the earlier steps, which gives off OH· radicals as the side product. This would lead to a higher value of pH, as evidenced in Figure 5-13. Similarly, when less ionomers were left in the fuel cell, the release of hydroxyl radicals was lowered, raising the pH values.

$$(CF_2)_n\text{-}CO_2H + H_2O_2 \rightarrow (CF_2)_n\,CO_2\cdot + \cdot OH$$
$$(CF_2)_n\text{-}CO_2\cdot + \cdot OH \rightarrow (CF_2)_{n-1}\,CF_2OH + CO_2\uparrow$$
$$(CF_2)_{n-1}\text{-}CF_2OH \rightarrow (CF_2)_{n-1}COF + HF$$
$$(CF_2)_{n-1}\text{-}COF + H_2O \rightarrow (CF_2)_{n-1}CO_2H + HF$$

Schematic 1: The proposed chemical degradation mechanism of Nafion, which involves attacks of carboxylate end group by peroxide and sequential propagation along the main chain.

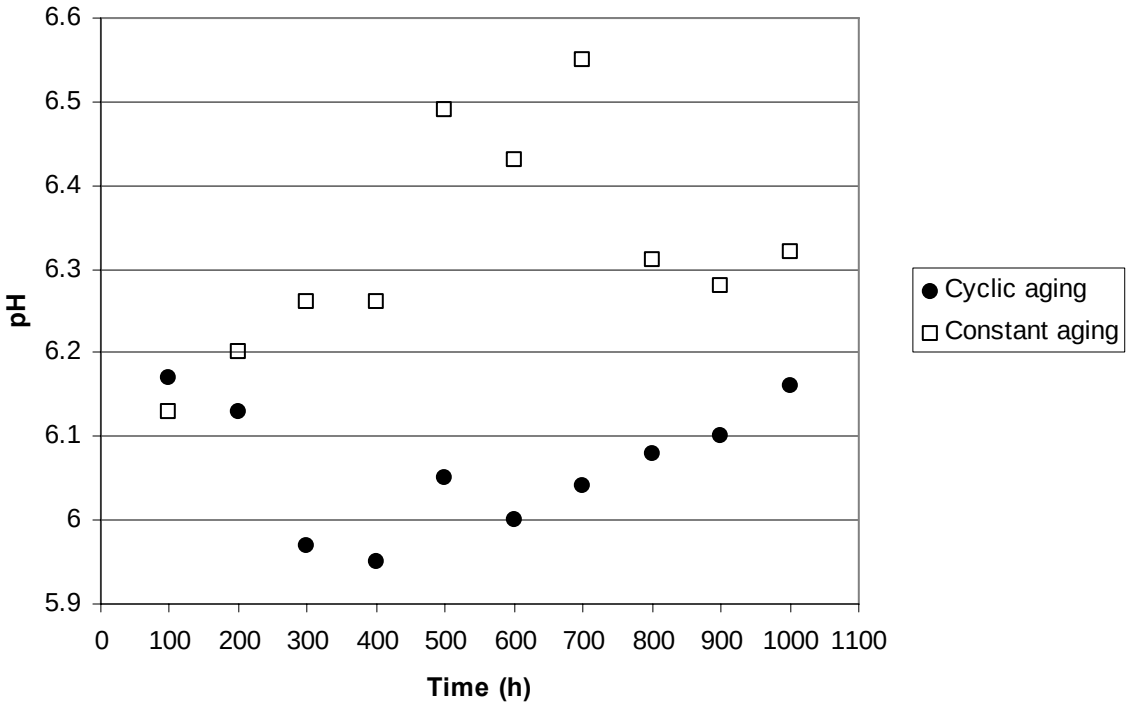

Figure 5-13. The pH values of the cathode outlet water demonstrated opposite trends for MEA1 under cyclic aging condition and MEA2 under constant aging condition.

5.5.2 PEMFC Durability Modeling

The semi-empirical phenomenological durability modeling for PEMFCs under both cyclic and constant aging conditions was attempted to incorporate observed aging phenomena and describe the cell performance at different time periods.

5.5.2.1 Modeling Principles

The semi-empirical equation that comprises the core of the phenomenological durability model is the following:[5]

$$V = E_r - \frac{RT}{2F}\ln\frac{a_{H_2O}}{a_{H_2}a_{O_2}^{\frac{1}{2}}} - i\cdot R_H - A\ln\frac{i}{i_0} + B\ln(1-\frac{i}{i_l}) \qquad \text{- (44)}$$

Where E_r is the cell reversible potential and equal to 1.18 V at the cell temperature of 80 ^{o}C,[5] a_{H_2}, a_{H_2O} and a_{O_2} are the chemical activities of the fuel, oxygen and product water, R_H is the high frequency resistance of the fuel cell measured simultaneously with the polarization curves, A and B are both empirical constants and equal to as $\frac{RT}{n\alpha F}$. Here R is the gas constant, T is the absolute cell temperature, n is the number of electrons transferred per electrochemical act, α is the charge transfer coefficient and F is the Faraday's constant. The symbol of i_0 is the exchange current density that is assumed to be a constant during the entire aging process. Most importantly, i is the mathematical "local current density" that is "modulated" on the membrane-catalyst interface to achieve the nominal output of current density and can be calculated based upon the nominal/apparent current density i_{app}, the internal current density due to hydrogen crossover i_n and the percentage of residue catalyst surface area p_{eas} as:

$$i = \frac{(i_{app} + i_n)}{p_{eas}} \qquad \text{- (45)}$$

Similarly, i_l is a function of the limiting apparent current density i_{l0} (the current density at which cell voltage goes to zero) and can be calculated by $i = \frac{(i_{l0} + i_n)}{p_{eas}}$.

Having the main equation set up, the model parameters including R, i_n, p_{eas} and i_{lo} were then implemented into the semi-empirical equation with values corresponding to 11 time nodes, 0, 100, 200, 300… to 1000h. The exchange current density i_0 was utilized as the sole adjustment parameter during the modeling process. The voltage decays at several current densities under constant current mode and in three aging cycles under cyclic current mode were computed. The cell polarization curves at 11 time nodes were assessed and compared with the experimental results.

5.5.2.2 Modeling Results

Figure 5-14 presents the modeling and experimental voltage results for MEA2 at current densities of 0.2, 0.7 and 1.06 A/cm^2. It can be seen that the "model-predicted" trends provided very good fits to the experimental data. In particular, for voltages at 1.06 A/cm^2, the voltage curve fell in between the actual voltages measured at the beginning and end of the 10 aging periods. This is what we have expected, since the values of the model parameters were obtained when the water content of the MEA2 already deviated from that during the constant current operation and ranged between the numbers at the driest and wettest states.

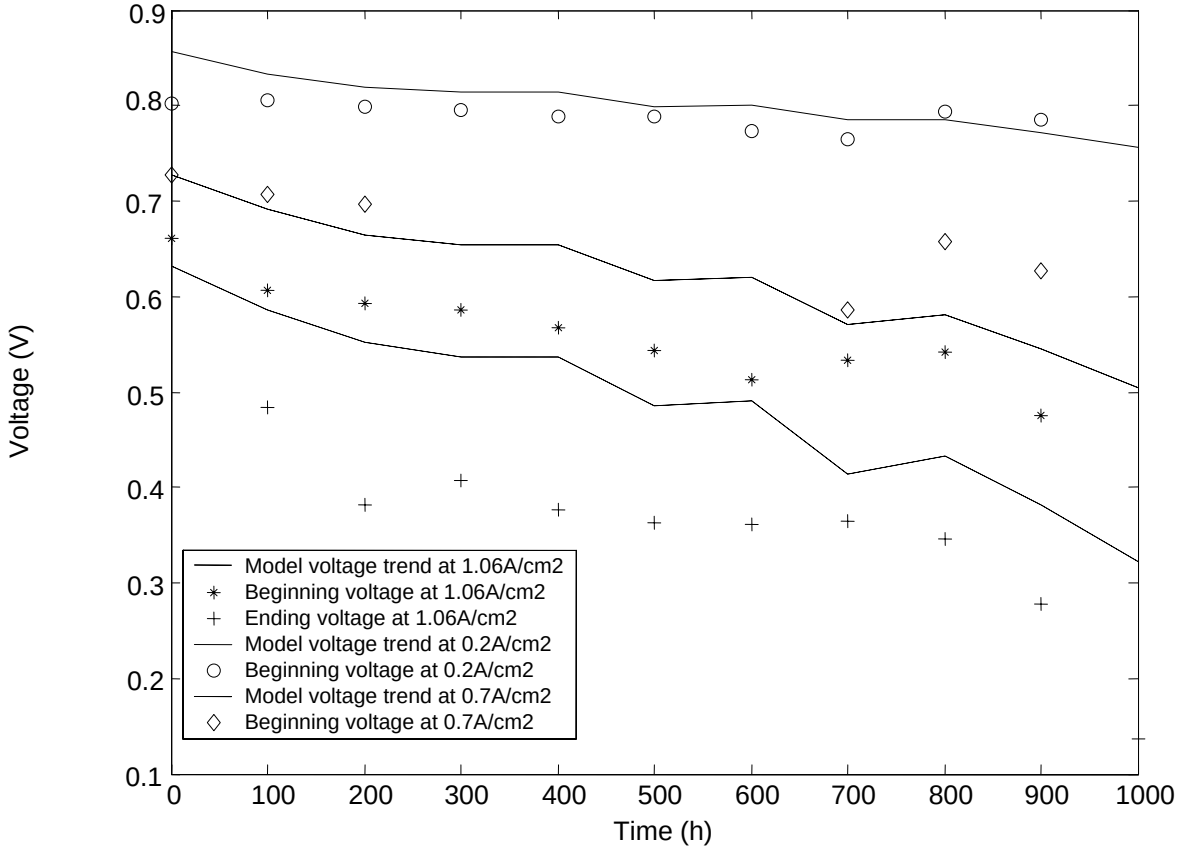

Figure 5-14. The model predicted and experimental voltage trends for MEA2 at 0.2, 0.7 and 1.06 A/cm^2 under constant aging conditions.

The results in Figure 5-15 demonstrate that the phenomenological durability model can successfully generate the polarization curves for aged MEAs at different time periods. The calculated polarization curves shifted downward and the current density at which the power curves reached their peak values was lowered in a similar fashion as the experimental results. The maximum power output decreased by approximately 10%, which is a good indication of the deterioration in the fuel cell system. This type of information is quite useful when evaluating the extent of degradations in fuel cells, but certainly time-dependent constitutive relations for fuel cell components need to be incorporated into the durability model as to bring the model with more predictive power.

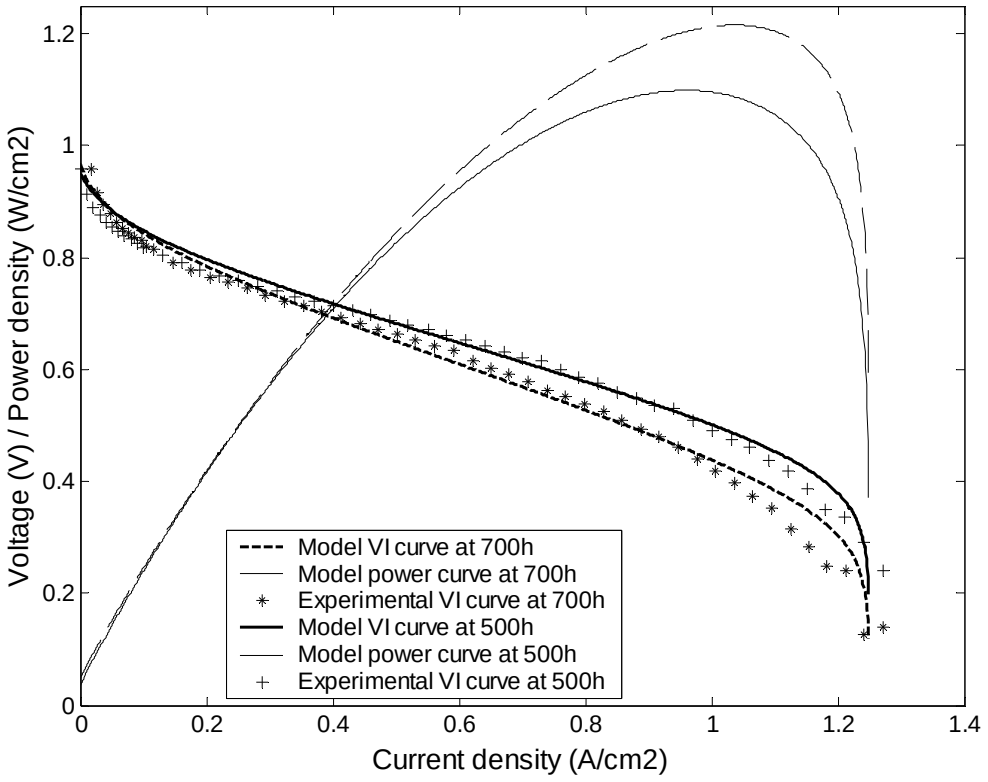

Figure 5-15. The model predicted and experimental polarization curves for MEA2 at 500 and 700h under constant aging conditions.

The model predicted and experimental cyclic voltage profiles for MEA1 at 400h were illustrated in Figure 5-16. The experimental voltage profile was found to have phase lag behind the model predicted profile. The reason behind this may be that due to the "ramp times" for the current to change from one setting to another. It took some time (although may be very short) for the fuel cell system to complete current step changes, especially the more dramatic ones such as step 14 to step 15 in Table 1. Once the designated current level was reached, the fixed plateau time when the current stayed at the set point began to elapse till the onset of next segment. This lagging behind due to extra "ramp time" further accumulated down the road, creating more and more phase differences. It should be noted here that the phase lag between model predicted and experimental voltage profile is a reflection of the nature of our phenomenological model. The phenomenological model is a steady-state model that computes the performances of the PEM fuel cell only at specified time nodes. A transient

model is required in order for the model to capture the dynamic behavior of a fuel cell under current step changes.

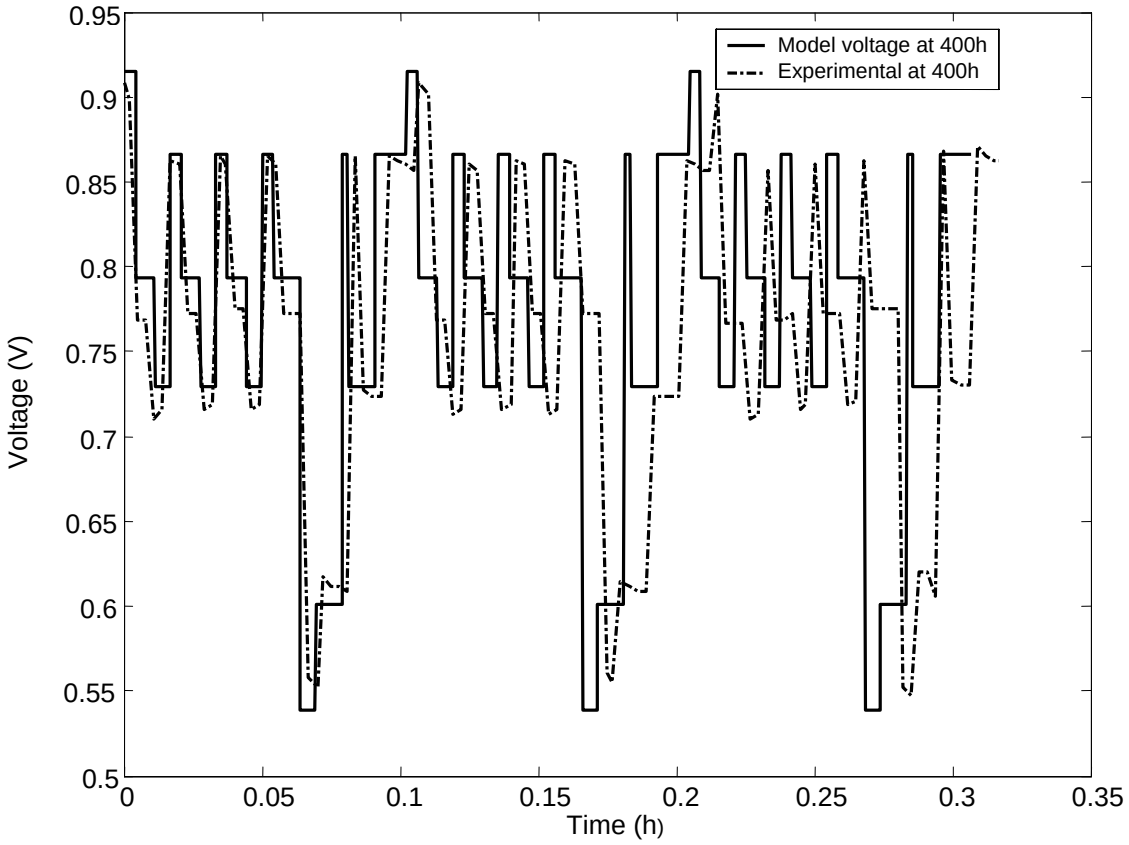

Figure 5-16. The model predicted and experimental cyclic voltage profiles for MEA1 at 400h.

5.6 Conclusions

In this article, the long-term durability of hydrogen-air proton exchange membrane fuel cells (PEMFCs) was investigated under both cyclic and constant current conditions for 1000h using the same type of MEAs. The end-of-period diagnosis including cell polarization, impedance spectrum, Tafel plot, hydrogen crossover rate as well as electrochemical active surface area was performed at a regular basis. It was demonstrated that hydrogen crossover was the most dominant degradation source for cyclic current aging after 500-600h and the MEA1 reached its lifetime after 1000h of operation. Mass transport limitations were identified as the major

degradation source of the MEA2 under constant current conditions. The degradation in performance of MEA2 was partially reversible when cathode flooding was resolved after the cell undergone the series of end-of-period characterizations. A semi-empirical phenomenological durability model was successfully established to incorporate the aging observations and describe the cell performance along with time. The results illustrated the demand for standard fuel cell durability test protocol and membrane pinhole reduction study.

Chapter 6. Conclusions

6.1 Summary

In this dissertation, the tensile behavior of Nafion® 117 (N117) and sulfonated Poly(arylene ether sulfone) random copolymer (BPSH35) membranes was explored under ambient conditions, with respect to the effects of strain rate, counterion type, molecular weight and the presence of inorganic fillers. It was found that the yielding behavior was affected by strain rates for both N117 and BPSH35-R films. The stress-strain curves of N117-H and N117-Na samples exhibited larger deviations at strains above the yield strain. Increase of molecular weight for BPSH-MW specimens resulted in improved elongation at break. Enhanced mechanical properties were observed for the BPSH35-ZrPP (2%, w/w) composite membrane compared to its matrix BPSH35-R film. A bundle-cluster model was proposed to interpret the tensile observations, combining the concepts of elongated polymer aggregates, proton conduction channels, as well as states of water. The rationale focuses on the chain motions in the hydrophobic phase, i.e. bundle rotation before yielding and polymer aggregates disentanglement/reorientation after yielding. In addition, the stress relaxations of N117 and BPSH35 films were measured at different strain levels and different strain rates. Although the relaxations fall into the nonviscoelasticity regime, master curves of log(stress relaxation modulus) vs. log(time) were able to be constructed.

Meanwhile, the influences of uniaxial loading on proton conductivity of N117 and BPSH35 membranes are investigated. The relaxation of proton conductivity and stress of N117-H membranes under ambient conditions and immersed in water were measured at a constant strain at temperatures of 30, 50 and 70^{o}C and different strain levels at 30^{o}C. The proton conductivities of the stretched film increased compared to those at the unstretched state. Detailed relaxation experiments revealed that proton conductivities relaxed exponentially with time under strain. The stresses of N117-H film relaxed faster in air and in water than proton conductivity. The speculation for above phenomena may be related to the combination effects of bundle rotation/aggregates disentanglements and the hydrophilic channel connectivity/reorientation. Similar trends were also found for BPSH35 materials. The NE1035-H membrane exhibited more pronounced proton conductivity hysteresis. Larger swelling irreversibility of NE1035-H film was

assigned as the reason. When modeling the change of PEMFC performance as function of time, the information obtained thus far would be valuable to define the constitutive relations.

The long-term durability of hydrogen-air proton exchange membrane fuel cells (PEMFCs) was investigated under both cyclic and constant current conditions for 1000h using the same type of MEAs. The MEA diagnosis including cell polarization, impedance spectrum, Tafel plot, hydrogen crossover rate as well as electrochemical active surface area was performed after each 100h aging period. It was demonstrated that hydrogen crossover was the most dominant degradation source for cyclic current aging after 500-600h and the MEA1 reached its lifetime after 1000h of operation. Mass transport limitations were identified as the major degradation source of the MEA2 under constant current conditions. The degradation in performance of MEA2 was partially reversible when cathode flooding was resolved after the cell undergone the series of end-of-period characterizations. A semi-empirical phenomenological durability model was successfully established to incorporate the aging observations and describe the cell performance along with time. The results illustrated the demand for standard fuel cell durability test protocol and membrane pinhole reduction study.

6.2 Future Work

In the short term, the future work based on this research could involve:

1. Validating the "Bundle-Cluster" Model

In order to validate the "Bundle-Cluster" model, it would be necessary to perform the tensile tests in wet conditions and compare with the model predictions. When the water content of a PEM is higher, one would expect weakened intermolecular/electrostatic interactions in the hydrophobic/ hydrophilic phase due to the plasticizing effect of water molecules, and further development of hydrogen bonding. These would lead to larger diameters of ionic-clusters, more randomly-oriented bundles, swollen channels and decreases in mechanical modulus and strength.[95,107,108,109]

2. Modeling the Proton Conductivity under Strain

The proton conduction behavior of PEM under strain itself is an interesting topic worth further investigations. The change of proton conductivity under strain in the transverse direction of the PEM can be measured and compared with the results from the machine direction. The Nernst-Einstein equation, $\sigma_{H^+}^{\alpha} = \frac{\varepsilon_i}{\tau}\frac{F^2}{RT} D_{H^+}^{\alpha} C_{H^+}^{\alpha}$, indicates that proton conductivity is a function of proton diffusion coefficient $D_{H^+}^{\alpha}$, local proton concentration $C_{H^+}^{\alpha}$ and the tortuosity factor of the hydrophilic channels.[127] To expand this equation and provide a detailed relationship between the tortuosity factor and the applied strain, one could apply the T2 experiments of ^{1}H NMR to stretched films, extract information regarding to $D_{H^+}^{\alpha}$ and $C_{H^+}^{\alpha}$, then back calculate the tortuosity factor of that membrane. The objective of this effort is to correlate the microscopic morphological evolutions with the changes in proton conductivity, which would benefit the PEMFC durability modeling.

3. Membrane Pinhole Study and Components Durability Characterization

The stress state analysis of PEMs in conjunction with the characterizations of residual strength and viscoelasticity behavior of PEMs under cyclic, hygro-thermal mechanical loading conditions needs to be carried out to predict the onset of pinhole formation. Based upon the results of our PEMFC aging study, there could be several ways to reduce pinhole formation in the membrane, including synthesis of membranes with higher yielding stress/strain, higher mechanical strength and less swelling when saturated with water, alternative method for MEA fabrication which employs chemical processes to adhere the components together instead of hot pressing (that may cause stress concentrations).

Finally, to reach the goal of microscopic durability modeling, the degradations of PEMFC components under various operation conditions must be understood. This may require detailed investigations of one component at a time, by setting other configurations constant. Advanced chemical analysis and imaging equipments will be essential to the research effort, enabling accurate mapping and characterizations of that particular component.

References

1. Malika Rajan, Global SOFC market to reach each $335 million by 2008, http://www.bccresearch.com/editors/RGB-282.html, 2003
2. G. Hoogers (Editor), Fuel cell technology handbook, 1st edition, CRC press, 2002
3. L. Carrette, K. A. Friedrich and U. Stimming, Fuel cells - fundamentals and applications, Fuel Cells, 1(1), 2001, 5-39
4. D. R. Crow, Principles and applications of electrochemistry, 4th edition, London: New York: Blackie, 1994
5. J. Larminie and A. Dicks, Fuel cell system explained, John Wiley & Sons, 2000
6. T. Berning, Three-dimensional computational analysis of transport phenomena in a PEM fuel cell, Ph. D dissertation submitted to the University of Victoria, Canada, 1997
7. C. M. A. Brett and A. M. O. Brett, Electrochemistry: principles, methods, and applications, Oxford University Press, 1993
8. J. Bockris, Fuel cells - their electrochemistry, McGraw-Hill, 1969
9. E. Stuve, http://faculty.washington.edu/stuve/chula03/ecat_chula_lec6.pdf, Catalysis and Electrocatalysis class note, July 2003
10. D. B. Sepa, L. M. Vracar, M. V. Vojnovic and A. Damjanovic, Symmetry factor and transfer coefficient in analysis of enthalpies of activation and mechanisms of oxygen reduction at platinum electrodes, Electrochimica Acta, 31(11), 1986, 1401-1402
11. D. B. Sepa, M. V. Vojnovic, M. Stojanovic and A. Damjanovic, Unconventional symmetry factor and transfer coefficient for oxygen reduction at Ir electrodes and their possible use as diagnostic criteria in mechanistic analysis, Journal of the Electrochemical Society, 134(4), 1987, 845-848
12. A. Damjanovic, Walsh and D. B. Sepa, Unconventional temperature dependence of the β-factor for oxygen evolution reaction at Pt electrodes in acid solutions: significance of the recovered activation energies, Journal of Physical Chemistry, 94, 1990, 1967-1973
13. A. Damjanovic, A. L. Utz and A. T. Walsh, “Anomalous” dependence of symmetry factor and transfer coefficient on temperature in oxygen evolution in alkaline solution, Journal

of Physical Chemistry, 97, 1993, 9177-9180

14. A. Damjanovic and D. B. Sepa, An analysis of the pH dependence of enthalpies and Gibbs energies of activation for O2 reduction at Pt electrode in acid solutions, Electrochimica Acta, 35(7), 1990, 1157-1162
15. P. H. Rieger, Electrochemistry, 2nd edition, Chapman & Hall, 1994
16. H. B. Oldham and J. C. Myland, Fundamentals of electrochemical science, Academic Press, 1994
17. D. B. Sepa, M. V. Vojnovic and L. M. and A. Damjanovic, Different views regarding the kinetics and mechanisms of oxygen reduction at Pt and Pd electrodes, Electrochimica Acta, 32 (1), 1987, 129-134
18. D. B. Sepa, M. V. Vojnovic, L. M. Vracar and A. Damjanovic, Apparent enthalpies of activation of electrodic oxygen reduction at platinum in different current density regions - 1: acid solution, Electrochimica Acta, 31(1), 1986, 91-96
19. D. B. Sepa, M. V. Vojnovic, L. M. Vracar and A. Damjanovic, A confirmation of the O_2 reduction mechanisms at Pt electrode from temperature studies, Electrochimica Acta, 29(8), 1984, 1169-1170
20. A. Damjanovic and M. A. Genshaw, Dependence of the kinetics of O_2 dissolution at Pt on the conditions for adsorption of reaction intermediates, Electrochimica Acta, 15(7), 1970, 1281-1283
21. A. Damjanovic and J. Bockris, The rate constants for oxygen dissolution on bare and oxide-covered platinum, Electrochimica Acta, 11(3), 1966, 376-377
22. L. M. Vracar, S. Burojevic and N. Krstajic, Unconventional temperature-dependence of Tafel slopes for the hydrogen evolution reaction at Pd-Ni electrode in alkaline solution, Journal of the Serbian Chemical Society, 63(3), 1998, 201-212
23. A. Damjanovic, M. A. Genshaw and J. Bockris, The roles of hydrogen peroxide in the reduction of oxygen at platinum electrodes, Journal of Physical Chemistry, 70(11), 1966, 3761-3762
24. D. B. Sepa, M. V. Vojnovic, L. M. Vracar and A. Damjanovic, Invariance with pH of enthalpies of activation for O2 reduction at Pt electrodes in acid solutions, Electrochimica Acta, 31(9), 1986, 1105-1111

25. A. Damjanovic and P. G. Hudson, On the kinetics and mechanism of O_2 reduction at oxide-film covered Pt electrodes, 1. Effect of oxide film thickness on kinetics, Journal of the Electrochemical Society, 135(9), 1988, 2269-2273
26. A. Damjanovic, On the kinetics and mechanism of O2 reduction at oxide film-covered Pt electrodes, 1. Electron transfer through the oxide film and mechanism of the reduction, Journal of the Electrochemical Society, 138(8), 1991, 2315-2320
27. L. D. Asnin, A. A. Fedorov and Y. S. Chekryshkin, Thermodynamic parameters of adsorption described by the logarithmic Temkin isotherm, Russian Chemical Bulletin, 50(2), 2001, 217-219
28. K. Carron, Determination of a Langmuir isotherm using SERS, Chemistry lab class notes, Department of Chemistry, University of Wyoming
29. D. B. Sepa, M. V. Vojnovic and A. Damjanovic, Reaction intermediates as a controlling factor in the kinetics and mechanism of oxygen reduction at platinum electrodes, Electrochimica Acta, 26(6), 1981, 781-793
30. M. Paucirova, D. M. Drazic and A. Damjanovic, The effect of surface coverage by adsorbed oxygen on the kinetics of oxygen reduction at oxide free platinum, Electrochimica. Acta, 18, 1973, 945-951
31. N. P. Siegel, M. W. Ellis, D. J. Nelson and M. R. von Spakovsky, Single domain PEMFC model based on agglomerate catalyst geometry, Journal of Power Sources, 115(1), 2003, 81-89
32. K. Ota and S. Mitsushima, Chapter 32: O_2 reduction on the Pt/polymerelectrolyte interface, Handbook of fuel cells - fundamentals, technology, applications, 2003
33. H. Schlichting (translated by J. Kestin), Boundary-layer theory, 7^{th} edition, McGraw-Hill, 1979
34. W. M. Deen, Analysis of transport phenomena, Oxford University Press, 1998
35. D. M. Bernardi, Water-balance calculations for solid-polymer-electrolyte fuel cells, Journal of the Electrochemical Society, 137(11), 1990, 3344-3350
36. D. M. Bernardi and M. W. Verbrugge, Mathematical model of a gas diffusion electrode bonded to a polymer electrolyte, AICHE Journal, 37(8), 1991, 1151-1163
37. D. M. Bernardi and M. W. Verbrugge, A mathematical model of the solid polymer

electrolyte fuel cell, Journal of the Electrochemical Society, 139(9), 1992, 2477-2491

38. T. E. Springer, T. A. Zawodzinski and S, Gottesfeld, Polymer electrolyte fuel cell model, Journal of the Electrochemical Society, 138(8), 1991, 2334-2341
39. T. E. Springer, M. S. Wilson, and S. Gottesfeld, Modeling and experimental diagnostics in Polymer electrolyte fuel cells, Journal of the Electrochemical Society, 140(12), 1993, 3513-3527
40. T. V. Nguyen, A gas distributor design for Proton-exchange-membrane fuel cells, Journal of the Electrochemical Society, 143(5), 1996, L103-L105
41. D. Bevers, M. Wohr, K. Yasuda and K. Oguro, Simulation for a polymer electrolyte fuel cell electrode, Journal of Applied Electrochemistry, 27(11), 1997, 1254-1264
42. K. Broka and P. Ekdunge, Modeling the PEM fuel cell cathode, Journal of Applied Electrochemistry, 27, 1997, 281-289
43. M. Eikerling, Y. I. Kharkats, A. A. Kornyshev, and Y. M. Volfkovich, Phenomenological theory of electro-osmotic effect and water management in polymer electrolyte proton conducting membranes, Journal of the Electrochemical Society, 145(8), 1998, 2684-2699
44. C. Marr and X. Li, Composition and performance modelling of catalyst layer in a proton exchange membrane fuel cell, Journal of Power Sources, 77(1), 1999, 17-27
45. J. J. Baschuk and X. Li, Modeling of polymer electrolyte membrane fuel cells with variable degrees of water flooding, Journal of Power Sources, 86(1-2), 2000, 181-196
46. A. Rowe and X. Li, Mathematical modeling of proton exchange membrane fuel cells, Journal of Power Sources, 102(1-2), 2001, 82-96
47. N. Djilali, D. Lu, Influence of heat transfer on gas and water transport in fuel cells, International Journal of Thermal Science 41(1), 2002, 29-40
48. T. F. Fuller and J. Newman, Water and thermal management in solid-polymer-electrolyte fuel cells, Journal of the Electrochemical Society, 140(5), 1993, 1218-1225
49. T. V. Nguyen and R. E. White, A water and heat management model for proton-exchange-membrane fuel cells, Journal of the Electrochemical Society, 140(8), 1993, 2178-2186
50. D. Thirumalai and R. E. White, Mathematical modeling of proton-exchange-membrane fuel cell stacks, Journal of the Electrochemical Society, 144(5), 1997, 1717-1723
51. J. S. Yi and T. V. Nguyen, An along-the-channel model for proton exchange membrane

fuel cells, Journal of the Electrochemical Society, 145(4), 1998, 1149-1159

52. J. S. Yi and T. V. Nguyen, Multicomponent transport in porous electrode of proton exchange membrane fuel cells using the interdigitated gas distributions, Journal of the Electrochemical Society, 146(1), 1999, 38-45
53. W. He, J. S. Yi and T. V. Nguyen, Two-phase flow model of the cathode of the PEM fuel cells using interdigitated flow channels, AICHE Journal, 46(10), 2000, 2053-2064
54. V. Gurau, H. Liu and S. Kakac, Two-dimensional model for proton exchange membrane fuel cells, AICHE Journal, 44(11), 1998, 2410-2422
55. Z. H. Wang, C. Y. Wang and K. S. Chen, Two-phase flow and transport in the air cathode of proton exchange membrane fuel cells, Journal of Power Sources, 94(1), 2001, 40-50
56. S-H. Ge and B-L. Yi, A mathematical model for PEMFC in different flow modes, Journal of Power Sources, 124(1), 2003, 1-11
57. S. Dutta, S. Shimpalee and J. W. Van Zee, Three-dimensional numerical simulation of straight channel PEM fuel cells, Journal of Applied Electrochemistry, 30, 2000, 135-146
58. T. Berning, D.M. Lu and N. Djilali, Three-dimensional computational analysis of transport phenomena in a PEM fuel cell, Journal of Power Sources, 106(1-2), 2002, 284-294
59. K. Hertwig, L. Martens and R. Karwoth, Mathematical modeling and simulation of polymer electrolyte membrane fuel cells. Part 1: Model structures and solving an isothermal One-cell model, Fuel Cells, 2(2), 2002, 61-77
60. D. Natarajan, T. V. Nguyen, Three-dimensional effects of liquid water flooding in the cathode of a PEM fuel cell, Journal of Power Sources, 115(1), 2003, 66-80
61. E. Hontanon, M. J. Escudero, C. Bautista, P. L. Garcia-Ybarra and L. Daza, Optimization of flow-field in polymer electrolyte membrane fuel cells using computation fluid dynamics techniques, Journal of Power Sources, 86(1-2), 2000, 363-368
62. A. Kumar and R. G. Reddy, Effect of channel dimensions and shape in the flow-field distributor on the performance of polymer electrolyte membrane fuel cells, Journal of Power Sources, 113(1), 2003, 11-18
63. J. C. Amphlett, R. M. Baumert and R. F. Mann, Parametric modeling of the performance of a 5-kW proton-exchange membrane fuel cell stack, Journal of Power Sources, 49(1-3),

1994, 349-356

64. J. Kim, S-M Lee, S. Srinivasan and C. E. Chamberlin, Modeling of proton exchange membrane fuel cell performance with an empirical equation, Journal of the Electrochemical Society, 142(8), 1995, 2670-2674
65. R. F. Mann, J. C. Amphlett, M. A.I. Hooper, H. M. Jensen, B. A. Peppley and P. R. Roberge, Development and application of a generalized steady-state electrochemical model for a PEM fuel cell, Journal of Power Sources, 86(1-2), 2000, 173-180
66. M. Wohr, K. Bolwin, W. Schnurnberger, M. Fischer, W. Neubrand and G. Eigenberger, Dynamic modeling and simulation of a polymer membrane fuel cell including mass transport limitation, International Journal of Hydrogen Energy, 23(3), 1998, 213-238
67. S. Um, C. Y. Wang and K. S. Chen, Computation fluid dynamics modeling of proton exchange membrane fuel cells, Journal of the Electrochemical Society, 147(12), 2000, 4485-4493
68. S. Yerramalla, A. Davari, A. Feliachi and T. Biswas, Modeling and simulation of the dynamic behavior of a polymer electrolyte membrane fuel cell, Journal of Power Sources, 124(1), 2003, 104-113
69. C. Singh and R. Billiton, System reliability modeling and evaluation, Hutchinson of London, 1977
70. M. Fowler, R. F. Mann, J. C. Amplett, B. A. Peppley and P. R. Roberge, Chapter 50: Reliability issues and voltage degradation, Handbook of fuel cells - fundamentals, technology, applications, 2003
71. D. P. Wiklinson and J. St-Pierre, Chapter 47: Durability, Handbook of fuel cells - fundamentals, technology, applications, 2003
72. S. Y. Ahn, S.-J. Shin, H. Y. Ha, S.-A. Hong, Y. C. Lee, T. W. Lim and I.-H. Oh , Performance and lifetime analysis of the kW-class PEMFC stack, Journal of Power Sources, 106(1-2), 2002, 295-303
73. S.-J. Shin, J.-K. Lee, H.-Y. Ha, S.-A. Hong, H.-S. Chun and I.-H. Oh, Effect of the catalytic ink preparation method on the performance of polymer electrolyte membrane fuel cells, Journal of Power Sources, 106, 2002, 146-152
74. A. E. Russell, S. Maniguet, R. J. Mathew, J. Yao, M. A. Roberts and D. Thompsett, In situ

X-ray absorption spectroscopy and X-ray diffraction of fuel cell electrocatalysts, Journal of Power Sources, 96(1), 2001, 226-232

75. P. Staiti, A. S. Arico, V. Antonucci and S. Hocevar, Morphological variation of platinum catalysts in phosphotungstic acid fuel cell, Journal of Power Sources, 70(1), 1998, 91-101
76. A. B. LaConti, M. Hamdan and R. C. McDonald, Chapter 49: Mechanisms of membrane degradation, Handbook of fuel cells - fundamentals, technology, applications, 200
77. R-Z Jiang and D. Chu, Voltage-time behavior of a polymer electrolyte membrane fuel cell stack at constant current discharge, Journal of Power Sources, 92(1-2), 2001, 193-198
78. M. W. Fowler, R. F. Mann, J. C. Amphlett, B. A. Peppley and P. R. Roberge, Incorporation of voltage degradation into a generalized steady state electrochemical model for a PEM fuel cell, Journal of Power Sources, 106(1-2), 2002, 274-283
79. Argonne National Laboratories, Department of Energy. In Basic Research Needs for the Hydrogen Economy; Workshop on Hydrogen Production, Rockville, Maryland, 2003, 53-60
80. T. Kyu and A. Eisenberg, Mechanical relaxations in perfluorosulfonated ionomer membranes. In Perfluorinated Ionomer Membranes, A. Eisenburg, H. L. Y., Ed. ACS: 1982; Vol. ACS Symposium Series 180, 79-110
81. Y. Kawano, Y. Wang, R. A. Palmer and S. R. Aubuchon, Stress-Strain Curves of Nafion Membranes in Acid and Salt Forms, Polimeros Tecnologia, 12 (2), 2002, 96-101
82. F. Bauer, S. Denneler and M. Willert-Porada, Influence of temperature and humidity on the mechanical properties of Nafion 117 polymer electrolyte membrane, Journal of Polymer Science, Part B: Polymer Physics, 43(7), 2005, 786-795
83. W. Y. Hsu and T. D. Gierke, Ion transport and clustering in Nafion perfluorinated membranes, Journal of Membrane Science, 13(3), 1983, 307-326
84. A. Eisenberg, B. Hird and R. B. Moore, A new multiplet-cluster model for the morphology of fandom ionomers, Macromolecules, 23(18), 1990, 4098-4107
85. H. G.. Haubold, T. Vad, H. Jungbluth and P. Hiller, Nano structure of NAFION: a SAXS study, Electrochimica Acta, 46(10-11), 2001, 1559-1563
86. L. Rubatat, G. Gebel and O. Diat, Fibrillar structure of Nafion: matching Fourier and real space studies of corresponding films and solutions, Macromolecules, 37(20), 2004, 7772-

7783

87. P. C. Heijden, L. Rubatat and O. Diat, Orientation of drawn Nafion at molecular and mesoscopic scales, Macromolecules, 37(14), 2004, 5327-5336
88. L. Rubatat, A. L. Rollet, G.. Gebel and O. Diat, Evidence of elongated polymeric aggregates in Nafion, Macromolecules, 35(10), 2002, 4050-4055
89. P. C. Heijden, A. Rosa, G.. Gebel and O. Diat, Relaxation of drawn Nafion films studied with birefingence experiments, Polymers for Advanced Technologies, 16(2-3), 2005, 102-107
90. K. D. Kreuer, On the development of proton conducting polymer membranes hydrogen and methanol fuel cells, Journal of Membrane Science, 185(1), 2001, 29-39
91. K. A. Mauritz and R. B. Moore, State of understanding of Nafion, Chemical Reviews, 104(10), 2004, 4535-4586
92. K. D. Kreuer, S. J. Paddison, E. Spohr and M. Schuster, Transport in proton conductors for fuel-cell applications: simulations, elementary reactions, and phenomenology, Chemical Reviews, 104(10), 2004, 4637-4678
93. V. Barbi, S. Funari, R. Gehrke, N. Scharnagl and N. Stribeck, Nanostructure of Nafion membrane material as a function of mechanical load studied by SAXS, Polymer, 44(17), 2003, 4853-4861
94. Y. S. Kim, L. Dong, M. A. Hickner, T. E. Glass, V. Webb and J. E. McGrath, State of water in Disulfonated poly(arylene ether sulfone) copolymers and a perfluorosulfonic acid copolymer (Nafion) and its effects on physical and eletrochemical properties, Macromolecules, 36(17), 2003, 6281-6285
95. Y. S. Kim, F. Wang, M. Hickner, S. McCartney, Y. T. Hong, W. Harrison, T. A. Zawodzinski and J. E. McGrath, Effect of acidification treatment and morphological stability of sulfonated poly(arylene ether sulfone) copolymer proton-exchange membranes for fuel-cell use above 100^{o}C, Journal of Polymer Science: Part B: Polymer Physics, 41(22), 2003, 2816-2828
96. F. Wang, M. Hickner, Y. S. Kim, T. A. Zawodzinski and J. E. McGrath, Direct polymerization of sulfonated poly(arylene ether sulfone) random (statistical) copolymers: candidates for new proton exchange membranes, Journal of Membrane Science, 197(1-2),

2002, 231-242

97. Y. Li, F. Wang, J. Yang, D. Liu, A. Roy, S. Case, J. Lesko and J. E. McGrath, Synthesis and characterization of controlled molecular weight disulfonated poly(arylene ether sulfone) copolymers and their applications to proton exchange membranes, Polymer, 47(11), 2006, 4210-4217
98. M. Hill, B. Einsla, Y. S. Kim and J. E. McGrath, Higher temperature PEM composite systems for fuel cells, Preprints of Symposia - American Chemical Society, Division of Fuel Chemistry, 49, 2004, 584-585
99. M. A. Hickner, H. Ghassemi, Y. S. Kim, B. R. Einsla and J. E. McGrath, Alternative polymer systems for proton exchange membranes (PEMs), Chemical Reviews, 104(10), 2004, 4587-4612
100. Y. A. Elabd, E. Napadensky and J. M. Sloan, Triblock copolymer ionomer membranes, Part I. methanol and proton transport, Journal of Membrane Science, 217(1-2), 2003, 227-242
101. O. Savadogo, Emerging membranes for electrochemical systems, part II. high temperature composite membranes for polymer electrolyte fuel cell (PEFC) applications, Journal of Power Sources, 127(1-2), 2004, 135-161
102. S. K. Young and K. A. Mauritz, Dynamic mechanical analyses of Nafion organically modified silicate nanocomposites, Journal of Polymer Science, Part B: Polymer Physics 39(12), 2001, 1282-1295
103. F. Bauer and M. Willert-Porada, Microstructural characterization of Zr-phosphate–Nafion® membranes for direct methanol fuel cell (DMFC) applications, Journal of Membrane Science, 233(1-2), 2004, 141-149
104. M. Gilbert, B. Haworth and D. J. Myers, Structure and properties of an oriented fluorosulfonated/PTFE copolymer, Polymer Engineering and Science, 44(2), 2004, 272-282
105. S. Kyriakides, D. Liu and S. Case, Mechanical behavior of Nafion and BPSH membranes, The 28th Annual Meeting of the Adhesion Society, K. Vorvolakos, Ed., Mobile, Alabama, 2005, 311-313
106. A. Z. Weber and J. Newman, Transport in polymer-electrolyte membranes, Journal of

the Electrochemical Society, 150(7), 2003, A1008-A1015

107. D. Liu, M. A. Hickner, S. W. Case and J. J. Lesko, Relaxation of proton conductivity and stress in proton exchange membranes, Journal of Engineering Materials and Technology, 2006, In press
108. P. J. James, J. A. Elliott, T. J. McMaster, J. M. Newton, A. M. S. Elliott, S. Hanna and M. J. Miles, Hydration of Nafion studied by AFM and X-ray scattering, Journal of Materials Science, 35(20), 2000, 5111-5119
109. W. Y. Hsu and T. D. Gierke, Elastic theory for ionic clustering in perfluorinated ionomers, Macromolecules, 15(1), 1982, 101-105
110. S. Slade, S. A. Campbell, T. R. Ralph and F. C. Walsh, Ionic conductivity of an extruded Nafion 1100 EW series of membranes, Journal of the Electrochemical Society, 149(12), 2002, A1556-A1564
111. T. A. Zawodzinski, M. Meeman, L. O. Sillerud and S. Gottesfeld, Determination of water diffusion coefficients in perfluorosulfonate ionomeric membranes, Journal of Physical Chemistry, 95(15), 1991, 6040-6044
112. G. Alberti, M. Casciola, L. Massinelli and B. Bauer, Polymeric proton conducting membranes for medium temperature fuel cells (110-160^{o}C), Journal of Membrane Science, 185(1), 2001, 73-81
113. D. Liu, S. Kyriakides, S. Case, J. Lesko, Y. Li and J. E. McGrath, Tensile behavior of Nafion and poly(arylene ether sulfone) copolymers and its morphological correlations, Journal of Polymer Science, Part B: Polymer Physics, 44(10), 2006, 1453-1465
114. D. P. Padiyan, S. J. Ethilton and K. Pauraj, Protonic conductivity and photoconductivity studies on $H_3PW_{12}O_{40}\times21H_2O$ single crystals, Crystal Research and Technology, 35(1), 2000, 87-94
115. L. Li, J. Zhang and Y. Wang, Sulfonated polyether ether ketone membranes cured with different methods for direct methanol fuel cells, Journal of Materials Science Letters, 22(22), 2003, 1595-1597
116. S. J. Paddison, M. Eikerling, T. A. Zawodzinski and L. R. Pratt, Molecular modeling of proton conduction in polymer electrolyte membranes of Nafion Type, ICCN International Conference on Computational Nanoscience, 2002, 15-116

117. S. H. Almeida andY. Kawano, Thermal behavior of Nafion membranes, Journal of Thermal Analysis and Calorimetry, 58(3), 1999, 569-577
118. V. Stanic, J. Braun and M. Hoberecht, Durability of membrane electrode assemblies (MEAs) in PEM fuel cells operated on pure hydrogen and oxygen, 1st International Energy Conversion Engineering Conference, Portsmouth, Virginia, 2003
119. J. St-Pierre and N. Jia, Successful demonstration of Ballard PEMFCS for space shuttle applications, Journal of New Materials for Electrochemical Systems, 5(4), 2002, 263-271
120. J. St-Pierre, D. P. Wilkinson, S. Knights and M. L. Bos, Relationships between water management, contamination and lifetime degradation in PEFC, Journal of New Materials for Electrochemical Systems, 3(2), 2000, 99-106
121. J. Xie, D. L. Wood, D. M. Wayne, T. A. Zawodzinski, P. Atanassov and R. L. Borup, Durability of PEFCs at high humidity conditions, Journal of the Electrochemical Society, 152(1), 2005, A104-A113
122. D. McMurry and C. DeRouin, Fuel Cell Technologies fuel cell test station software manual, Albuquerque, 2003
123. M C. Lefebvre, R. B. Martin and P. G. Pickup, Characterization of ionic conductivity profiles within proton exchange membrane fuel cell gas diffusion electrode by impedance spectroscopy, Electrochemical and solid-state letters, 2(6), 1999, 259-261
124. M. Roos, E. Batawi, U. Harnisch and Th. Hocker, Efficient simulation of fuel cell stacks with the volume averaging method, Journal of Power Sources, 118(1-2), 2003, 86-95
125. X. Wang, D. Myers and R. Kumar, Non-precious metal electrocatalysts, Argonne National Laboratory Report, 2005
126. S. Hamrock, New membranes for PEM fuel cells, Advances in Materials for Proton Exchange Membrane Fuel Cell Systems, Pacific Grove, CA, 2005
127. P. Choi, N. H. Jalani and R. Datta, Thermodynamics and Proton Transport in Nafion, II: Proton Diffusin Mechanisms and Conductivity, Journal of the Electrochemical Society, 152(3), 2005, E123-E130